The CESR Test Accelerator Electron Cloud Research Program Phase I Report

Editors: *M.A. Palmer, M.G. Billing, G.F. Dugan, M.A. Furman, D.L. Rubin*

November 29, 2011

Program Contributors:

N. Omcikus[1], K.C. Harkay[2], R. Dowd[3], W. Guo, S.Y. Zhang[4], R.L. Holtzapple[5], L. Fabrizio[5], M. Randazzo[5], D. Asner[6], M. Cunningham[6], D. Carmody[7], J. Chu[7], F. Antoniou[8], S. Calatroni[8], F. Caspers[8], M. Gasior[8], R. Jones[8], Y. Papaphilippou[8], J. Pfingstner[8], G. Rumolo[8], H. Schmickler[8], M. Taborelli[8], D. Gonnella[9], J. Jones[10], A. Wolski[10], D. Teytelman[11], J.P. Alexander[12], J. Barley[12], L. Bartnick[12], M.G. Billing[12], K.R. Butler[12], J.R. Calvey[12], S.S. Chapman[12], G.W. Codner[12], M. Comfort[12], C.C. Conolly[12], J.V. Conway[12], J.A. Crittenden[12], C.A. Dennett[12], J.A. Dobbins[12], G.F. Dugan[12], N. Eggert[12], M. Ehrlichman[12], E. Fontes[12], M.J. Forster[12], R.E. Gallagher[12], S.W. Gray[12], S. Greenwald[12], D.L. Hartill[12], W. Hartung[12], Y. He[12], R. Helms[12], L. Hirxhman[12], W.H. Hopkins[12], N. Kaminsky[12], J. Kandaswamy[12], J-S. Kim[12], D.L. Kreinick[12], B. Kreis[12], J. Lanzoni[12], Z. Leong[12], Y. Li[12], H. Liu[12], X. Liu[12], J.A. Livezey[12], A. Lyndaker[12], J. Makita[12], M. McDonald[12], V. Medjidzade[12], R.E. Meller[12], T.P. Moore[12], T.I. O'Connell[12], M.A. Palmer[12], S.B. Peck[12], D.P. Peterson[12], G.A. Ramirez[12], M.C. Rendina[12], P. Revesz[12], D.H. Rice[12], N.T. Rider[12], D.L. Rubin[12], D.C. Sagan[12], S. Santos[12], J. Savino[12], R.M. Schwartz[12], R. Seeley[12], J. Sexton[12], J. Shanks[12], J.P. Sikora[12], E.N. Smith[12], K.W. Smolenski[12], K. Sonnad[12], M. Stedinger[12], C.R. Strohman[12], A.B. Temnykh[12], M. Tigner[12], J.T. Urban[12], S. Vishniakou[12], W. Whitney[12], T. Wilksen[12], H.A. Williams[12], Y. Yariv[12], M.C. Ross[13], C.Y. Tan[13], R. Zwaska[13], B. Carlson[14], K. Hammond[15], Department of Physics, Harvard University, Cambridge, MA 02138, U.S.A. [15], M. Lawson[15], C. Cude[16], T. Demma[17], J. Flanagan[18], H. Fukuma[18], T. Ishibashi[18], P. Jain[18], K. Kanazawa[18], S. Kato[18], K. Kubo[18], K. Ohmi[18], K. Oide[18], H. Sakai[18], K. Shibata[18], Y. Suetsugu[18], H. Tajima[18], M. Tobiyama[18], J. Urakawa[18], R.J. Macek[19], J. Byrd[20], C.M. Celata[20], J.N. Corlett[20], S. De Santis[20], M.A. Furman[20], A. Jackson[20], R. Kraft[20], D.V. Munson[20], G. Penn[20], D.W. Plate[20], A. Rawlins[20], M. Venturini[20], M. Zisman[20], E.L. Wilkinson[21], H. Jin[22], L. Boon[23], A.F. Garfinkel[23], D. Kharakh[24], J. Ng[24], M.T.F. Pivi[24], L. Wang[24], R.P. Badman[25], S. Veitzer[26], L. Schächter[27], P. Kehayias[28], and L. Hales[29]

[1]American River College, Sacramento, CA 95841, U.S.A.
[2]Argonne National Laboratory, Argonne, IL 60439, U.S.A.
[3]Australian Synchrotron, Clayton, 3168, Australia.
[4]Brookhaven National Laboratory, Upton, NY 11973, U.S.A.
[5]Physics Department, California Polytechnic State University, San Luis Obispo, CA 93407, U.S.A.
[6]Department of Physics, Carleton University, Ottawa, Ontario, K1S 5B6, Canada.
[7]Department of Physics, Carnegie Mellon University, Pittsburgh, PA, 15389, U.S.A.
[8]CERN, CH-1211 Genève 23, Switzerland.
[9]Department of Physics, Clarkson University, Potsdam, NY 13699, U.S.A.
[10]Cockroft Institute, Warrington, Cheshire, U.K.
[11]Dimtel, Inc., San Jose, CA 95124, U.S.A.
[12]Cornell Laboratory for Accelerator-based Sciences and Education, Cornell University, Ithaca, NY, 14850, U.S.A.

[13]Fermi National Accelerator Laboratory, Batavia, IL 60510, U.S.A.
[14]Physics Department, Grove City College, Grove City, PA 16127, U.S.A.
[15]Department of Physics, Harvey Mudd College, Claremont, CA 91711, U.S.A.
[16]Department of Physics, Indiana University, Bloomington, IN 47405, U.S.A.
[17]Istituto nazionale di Fisica Nucleare - Laboratori Nazionali di Frascati, 00044 Frascati, Italy.
[18]High Energy Accelerator Research Organization (KEK), Tsukuba, Ibaraki 305-0801, Japan.
[19]Los Alamos National Laboratory, Los Alamos, NM 87544, U.S.A.
[20]Lawrence Berkeley National Laboratory, Berkeley, CA 94270, U.S.A.
[21]Department of Physics, Loyola University, Chicago, IL, 60626, U.S.A.
[22]Department of Physics, Postech, Pohang, Gyeongbuk 790-784, R.O.K.
[23]Department of Physics, Purdue University, West Lafayette, IN 47907, U.S.A.
[24]SLAC National Accelerator Laboratory, Menlo Park, CA 90425, U.S.A.
[25]Department of Physics, Syracuse University, Syracuse, NY 13244, U.S.A.
[26]Tech-X Corporation, Boulder, CO, 80303, U.S.A.
[27]Department of Electrical Engineering, Technion-IIT, Haifa, 32000, Israel.
[28]Department of Physics and Astronomy, Tufts University, Medford, MA 02155, U.S.A.
[29]Department of Physics and Astronomy, University of Utah, Salt Lake City, UT 84112, U.S.A.

Contents

List of Figures

List of Tables

Chapter 1

Electron Cloud Induced Beam Dynamics

One of the key goals of the CesrTA research program is to improve our understanding of the interaction of the electron cloud with the high energy particle beam. This improved understanding is required to be able to extrapolate with confidence from the experimental conditions of CesrTA to the conditions expected for the ILC damping rings.

The interaction of the particle beam with the cloud can be studied by measuring the properties of the beam in the presence of the cloud. The key beam properties which are influenced by the cloud are the beam's closed orbit distortion (quite small, and not extensively studied with CesrTA), the frequency spectrum of the beam centroid's coherent dipole motion relative to this orbit, and the beam's transverse position distribution.

In CesrTA, the beam is formatted longitudinally into a train of short ($\sim$ 10 mm) bunches separated by an adjustable spacing (variable from a minimum of 4 ns, up to a maximum equal to the revolution period, about 2.5 μs). As described in Chapter **??**, for sufficiently closely-spaced bunches, the electron cloud grows along the train, and so the cloud environment is different for each bunch. For this reason, it is critical that the beam dynamics measurement made to probe the cloud be done on a bunch-by-bunch basis.

The frequency spectrum of the coherent dipole motion of each bunch contains a wealth of information. In particular, this information includes

- the amplitude, frequency, and line shape of the betatron lines, which are sensitive to the electron cloud's electric field, to the mode of oscillation of the bunches in the train, and to the presence of multibunch instabilities;
- the amplitude, frequency, and line shape of "head-tail" lines, which are generally separated from the betatron lines by approximately the synchrotron frequency, and are sensitive to internal motion of the bunch driven by electron-cloud-induced single-bunch head-tail instabilities.

In addition, the time dependence of the amplitude of the betatron and "head-tail" lines, after bunch motion has been excited by an external source, provides information on the damping of these lines, which is related to aspects of the effective electron-cloud impedance not probed by tune measurements.

The transverse position distribution of each bunch is sensitive to

- emittance growth driven by single-bunch instabilities. Generally, this growth would be expected to be correlated with the observation of "head-tail" lines described in the previous paragraphs;
- incoherent emittance growth, driven by non-linear components of the electron cloud's electric field, which may take place before the onset of emittance growth driven by single-bunch coherent instabilities.

Incoherent emittance growth, if present, is critical to understand fully, since it could impact achieving the design emittance goals of the ILC damping rings.

For a full understanding of the observational data discussed above, comparison with simulations of the electron cloud is essential. The electron cloud build-up simulation programs discussed in Chapter **??** can be used to compute the expected betatron tune shifts, and comparison with the simulations allows the parameters of the effective ring-averaged electron cloud density sensed by the beam to be determined. Specialized simulation programs([2], [3]) have been written to model the interaction of the cloud and beam responsible for incoherent emittance growth and single-bunch instabilities.

In the sections below, the experimental hardware and techniques used to obtain the measurements are described (Section 1.1); the simulation tools and their applications to the measurements are discussed (Section 1.2); and the most important beam dynamics observations and comparisons with simulations are presented (Section 1.3). The final section presents a summary and discussion of future work.

1.1 Experimental Hardware and Techniques

1.1.1 Hardware Overview

CesrTAhas been studying the effects of electron clouds on stored beams in order to understand their impact on future linear-collider damping ring designs. One of the important issues is the way that the electron cloud alters the dynamics of bunches within the train. Techniques for observing the dynamical effects of beams interacting with the electron clouds have been developed.

There are several beam parameters, which are particularly relevant for the study of electron cloud effects. Since the electron cloud can produce focusing of the stored beam, measuring the betatron tunes of bunches through the train gives information about the density of the cloud along the length of the train. The electron cloud can also produce unstable motion in bunches later in the train. To observe the unstable motion, it is necessary to detect the amplitude of the betatron frequency and any other frequencies representing different modes of oscillation (e.g. head-tail modes) of bunches within the train. The unstable motion may also result in enlargement of the vertical beam size, so the measurement of the vertical beam size for each bunch in the train is important. Before beam conditions approach the regime for the onset of unstable motion, it is possible to measure the damping of coherent motion of the bunches using drive-damp techniques. This method excites coherent dipole betatron modes or head-tail modes for each bunch within the train and then observes the damping of the motion. Thus it is possible to observe how the coherent motion becomes less

stable while the bunches are stable. The methodology and examples of typical measurements for these techniques are presented below.

1.1.2 Bunch-by-Bunch Tune Measurements

Over the CesrTAproject several different techniques have been utilized for making tune shift measurements for individual bunches within trains of bunches. These techniques, their benefits and limitations will be described in this section.

1.1.2.1 Multi-bunch Large Amplitude Excitation

This method for observing the tunes of different bunches within the train pulses a pinger magnet with a single-turn excitation to deflect all of the bunches within the train and thus start an oscillation of their centroids. The CBPM system is then is timed to read out a number of BPMs over several thousand turns for all bunches in the train (see block diagram in Fig. **??**); the data acquisition is synchronized with the triggering of the pinger magnets deflection. After recording the turn-by-turn bunch positions, the data is analyzed offline with a Fast Fourier transform (FFT), from which the betatron tunes are determined. During these measurements the peak vertical beam displacements, for example, were typically 7 mm and 2 mm at 2.1 GeV and 5.3 GeV, respectively.

Since data from all bunches is recorded at the same time, it is relatively rapid to take data in one set of conditions and, since the data from all bunches is taken on the same turns, this method is relatively insensitive to any drifts in the storage ring tunes. However, the fact that all bunches are excited at the same instant implies that the lowest coupled bunch mode is excited for the train of bunches. As discussed in Section 1.2.1, when the train is oscillating in this mode, the bunch-by-bunch horizontal tune shifts induced by the electron cloud in the dipoles are strongly suppressed, and difficult to measure. It is also the case that the pinger excitations are relatively large with respect to the stored beams size, e.g. typically the vertical oscillation amplitude may exceed many tens of the vertical sigma. So the beams oscillation is exploring a fairly large volume of the electron clouds distribution.

1.1.2.2 Single Bunch Small Amplitude Excitation

Another approach has been developed for bunch-by-bunch tune measurements. This approach focuses on reducing the coupling from preceding bunches to the bunch that one is trying to measure. As shown schematically for one stripline kicker in Fig. 1.1), this is accomplished by driving both the horizontal and vertical stripline kickers only for the bunch being measured by making use of the external modulation input for the beam size feedback system. The source for the signal for the external modulation port comes from a frequency synthesizer, whose output frequency is swept across the range of betatron oscillation frequencies for the bunches. The frequency is swept with a saw-tooth at 500 Hz, driving the bunch in the dipole oscillation mode when the excitation frequency crosses the betatron resonance. Again the turn-by-turn position data is recorded for a number of BPMs using the CBPM system readout (as shown in the block diagram in Fig. **??**) with the total turn record length long enough to capture at least one excitation and damping cycle. The measurement process is repeated as the excitations delay is stepped from one bunch to the next,

resulting a set of positions for all bunches at each delay. The data is analyzed offline with a FFT to give the oscillation frequency of the excited bunch and coupling of its motion to subsequent bunches via the electron cloud.

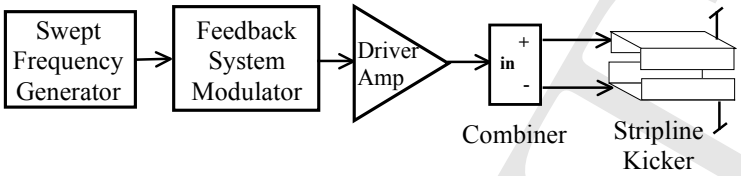

Figure 1.1: Single bunch excitation method using the stripline kicker, driven by a swept frequency source via the feedback systems external modulation port.

Some results are presented here for illustration of this technique; the data were taken with a 10 bunch train with a 14 nsec spacing in 2.1 GeV conditions. Fig. 1.2 shows the horizontal position data for the first, fifth and tenth bunch, when only bunch number 5 was being excited. During the 2048-turns of the data-samples taken on simultaneous turns for the three bunches, it is clear that bunch 5 was excited with two complete cycles of the swept signal source. This is even clearer in Fig. 1.3 when viewing the horizontal spectra of all 10 bunches when bunch numbers 1, 5 and 10 were being driven individually. The fact that the stripline kicker is exciting only one bunch is quite evident in both figures 1.2 and 1.3.

For comparison with the horizontal data, the matching set of vertical data is presented here for the same storage ring and electron cloud conditions as above. The vertical position data for bunches 1, 5 and 10 is shown in Fig. 1.4, when only bunch 5 is driven. Also the vertical spectra for all bunches are shown in Fig. 1.5, when bunches 1, 5 and 10 are individually excited. The interesting feature, visible in the vertical data, is that even though only one bunch is being driven, its motion is coupling the subsequent bunches in the train. Fig. 1.5 presents evidence that this coupling increases along the train, suggesting that the electron cloud may be playing some part in this bunch-to-bunch vertical dipole coupling.

This technique has the advantage of avoiding cross-coupling from preceding bunches to the bunch being studied, while also providing information about the coupling of the motion of one bunch to later bunches via the electron cloud. The excitation level can, in principle, be tailored for the bunch that is being driven; the ability to keep a relatively fixed amplitude for the bunchs oscillation could be important for conditions when the first bunches in the train are more stable but the latter bunches are not. This method has the drawback that it slower that the preceding method as it requires collecting turn-by-turn position data for every bunch times the number of bunches within the train, and is, therefore, sensitive to drifts in the tunes of the storage ring.

1.1.2.3 Feedback System Response

Another approach for tune measurements became apparent after the installation of the Dimtel[1] feedback electronics, capable of damping bunches with spacings down to 4 nsec. While looking at the FFT of the position for a single bunch as part of the feedback system diagnostics, it was observed that the signal response varied as a function of the feedback gain. At low gains the betatron peak

[1] Dimtel Inc., www.dimtel.com.

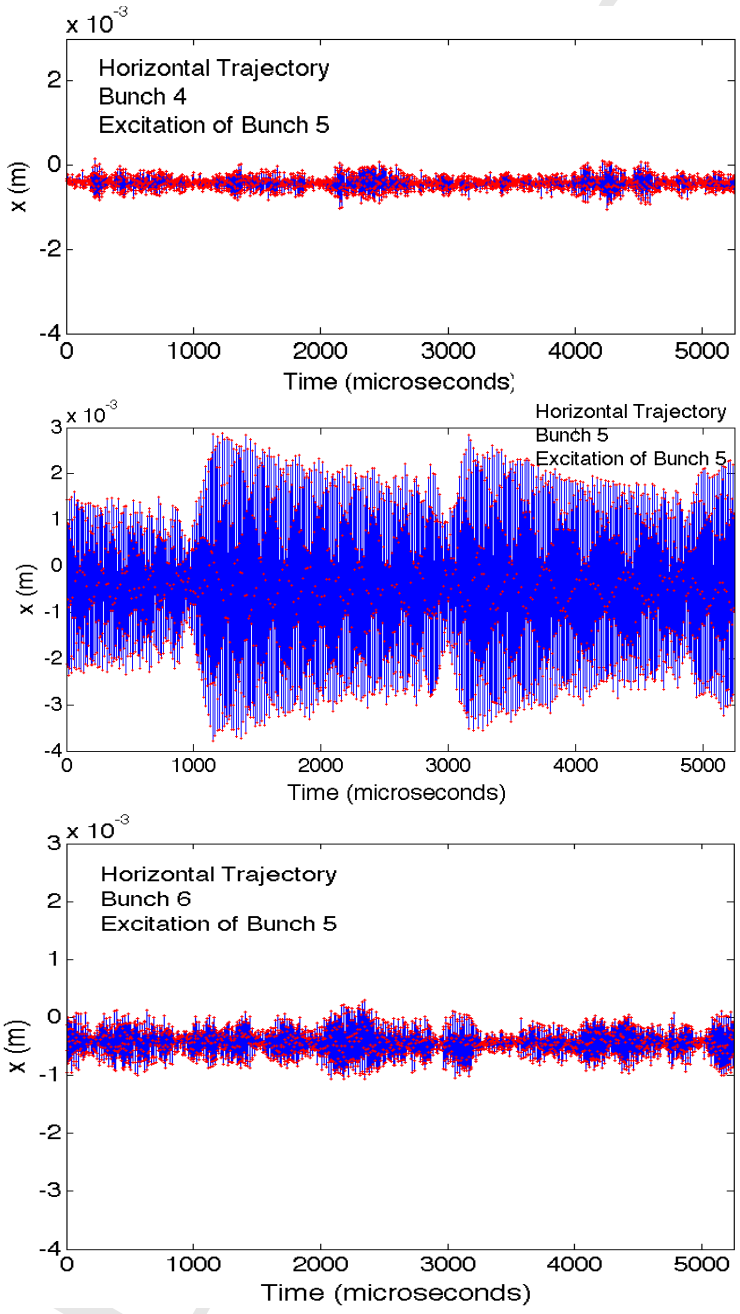

Figure 1.2: Horizontal position of bunches 1, 5 and 10 (respectively for the top, middle and bottom plots) for a 10-bunch train when only bunch number 5 was driven.

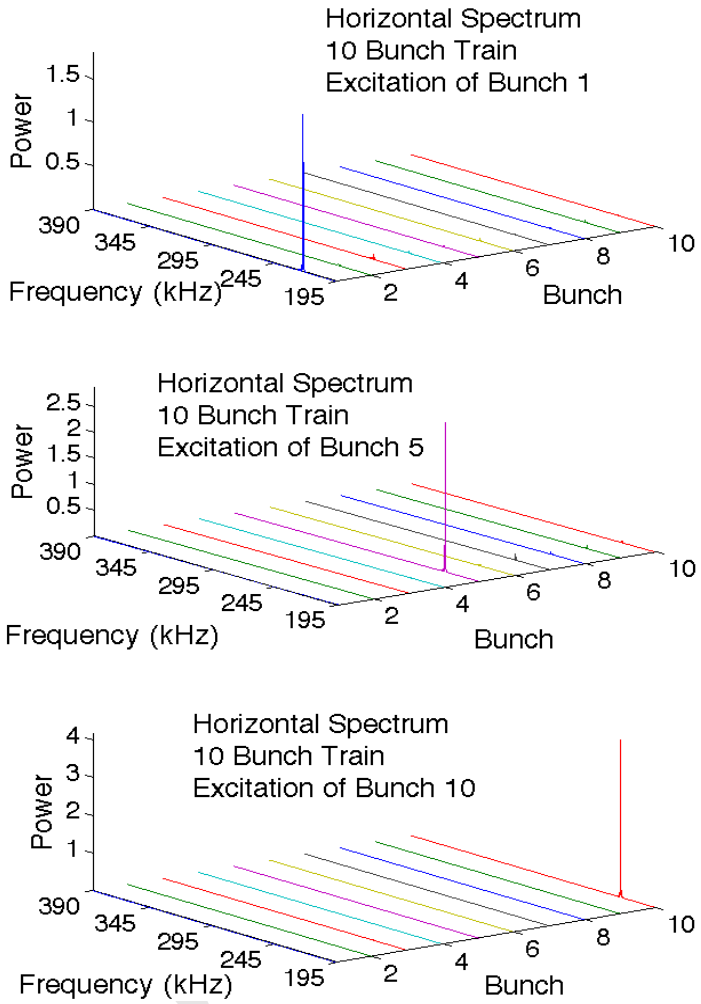

Figure 1.3: Horizontal position spectra of all bunches in a 10-bunch train when bunches number 1, 5 and 10 (respectively for the top, middle and bottom plots) were driven individually.

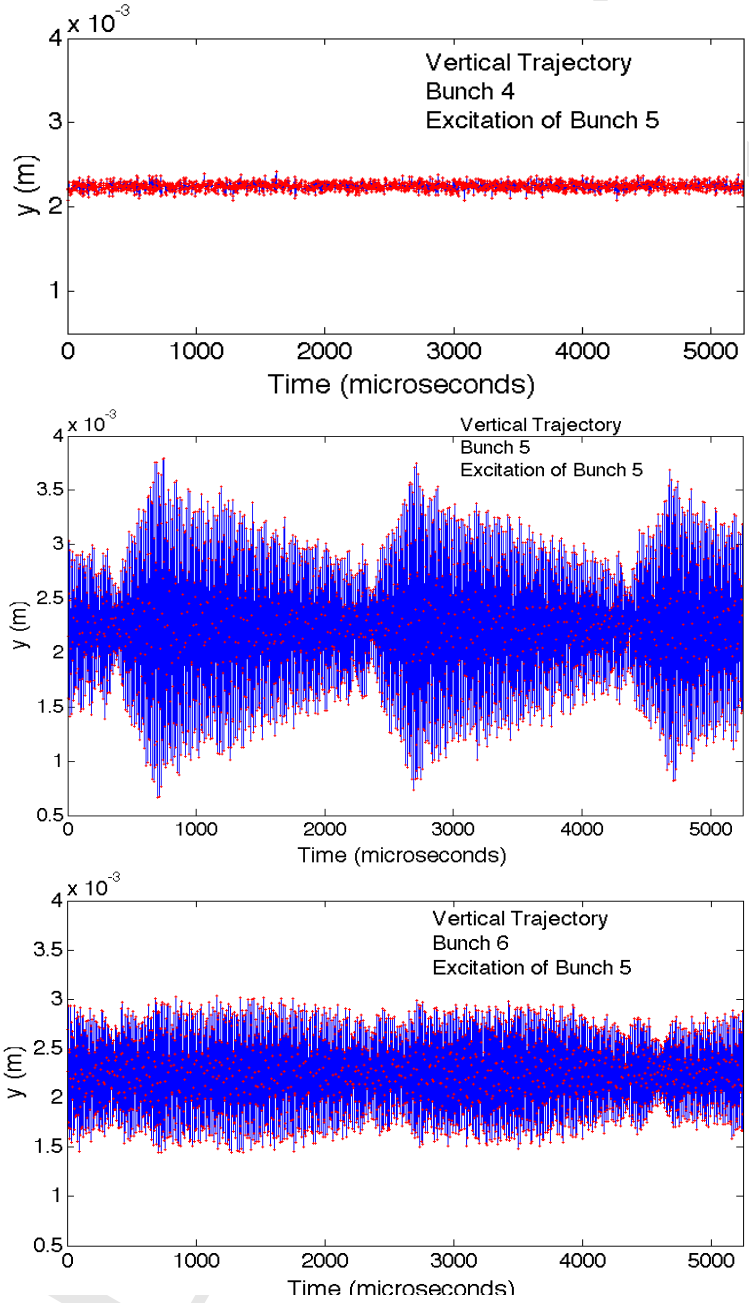

Figure 1.4: Vertical position of bunches 1, 5 and 10 (respectively for the top, middle and bottom plots) for a 10-bunch train when only bunch number 5 was driven.

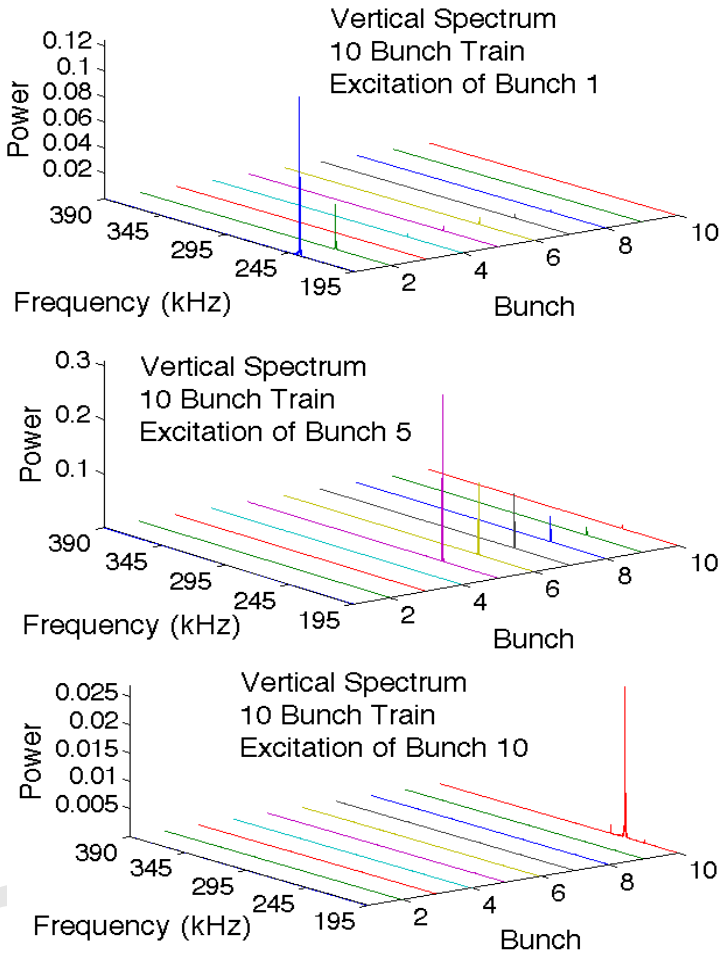

Figure 1.5: Vertical position spectra of all bunches in a 10-bunch train when bunches number 1, 5 and 10 (respectively for the top, middle and bottom plots) were driven individually.

is visible, but as the gain is increased the amplitude of the peak decreases until it become a notch in the spectrum at high gain. The explanation for this effect is that there is a broadband excitation of the beam and the feedback system is phased to suppress the bunchs response preferentially at the betatron frequency. When the feedback settings have been fully optimized, the notch in the spectrum for each bunch marks the location of its betatron oscillation frequency.

The position data generally represents the effect of probing the electron cloud in a regime when the bunches are moving at small amplitudes. An example of data taken using this method is seen in Fig. 1.6. There is a very clear trend for the vertical focusing effect from the accumulating electron cloud, which is visible the plot. Although this method is quite appealing, only a few tune shift measurements have been performed via this method. This technique works well for 4 nsec-spaced bunches, but it requires fairly exact adjustments of the feedback system parameters to be able to clearly identify the notches in the bunch spectra. To obtain the most accurate spectra, the data for each bunch is averaged typically for 30 seconds, allowing some uncertainty in the tunes due to longerterm drifts in the storage ring focusing.

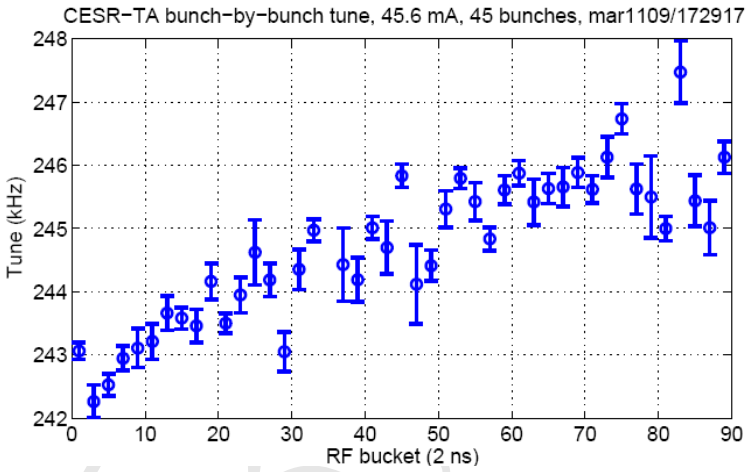

Figure 1.6: Vertical tune vs. RF bucket number for a train of 45 bunches with 4 nsec bunch spacing determined from notches in the spectra from the feedback error signal.

1.1.2.4 Self-Excitation

The last method for bunch-by-bunch tune shift measurements to be presented here is a by-product of the observation of beam instabilities, described in the next section. In this set of measurements the position spectrum of each bunch is measured with a spectrum analyzer. Two of the peaks that are visible in these self-excited spectra are the horizontal and vertical dipole modes. The shift of the tunes from bunch to bunch are easily detected via this method. Since most of these measurements are taken in conditions when the beam is above or near an instability threshold for at least some of the bunches within the train, the self-excited amplitudes of the dipole motion will vary along the train. This method is quite sensitive to low signal levels with the noise floor for small amplitude oscillations at the level of 0.4 μm-rms horizontally and 0.2 μm-rms vertically. Due to averaging in the spectrum analyzer, the data acquisition requires about 1 minute for each bunch, leaving this method sensitive to drifts in the storage ring tunes.

1.1.3 Instability Measurements

An important set of CesrTAmeasurements study beam instabilities due to the electron cloud. This study focuses on the growth of self-excited oscillations of the bunchs centroid and the growth of vertical beam size along the train under various accelerator and electron cloud conditions. The first part of the hardware utilized for these measurements is a monitor for the bunch-by-bunch beam position. The other detection system required is the xBSM monitor for determining vertical beam of each bunch.

Bunch-by-bunch Position Spectra

For instability studies the bunch-by-bunch position measurements are accomplished by a BPM detector connected to one of CESRs original relay-based BPM system processors, which in turn passes its video output signal to a spectrum analyzer in the control room. (For further description see text above and the block diagram shown in figure 2b.) BPM33W, which is located at a higher vertical beta point, has generally been used as the detector for these observations. The signal is taken from one button, making it sensitive to both the horizontal and vertical motion. The data taking software sets the trigger delay for the sampling gate to select a particular bunch within the train. For almost all of the data, an RG-174 coaxial cable is placed within the signal path to limit the bandwidth of the button signal (giving an effective 20 dB of signal attenuation) and to this an additional 12 dB of amplification is added. The signal is then sent to the biased peak rectifier circuit, which has an effective bandwidth of 700 MHz, and a decay time constant of approximately 5 μsec. The resulting video signal is buffered and sent on a wide-band coaxial cable to a spectrum analyzer in the control room.

The spectrum analyzer is an Hewlett Packard model 3588A, operating in the baseband (in these studies the center frequency ranges from 190 kHz to 210 kHz) in Narrowband Zoom mode with a 40 kHz span. This mode of operation performs a ±20 kHz FFT on time slices of the signal and these spectra are averaged for 100 time slices, taking about 10 seconds for each 40 kHz step of the center frequency. At 2.1 GeV the position sensitivity of the signal from the BPM at 33W was measured to be

$$\begin{aligned} x_{rms} &= x_0 \left(\tfrac{1\ mA}{I_b}\right) 10^{A_x/20\ dBm} \\ y_{rms} &= y_0 \left(\tfrac{1\ mA}{I_b}\right) 10^{A_y/20 dBm} \end{aligned} \tag{1.1}$$

where $x_0 = 81.3$ mm and $y_0 = 45.3$ mm when the bunch length was approximately 10 mm. With this gain configuration and over the frequency range of study, the noise baseline falls from -95 dBm to -105 dBm (corresponding in the vertical direction, respectively, to displacements of 1.1 μm-rms to 0.33 μm-rms for a 1 mA bunch.)

Representative self-excited spectra of the first and last bunch in a 30-bunch positron train at 2.1 GeV are shown in Figs. 1.7 and 1.8. For this train the horizontal tunes are in the range from 212 kHz to 218 kHz, and the vertical tunes are in the range from 224 kHz to 227 kHz. Since this spectrum overlaps the 1/2-integer resonance at 195 kHz, this frequency is a reflection point for the spectra. For bunch 30, additional lines are visible in the ranges 198-201 kHz and 250-252 kHz; these correspond to vertical head-tail modes as their frequencies are plus and minus the synchrotron oscillation frequency added to the vertical tune. The baseline is seen to be falling as roughly a 1/f noise spectrum. There are also a number of unrelated noise lines, scattered throughout

the spectra assumed to be due to cultural noise sources. A mountain-range plot of the spectra of all 30 bunches within a 30 bunch-long train is plotted in Fig. 1.9. A cut of the spectrum has been made at the half integer resonance (195 kHz) to suppress the reflected spectral lines. In this plot the self-excited vertical tune amplitude begins to grow at approximately bunch 10 and continues to grow in amplitude until near bunch 20. In this region the two vertical head-tail lines appear above the noise background. Also around bunch 15 the spectral peak of the horizontal tune appears to bifurcate, something which is also seen in the bottom plot of Fig. 1.8, and on close examination these data also show bifurcation of the vertical tune and the vertical head-tail lines for the latest bunches in the train. Fig. 1.9 also shows a number of fences, i.e. peaks in the spectrum at fixed frequencies due to external cultural noise sources.

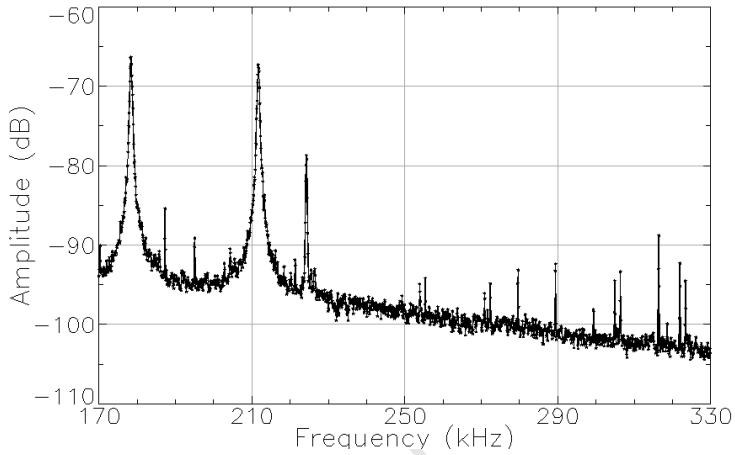

Figure 1.7: Self-excited beam power spectra for bunch 1 in a 30 bunch-long positron train at 2.1 GeV.

Many tests have examined the self-consistency and interpretation of the data. The identification of the vertical and horizontal tunes was checked by changing the controls for each separately and verifying which spectral peak moved. They were also checked using BPMs at other locations, which had buttons summed to produce dominantly horizontally- or vertically-sensitive detectors. The interpretation that the vertical head-tail lines were not inter-modulation distortion components coming from the processing electronics was tested [5] by switching an attenuator into the signal path upstream of the peak detector and observing that all spectral peaks decreased by 9±1 dB. If the head-tail lines were actually inter-modulation cross-products from the non-linearity of the electronic processing, then they would have decreased by 18 dB and they only decreased by 9 dB.

This method for detecting the frequency spectra of the bunches is fairly sensitive, however measurements must be made for each individual bunch. The measurement time is about 1 minute per bunch for the frequency range, over which we choose to take data. This means that the data represents the equilibrium state of any unstable motion. It also implies that due the typical beam lifetimes, the beam must be refilled a number of times during the set of data for one observation. In our case we choose typically to refill after measuring five bunch spectra, which, when plotted, gives the amplitude of peaks within the spectrum a slightly scalloped shaped over five bunches. This refilling cycle coordinates fairly well with the cycle to measure and readout the bunch-by-bunch

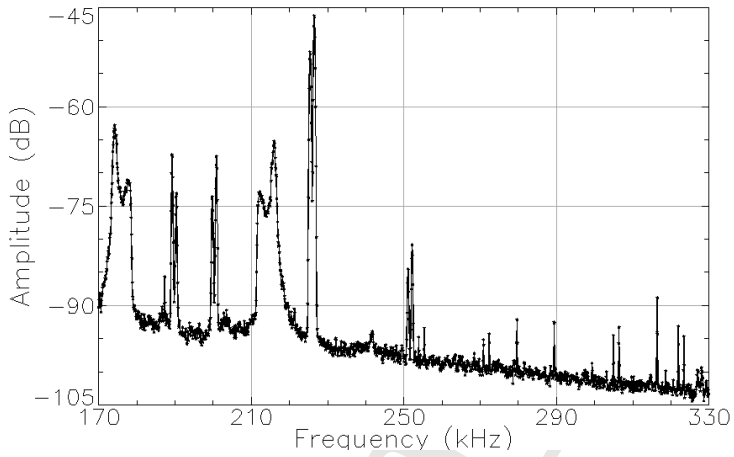

Figure 1.8: Self-excited beam power spectra for bunch 30 in a 30 bunch-long positron train at 2.1 GeV.

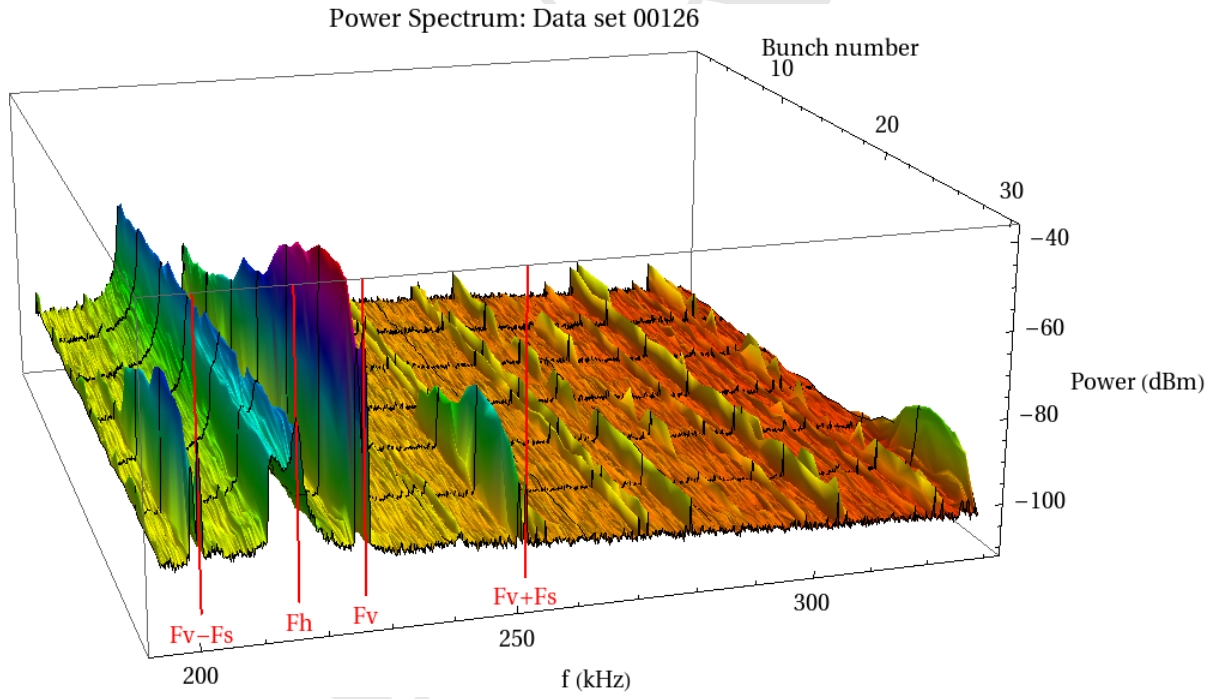

Figure 1.9: Self-excited beam power spectra for bunches 1 through 30 in a 30 bunch-long positron train at 2.1 GeV. The horizontal axis is the frequency, the vertical axis is the spectral power in dB and the axis into the page is the bunch number with bunch 30 being in the foreground. Red vertical lines in the foreground denote in ascending order the location of the m = -1 vertical head-tail line, the horizontal tune, the vertical tune and the m = +1 vertical head tail line.

and turn-by-turn xBSM data.

We have tried to readout the turn-by-turn and bunch-by-bunch positions from a number of BPMs via the CBPM system (giving a much faster data acquisition time.) Unfortunately the head-tail lines are not visible in the CBPM data. Our explanation is that the relay BPM system peak rectifies the position signal and, if there is a temporal variation due to synchrotron motion, the arrival time of the signal varies correspondingly. This gives a frequency modulation to the position signal when viewed by the spectrum analyzer. The CBPM processing is different; the signal is sampled at a fixed time corresponding to the positive peak of the button BPM pulse. Any variation in the arrival time produces only a second order variation in amplitude and, even if one moved the sampling time significantly off of the peak, it does not produce any signal at the head-tail line frequencies.

Bunch-by-Bunch Beam Size

The second detection system in use during these experiments for determining vertical beam size of each bunch is the xBSM monitor (described below in section 1.1.5). During a given set of instability measurements typically data are taken using all three sets of optics, the adjustable slit (AKA pinhole), the Fresnel zone plate optics chip and the coded aperture optic chip. This allows the greatest range of sensitivity for measurements of the vertical size and centroid motion of the beam. During the measurement cycle, the beam size data are taken bunch-by-bunch and turn-by-turn generally immediately after the train has been topped off, usually occurring after taking the spectrum for every fifth bunch.

1.1.4 Mode Growth Rates

A complement to the instability measurements, described in the preceding section, are the damping rate measurements for the coherent transverse modes. The instability measurements easily record the large amplitude signals as the bunches become unstable and ultimately limit due to non-linearities in the bunchs dynamics. However, the damping measurements give information about the stability of the bunch at small amplitudes before the bunch goes unstable, the regime in which storage rings and damping rings will actually operate. These studies will give some insight about how the beam instability begins developing as one looks from bunch to bunch along the train.

Drive-Damp Excitation

The basic idea for these observations is to employ the same relay BPM configuration as is used for the instability measurements. However, the spectrum analyzers center frequency is adjusted to be at either the vertical betatron dipole-mode frequency or one of the head-tail mode frequencies while the spectrum analyzer is set to be in Zero Span mode. In this mode the analyzer functions as a tuned receiver with its display producing signal amplitude vs. time. The spectrum analyzers tracking generators output is sent to the vertical feedback systems external modulation input. Aside from the spectrum analyzers control settings, this is quite similar to the hardware configuration shown in Fig. 1.1. By adjusting the digital timing controls for the modulators external input, it possible to drive only one bunch as long as bunch spacing is greater than 6 nsec. (If the bunch spacing is 4 nsec, then the timing of the pulse on the beam stabilizing feedback systems stripline kicker will the deflect the bunch under study and slightly kick the following bunch.) To permit the drive-damp modulation of the beam, there is one additional element added to the block diagram of Fig. 1.1. This element is a modulating gate for the spectrum analyzers tracking generator signal. This modulator gate is timed with the spectrum analyzers timing sweep to pass the tracking generator

output for 3 msec at the beginning of the sweep and then to gate off its output until the start of the next sweep.

An illustration of the timing and the expected signal response are shown in Fig. 1.10. The red curve shows that the amplitude of the transverse excitation of the bunch vs. time is an impulse. The expected beam response initially grows during the driving impulse, usually reaching a saturated level, and then decays exponentially after the drive is switched off (shown in the logarithmic plot as a linear decrease vs. time.) If the spectrum analyzers tracking generators frequency is tuned away from the bunchs resonant frequency, the decaying response will have periodic oscillatory beats. So during the measurement it is necessary to make small tuning adjustments to the excitation frequency to produce the most exponential decay possible.

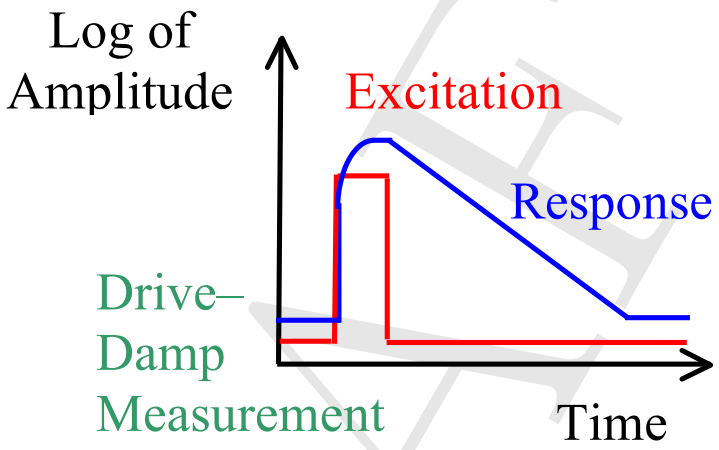

Figure 1.10: Illustration of the drive-damp measurement: The red trace is the amplitude of the excitation driving the bunch. The blue trace is the bunchs response.

The excitation of the bunch is accomplished in a somewhat different manner for the betatron dipole mode and the head-tail modes. In the both cases the spectrum analyzer is set to drive the coherent mode frequency being measured. However, for the head-tail modes it is necessary to also continuously drive the external modulation input for RF cavity phase at the synchrotron oscillation frequency. This imposes a longitudinal energy oscillation on all of the bunches within the train, causing them to uniformly shift their arrival times and displace the trains centroid horizontally proportional to the storage rings dispersion. The typical amplitude of this oscillation is relatively large, with the peak fractional energy varying as much as $\pm 7.6 \text{x} 10^{-3}$ for all of the bunches within the train and, due to the RF systems non-linearities, increases the energy spread (and bunch length) of the bunches. For the head-tail modes the added energy spread, when taken with the deflecting field from the stripline kicker, deflects the lower energy particles in the bunch (moving toward the head of the bunch) more than the higher energy particles (moving toward the tail of the bunch.) Although this is a fairly small differential effect, the bunch is being driven on the head-tail resonance allowing the oscillation amplitude to build up.

Two examples of the actual measurements are found in Figs. 1.11 and 1.12. In Fig. 1.11 the betatron dipole modes amplitude ramps up for the first 3 msec and then decays exponentially thereafter. Fig. 1.12 shows one of the head-tail modes being excited. After the drive turns off, the initial 7 dB drop represents the component of the signal, which represents the excitation of the dipole mode; the roughly exponential shape thereafter is the head-tail modes decay. If the longitudinal drive to

the RF cavitys phase were to be turned, then off the head-tail modes signal would go away.

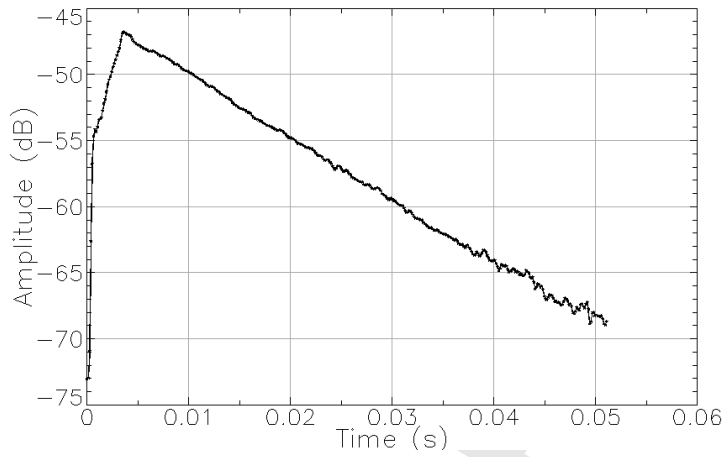

Figure 1.11: Drive-damp measurement: The trace is the response for the bunch being driven at the vertical betatron frequency. The vertical and horizontal scales are 5 dB and 10 msec per division, respectively.

This type of measurement may be very useful for understanding the behavior of bunches within the train before their motion becomes unstable. However, even though much of the data acquisition is automated, there are a few steps, which must be accomplished by the personnel taking data. In particular the fine adjustment of the spectrum analyzers frequency, centering it on the coherent modes frequency, is necessary to produce the exponential damping curve. The manual adjustment of the frequency makes this type of measurement fairly time-consuming. Routinely, after data is taken for several bunches, the beam is topped off. Beam size measurements are typically taken immediately after topping off.

1.1.5 Multi-bunch, Turn-by-turn Beam Size Measurements

1.2 Simulation Tools

1.2.1 Bunch-by-Bunch Tunes

1.2.1.1 General methodology for computing tune shifts due to the electron cloud

In this section, we discuss in a simplified form the methodology used to compute the tune shifts due to the electron cloud. We discuss only vertical motion, in a constant-β lattice. The extension to a real lattice is treated below. The generalization to the horizontal plane is straightforward.

For a constant-β lattice, and in the absence of any perturbing effects, the equation of vertical

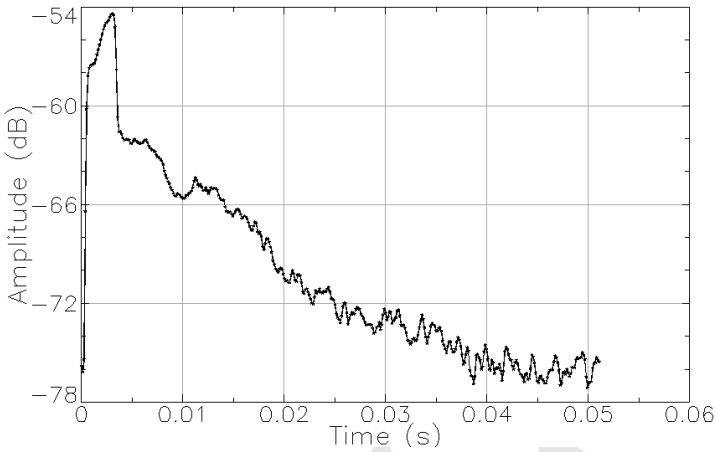

Figure 1.12: Drive-damp measurement: The trace is the response when one of the head-tail modes is excited. The vertical and horizontal scales are 6 dB and 10 msec per division, respectively.

coherent motion of the beam centroid y_b, relative to the closed orbit, is

$$\frac{d^2 y_b}{dt^2} + \omega_\beta^2 y_b = 0. \tag{1.2}$$

The betatron frequency is

$$\omega_\beta = (N + \delta_\beta)\omega_0, \tag{1.3}$$

in which N is the integral part of the tune and ω_0 is the revolution frequency.

In the presence of an electron cloud whose centroid position is y_c, which generates an electric field $E_y(y, y_c)$, the equation of motion is modified to

$$\frac{d^2 y_b}{dt^2} + \omega_\beta^2 y_b = \frac{e\langle E_y(y_b, y_c)\rangle}{m_0 \gamma}. \tag{1.4}$$

The brackets indicate an average over the beam transverse distribution, which is required to describe the coherent tune shift of the whole beam. In principle, this equation also applies for each longitudinal slice of the beam; for simplicity, we suppress that dependence here, but will include it in the final result.

For small oscillations of the beam, the presence of the cloud introduces a betatron frequency shift, which is proportional to the coefficient of y_b in a Taylor expansion of the right-hand side of this equation about $y_b = 0$.

1.2.1.2 Static cloud model

If the position of the cloud y_c is fixed, independent of y_b, then a Taylor expansion of the field about $y_b = 0$ is

$$\langle E_y(y_b, y_c)\rangle = \langle E_y(0, y_c)\rangle + y_b \frac{\partial \langle E_y(0, y_c)\rangle}{\partial y}. \tag{1.5}$$

In this case, the tune shift is proportional to the average field gradient

$$\frac{\partial \langle E_y(0, y_c)\rangle}{\partial y}$$

evaluated at the beam centroid.

In general, however, this "static cloud model" is a poor one. The electron cloud is a dynamic system, which is both generated by the beam, and also driven and focused by the beam.

1.2.1.3 Dynamic cloud model

To lowest order, the dynamic motion of the cloud can be treated in this simple model by recognizing that the position of the cloud, y_c, is in fact not independent of the position of the beam. The field depends on the beam position y_b not only directly, but also because the location and shape of the cloud depends on the beam position. This latter dependence comes about because of correlations between the given bunch and the position of previous bunches which generated the cloud, and also because the cloud can be driven and focused as the beam passes through it. The linear part of this additional dependence of the electric field on y_b will be a term in the equations of motion of the bunch which will contribute to the tune shift.

Thus, in this case the Taylor expansion should be written

$$\langle E_y(y_b, y_c(y_b))\rangle = \langle E_y(0, y_c(0)) + y_b \left.\frac{d\langle E_y(y, y_c(y))\rangle}{dy}\right|_{y=0} \tag{1.6}$$

$$= \langle E_y(0, y_c)\rangle + y_b \left(\frac{\partial \langle E_y(0, y_c(0))\rangle}{\partial y} + \frac{\partial \langle E_y(0, y_c(0))\rangle}{\partial y_c} \left.\frac{dy_c}{dy_b}\right|_{y_b=0} \right). \tag{1.7}$$

The tune shift is proportional to

$$\left(\frac{\partial \langle E_y(0, y_c(0))\rangle}{\partial y} + \frac{\partial \langle E_y(0, y_c(0))\rangle}{\partial y_c} \left.\frac{dy_c}{dy_b}\right|_{y_b=0} \right).$$

The extra term can have a significant effect. For example, suppose the beam-averaged electric field $\langle E_y(y, y_c)\rangle$ depends primarily on the difference

$$\langle E_y(y, y_c)\rangle \approx f(y - y_c). \tag{1.8}$$

Further suppose that, as is typically true in the horizontal plane in dipoles, the centroid of the cloud is closely aligned with the centroid of the beam. Finally, suppose that a train of bunches is oscillating in the lowest frequency coherent mode, for which the centroids of all the bunches are located at the same point at any position in the ring. Then the cloud generated by this train will have $y_c = y_b$, and the expression given above shows that the tune shift due to the electron cloud in the dipoles could be very small in this case. This is precisely what is observed for many of the horizontal tune measurements at CesrTA, when the train is "pinged" (i.e, excited in the lowest frequency coherent mode.)

If each bunch in excited individually, then there is no correlation between the center of the cloud generated by previous bunches, and the bunch position. In this case, $\left.\frac{dy_c}{dy_b}\right|_{y_b=0} = 0$. The total derivative is then determined (if we neglect the"pinch") just from the partial derivative of the field with respect to y, as in the static cloud model.

1.2.1.4 Tune shift from electron cloud buildup simulations

Electron cloud buildup simulation programs such as `ECLOUD` [4, 5] and `POSINST` [6, 7] can be used to compute the tune shifts approximately, using the static cloud model described above, or more accurately, using the dynamic cloud model.

Modified static cloud model. In the static cloud model, the coherent tune shifts are proportional to the field gradient generated by the electron cloud's space charge field, averaged over the beam's transverse profile. For a finite length bunch, this quantity must also be averaged over the bunch's normalized longitudinal distribution $\rho(z)$:

$$\Delta Q_y \propto \int dz \rho(z) \frac{\partial \langle E_y(0, y_c(z), z) \rangle}{\partial y}, \tag{1.9}$$

in which we have explicitly indicated the longitudinal (z) dependence of the field gradient. This field gradient can be computed from the electron cloud simulation results.

As noted above, the static cloud model is a very poor approximation. It neglects both dynamical motion of the cloud on the time scales of the bunch spacing, and also on the time scale of the bunch duration. A significant improvement to the model can be made by incorporating a dynamical correction $D(z)$ on the bunch time scale in the integral above; this correction is discussed in detail in Ref. [8]. In essence, this correction accounts for dipole motion of the cloud during the bunch traversal; that is, it includes the effect of a simple approximation for the dipole short-range wake field of the cloud on the tune shift.

The tune shift including this correction can be written

$$\Delta Q_y^* \propto \int dz \rho(z) D(z) \frac{\partial \langle E_y(0, y_c(z), z) \rangle}{\partial y}. \tag{1.10}$$

In Ref. [8], a simple model for the electron cloud wake is used to show that, for short bunches, the effect of the correction factor $D(z)$ is that the tune shift is approximately given by

$$\Delta Q_y^* \propto \frac{\partial \langle E_y(0, y_c(-\infty)), -\infty) \rangle}{\partial y} \tag{1.11}$$

in which evaluation at $z = -\infty$ corresponds to the field gradient evaluated just before the bunch enters the cloud.

We have verified[2] the approximate accuracy of Eq. 1.11 by evaluating the correction numerically using `POSINST` simulations, and comparing with results computed using the "Dynamic cloud model".

We refer to the use of Eq. 1.11 for the tune shift calculations as the "modified static cloud model". It approximately corrects for dynamic cloud motion on the time scale of the bunch duration, but not on the time scale of the bunch train.

[2] CesrTA Electron Cloud meeting notes, G. Dugan, 1/7/2009

Dynamic cloud model. An accurate estimate of the tune shift, in which all dynamic cloud effects are included, can be obtained from the electron cloud buildup simulation programs `POSINST` or `ECLOUD`, by using the option which allows the bunches to be offset in the simulations. For example, suppose that one wishes to compute the tune shift of bunch n, which interacts with a cloud generated by the preceding $n-1$ bunches in a train. The method is to perform a buildup simulation for all n bunches, in which bunch n is displaced by a small offset δ. If the train is excited in a coherent mode for which there is a correlation between the offset of the n^{th} bunch and previous bunches, this correlation must be included when the buildup simulation is done.

For example, if the lowest coherent mode of the train is excited, then all bunches should be given the same offset δ. If only bunch n is excited, then the offset of previous bunches is zero. Then, from the simulation, the beam-averaged electric field at longitudinal position z along within the length of bunch n is computed numerically: using the terminology of the preceding section (but with z dependence), this is

$$\langle E_y(\delta, y_c(\delta, z), z)\rangle$$

Another simulation is done, with the sign of δ changed. Then, the total derivative which enters into the tune shift calculation is

$$g_y(\delta, z) = \left.\frac{d\langle E_y(y, y_c(y, z), z)\rangle}{dy}\right|_{y=0} \approx \frac{\langle E_y(\delta, y_c(\delta, z), z)\rangle - \langle E_y(-\delta, y_c(-\delta, z), z)\rangle}{2\delta}. \tag{1.12}$$

The coherent tune shift is proportional to the average of this quantity over the bunch's normalized longitudinal distribution $\rho(z)$:

$$\Delta Q_y \propto G_y(\delta) = \int dz \rho(z) g_y(\delta, z). \tag{1.13}$$

The integral is to be taken over the length of the bunch. Since the full dynamical evolution of the electron cloud in response to the beam is included in the buildup simulations, including any cloud motion which occurs during the bunch, this method also accounts properly for the "pinching" that occurs during the passage of the bunch.

Ideally, the value chosen for δ is close to the actual displacement given to the beam during the tune measurement. For self-excited tune measurements, $G_y(\delta)$ should be extrapolated close to the limit $\delta \to 0$.

We refer to the use of Eq. 1.13 for the tune shift calculation as the "dynamic cloud model".

Calculation of the electric field

`POSINST` The cloud buildup code `POSINST` generates a two-dimensional distribution of macro-electrons within the vacuum chamber, which represent the electron cloud in a given magnetic environment (e.g., drift or dipole) any point in time. For each macro-electron, the beam-averaged electric field components $\langle E_x\rangle$ and $\langle E_y\rangle$ generated by the macro-electron in a vacuum chamber (i.e, including the image charges) is computed analytically, assuming a Gaussian transverse beam distribution. Then, the total electric field of the cloud is obtained by simply summing the contributions from the individual macro-electrons.

`ECLOUD` The `ECLOUD` code computes the electric field sourced by the cloud macro-electrons by first clustering them on a 81×81 Cartesian grid over a 9×5 cm region, then summing the contribution of each grid node, accounting for the boundary conditions of an elliptical vacuum chamber with semi-axes 4.5×2.5 cm by means of 50 image charges. The time-sliced cloud dynamics model includes the 2D electrostatic force from the Gaussian beam (Basseti-Erskine) and the force from any ambient magnetic field. The magnetic field kick is calculated in three dimensions, thus adding longitudinal momentum to any longitudinal components generated when the macro-electrons are produced. For the purpose of the tune shift calculations with displaced beams, the beam-averaged electric field value is calculated via a Gaussian-weighted sum of field values over a 7×7 grid spanning a $3\sigma \times 3\sigma$ region centered on the beam position.

1.2.1.5 Ring averaging

To compute the total tune shift for a particular ring and lattice, we use

$$\Delta Q_y = \frac{e}{4\pi E} \oint ds\ \beta_y(s) G_y(s). \tag{1.14}$$

in which G_y represents the field difference, computed from a cloud simulation program, as described in the previous section. s is the longitudinal coordinate around the ring. At any point s in the ring, the quantity G depends, in general, on the type of beamline magnetic environment at that location (i.e., drift, dipole, wiggler, quadrupole., etc.) and on the azimuthal distribution of radiation intensity per unit length (photons per beam particle per meter) at the point s. Let p be the normalized polar angle which measures a point on the vacuum chamber wall. If we let $N(s,p)$ be the number of photons per beam particle absorbed on the vacuum chamber at the coordinates s and p, then the distribution function of the radiation intensity is

$$D(s,p) = \frac{\partial^2 N(s,p)}{\partial s\, \partial p}. \tag{1.15}$$

Let us designate the type of element by the integer k, which runs from 1 to m, the total number of magnet types. Then, indicating all the dependencies explicitly, we write

$$G_y(s) = G_y(k, D_1(s), D_2(s), \ldots, D_P(s)), \tag{1.16}$$

where $D_i(s) = D(s,p_i)$. The quantities $D(s,p_1), D(s,p_2), \ldots, D(s,p_P)$ characterize the photon radiation angular distribution. They may correspond to

- the radiation angular distribution, evaluated at P angular points, or
- the P parameters of a fit to the angular distribution.

We define a reference value $D_{y,i}(k)$ as being equal to the β_y-weighted average of $D_i(s)$ for elements of type k:

$$D_{y,i}(k) = \frac{\int_k ds\ \beta_y(s) D_i(s)}{w_y(k)}, \tag{1.17}$$

in which the weight $w_y(k)$ is

$$w_y(k) = \int_k ds\ \beta_y(s). \tag{1.18}$$

The integral around the ring can be written as

$$\oint ds\ \beta_y(s) G_{y(s)} = \sum_{k=1}^{m} \int_k ds\ \beta_y(s) G_y(k, D_1(s), D_2(s), \ldots, D_P(s)), \tag{1.19}$$

in which we separated the ring integral into sums over integrals of the different magnetic element types.

The general dependence of G on $D_i(s)$ can be approximated as a power series. Expanding in a Taylor series about the reference values $D_{y,i}(k)$, we have, to second order,

$$\begin{aligned} & G_y(k, D_1(s), D_2(s), \ldots, D_P(s))) \approx G_y(k, D_{y,1}(k), D_{y,2}(k), \ldots, D_{y,P}(k)) \\ + & \sum_{i=1}^{P} \left.\frac{\partial G_y}{\partial D_i}\right|_{D_i = D_{y,i}(k)} (D_i(s) - D_{y,i}(k)) \\ + & \frac{1}{2} \sum_{i=1}^{P} \sum_{j=1}^{P} \left.\frac{\partial^2 G_y}{\partial D_i\, \partial D_j}\right|_{D_i = D_{y,i}(k), D_j = D_{y,j}(k)} ((D_i(s) - D_{y,i}(k)))((D_j(s) - D_{y,j}(k))) \end{aligned} \tag{1.20}$$

Integrating around the ring, and ignoring the second oder terms, we find,

$$\oint ds\ \beta_y G_y \ = \ \sum_{k=1}^{m} T_y(k) \tag{1.21}$$

where

$$\begin{aligned} T_y(k) \ &= \ G_y(k, D_{y,1}(k), D_{y,2}(k), \ldots, D_{y,P}(k)) \int_k ds\ \beta_y(s) \\ &+ \ \sum_{i=1}^{P} \frac{\partial G_y}{\partial D_i} \int_k ds\ \beta_y(s)(D_i(s) - D_{y,i}(k) \qquad (1.22) \\ &= \ G_y(k, D_{y,1}(k), D_{y,2}(k), \ldots, D_{y,P}(k)) w_y(k) \qquad (1.23) \end{aligned}$$

The second term has vanished because of the way that the reference value $D_{y,i}(k)$ is defined.

The tune shift, in this approximation, is then

$$\Delta Q_y = \frac{e}{4\pi E} \sum_{k=1}^{m} T_y(k). \tag{1.24}$$

Since we have ignored the second order terms $\frac{\partial^2 G_y}{\partial D_i\, \partial D_j}$ in the Taylor expansion, this result assumes that the field differences are strictly linear in the radiation intensities. In general, at high cloud densities for which space charge effects are important, nonlinear terms may be present. It is possible to check the accuracy of the linearity assumption, and, if necessary, include also the second order terms. We have not yet done this, but it will be done in future work.

1.2.2 Analytical Formulae for coherent instability thresholds (adapted from [1])

When the positron beam passes through the electron cloud, the electrons near the beam oscillate in the electric potential of the positron bunch. In the analytic treatment, we describe the system as

a dynamic interaction between the beam and the electron cloud, each with a transverse Gaussian distribution, and consider only the linear term of the interaction.

The motions of the beam and the electron cloud centroids are characterized by $y_b(s,z)$ and $y_e(s,t)$ at location s, longitudinal coordinate z, and time t, respectively. Note that $z<0$ for the backward direction. The equations of motion for the beam and cloud are expressed as [9]

$$\frac{d^2y_b(s,z)}{ds^2}+\frac{\omega_{\beta,y}^2}{c^2}y_b(s,z)=-\frac{\omega_{b,y}^2}{c^2}\left(y_b(s,z)-y_e(s,\frac{s-z}{c})\right), \tag{1.25}$$

$$\frac{d^2y_e(s,t)}{dt^2}=-\omega_{e,y}^2\left(y_e(s,t)-y_b(s,s-ct)\right), \tag{1.26}$$

where $\omega_{\beta,y}$ denotes the angular betatron frequency without the electron cloud interaction. The two coefficients $\omega_{b,y}$ and $\omega_{e,y}$ characterize the linearized force between beam and cloud, and are given by

$$\omega_{b,y}=\sqrt{\frac{\lambda_e r_e c^2}{\gamma\sigma_y(\sigma_x+\sigma_y)}},\quad \omega_{e,y}=\sqrt{\frac{\lambda_b r_e c^2}{\sigma_y(\sigma_x+\sigma_y)}}, \tag{1.27}$$

where λ_e and λ_b are the line densities of the cloud and the beam, r_e is the classical electron radius, c is the speed of light, γ is the beam Lorentz factor, and σ_x and σ_y are the horizontal and vertical beam sizes.

From Eq. 1.25 and Eq. 1.26, the equation of beam motion is obtained as

$$\frac{d^2y_b(s,z)}{ds^2}+\frac{\tilde{\omega}_\beta^2}{c^2}y_b(s,z)=\frac{\omega_{b,y}^2\omega_{e,y}}{c^3}\int_z^\infty dz' y_b(s,z')\sin\frac{\omega_{e,y}}{c}(z-z'), \tag{1.28}$$

where $\tilde{\omega}_\beta^2=\omega_{\beta,y}^2+\omega_{b,y}^2$ is the angular betatron frequency including the frequency shift due to the electron cloud. The right-hand side of Eq. 1.28 can be represented by a wake function, which depends only on the longitudinal distance. Integrated over the ring circumference L, the wake field $W_1(z)$ can be written as

$$W_1(z)=c\frac{R_S}{Q}\sin(\frac{\omega_{e,y}}{c}z), \tag{1.29}$$

where

$$c\frac{R_S}{Q}=\frac{\lambda_e}{\lambda_b}\frac{L}{\sigma_y(\sigma_x+\sigma_y)}\frac{\omega_{e,y}}{c}. \tag{1.30}$$

This wake field does not damp in z in this model. Actually the electron frequency $\omega_{e,y}$ has a finite spread, since the frequency of each electron depends on its oscillation amplitude and the horizontal position of the electron. This nonlinear effect causes the oscillation of the electrons to damp. If we added a damping term $2\alpha y_e$ in the left-hand side of Eq. 1.26, the wake field $W_1(z)$ is expressed by

$$W_1(z)=c\frac{R_S}{Q}\frac{\omega_{e,y}}{\tilde{\omega}}\exp(\frac{\alpha}{c}z)\sin(\frac{\tilde{\omega}}{c}z), \tag{1.31}$$

where the damping factor $\alpha=\omega_{e,y}/2Q$ is related to the frequency spread of $\omega_{e,y}$ and $\tilde{\omega}=\sqrt{\omega_{e,y}^2-\alpha^2}$. In a nonlinear resonator model, the wake field due to the electrons has a finite quality factor $Q=Q_{nl}$. From comparisons with numerical simulations [9], the nonlinear resonator quality factor is estimated to be $Q_{nl}\sim 7$.

The single-bunch instability is caused by the wake effect of electron motion with the frequency $\omega_{e,y}$. The phase angle of the electron oscillation during the passage of the bunch is characterized by

$$\chi = \frac{\omega_{e,y}\sigma_z}{c}, \tag{1.32}$$

where σ_z is the bunch length. The nature of the instability depends on the phase factor, χ.

The corresponding effective transverse impedance is given by a Fourier transformation of the wake function,

$$Z_\perp(\omega) = i\int_{-\infty}^{\infty}\frac{dz}{c}\exp(-\frac{i\omega z}{c})W_1(z). \tag{1.33}$$

From Eq. 1.31 and Eq. 1.33, the resonator impedance is expressed by

$$\begin{aligned} Z_\perp(\omega) &= \frac{c}{\omega}\frac{R_S}{1+iQ(\frac{\omega_{e,y}}{\omega}-\frac{\omega}{\omega_{e,y}})} \\ &= \frac{\lambda_e}{\lambda_b}\frac{L}{\sigma_y(\sigma_x+\sigma_y)}\frac{\omega_{e,y}}{\omega}\frac{Z_0}{4\pi}\frac{Q}{1+iQ(\frac{\omega_{e,y}}{\omega}-\frac{\omega}{\omega_{e,y}})}, \end{aligned} \tag{1.34}$$

where Z_0 is the vacuum impedance 377 Ω.

We can estimate the stability requirement for a positron beam which experiences this effective impedance. For $\chi > 1$, the coasting beam model is available to study the fast head-tail instability. For zero chromaticity, the stability criterion is given by the dispersion relation as [10]

$$\begin{aligned} U &= \frac{\sqrt{3}\lambda_b r_e\beta_y}{\gamma\nu_s\omega_{e,y}\sigma_z/c}\frac{|Z_\perp(\omega_{e,y})|}{Z_0} \\ &= \frac{\sqrt{3}\lambda_b r_e\beta_y}{\gamma\nu_s\chi}\frac{Q}{4\pi}\frac{\lambda_e}{\lambda_b}\frac{L}{\sigma_y(\sigma_x+\sigma_y)} = 1, \end{aligned} \tag{1.35}$$

where ν_s is the synchrotron tune, β_y is average vertical beta function. For $U > 1$, the beam becomes unstable.

The number of electrons in the beam cross-section area, λ_e, is $2\pi\rho_e\sigma_x\sigma_y K$ [11], where ρ_e is the density of the electron cloud. The electrons are gathered around the positron beam path by the electric force produced by the circulating positrons. Due to the pinch effect, the number of electrons, which contributes to the instability, is enhanced by a factor K, where K should depend on χ. This stability condition gives the threshold of the electron density for the instability as

$$\rho_{e,th} = \frac{2\gamma\nu_s\chi}{\sqrt{3}KQr_e\beta_y L}. \tag{1.36}$$

For a finite bunch length, the quality factor should not be larger than χ. Thus $Q = \min(Q_{nl}, \chi)$ is used. And $K = \chi$ is chosen as a simple model.

For a long bunched beam, the Landau damping rate per turn is given by [10]

$$\frac{\nu_s\omega_{e,y}\sigma_z}{c} = \frac{\alpha\sigma_\delta\omega_{e,y}}{\omega_0}, \tag{1.37}$$

where α is the momentum-compaction factor, σ_δ is the rms relative momentum spread, and ω_0 is the revolution frequency. From From Eq. 1.36 and Eq. 1.37, we can get the relationship between the threshold density and momentum-compaction factor as

$$\rho_{e,th} = \frac{2\gamma\alpha\sigma_\delta\omega_{e,y}}{\sqrt{3}KQr_e\beta_y\omega_0 L}. \tag{1.38}$$

A high momentum-compaction factor suppresses the fast head-tail instability.

The tune shift induced by the electric focusing force for a certain electron cloud density is given by [8]

$$\Delta\nu_{x+y} = \Delta\nu_x + \Delta\nu_y = \frac{r_e}{\gamma}\rho_e\beta L, \tag{1.39}$$

where ν_x and ν_y are the horizontal and vertical betatron tunes and ρ_e is the electron cloud density.[3] The averaged beta function in the horizontal and vertical is assumed the same and denoted as β in the above equation.

1.2.3 Simulation of beam response to the Electron Cloud using CMAD

`CMAD` is a many-particle systems program to simulate the transport of charge particle beams in an accelerator lattice in the presence of electron cloud interaction [3]. The program tracks the beam across the full lattice of the accelerator, while computing the beam-electron cloud interactions within every element of the lattice. The lattice representation may be imported from any standard accelerator program such as `MAD` [12] in the form of transfer maps. The interaction between the beam and electron cloud is modeled using the particle-in-cell (PIC) algorithm. `CMAD` runs on multiple processors and is optimized for speed in computation. `CMAD` has been validated against two other programs that perform similar calculations [13], namely `HEADTAIL` [5] and `WARP` [14].

1.2.3.1 Representation of the lattice for the purpose of tracking

While computing the beam electron cloud interactions, it is important to correctly model the effect of the variation of the twiss function around the ring. The beta function as well as the dispersion influences the distribution of the particles comprising the beam. This determines how the electron cloud distribution evolves during a bunch passage, described by the so called pinching process. This pinching process in turn influences the beam response to the cloud. Thus, it is important to take into account these details rather than use a constant focusing model, although the latter would greatly simplify the simulation process. Before starting the computation, the beam distribution needs to be matched to the twiss functions at the point where the tracking begins. The macro-particles comprising the beam are then propagated across each element based on transfer functions obtained from the lattice description. Coupled with the tracking through the lattice elements the beam particles would undergo an "electron cloud kick", which is described later in this subsection.

The longitudinal phase space coordinates are defined by δ, the relative energy offset and z, the position along the bunch. To match the distribution in this degree of freedom, the coordinates are assigned to each particle as follows.

$$\begin{vmatrix} z \\ \delta \end{vmatrix} = \begin{vmatrix} \frac{c|\eta|\sigma_\delta}{\omega_s} & 0 \\ 0 & \sigma_\delta \end{vmatrix} \begin{vmatrix} z_G \\ \delta_G \end{vmatrix} \tag{1.40}$$

where c is the speed of light, ω_s is the angular synchrotron frequency and η is the slippage, σ_δ is the equilibrium relative energy spread. The quantities z_G and δ_G are assigned to each particle using a Gaussian distribution random generator with a standard deviation of unity over all the particles. We have assumed that the relativistic parameter $\beta_0 = v_0/c \approx 1$. The transverse phase

[3] This is the same as Eq. 1.58.

space coordinates are defined by x the horizontal position, x' the horizontal angle, y the vertical position and y', the vertical angle. For a matched distribution the particles are chosen in order to satisfy the following relationship,

$$\begin{vmatrix} x \\ x' \end{vmatrix} = \sqrt{\frac{\epsilon_x}{\beta_x}} \begin{vmatrix} \beta_x & 0 \\ -\alpha_x & 1 \end{vmatrix} \begin{vmatrix} x_G \\ x'_G \end{vmatrix} + \delta \begin{vmatrix} D_x \\ D_{x'} \end{vmatrix} \tag{1.41}$$

$$\begin{vmatrix} y \\ y' \end{vmatrix} = \sqrt{\frac{\epsilon_y}{\beta_y}} \begin{vmatrix} \beta_y & 0 \\ -\alpha_y & 1 \end{vmatrix} \begin{vmatrix} y_G \\ y'_G \end{vmatrix} + \delta \begin{vmatrix} D_y \\ D_{y'} \end{vmatrix} \tag{1.42}$$

where $\beta_{x/y}$, $\alpha_{x/y}$, $D_{x/y}$, $D_{x'/y'}$ are the horizontal/vertical values of the beta function, the alpha function, the dispersion and dispersion gradient respectively at the given position in the lattice the distribution is matched to. Also, $\epsilon_{x/y}$ is the horizontal/vertical beam emittance. The quantities x_G/y_G and x'_G/y'_G are assigned to each particle using a Gaussian distribution random generator with a standard deviation of unity over all the particles. The particle distribution is truncated along each axis at a pre-specified value given by an integer multiple of the root mean square (rms) extent of the full distribution.

The tracking across the lattice elements is done with the help of transfer functions as specified in Ref [15]. These include first order transfer matrices and higher order phase space tensors. The transfer across each element may be expressed as

$$v_i^{(2)} = \sum_{j=1}^{6} R_{ij} v_j^{(1)} + \sum_{j=1}^{6} \sum_{k=1}^{6} T_{ijk} v_j^{(1)} v_k^{(1)} \tag{1.43}$$

where v_i is the set of components of the phase space vectors in six dimensions, R_{ij} are the components of the matrix elements representing linear transport and T_{ijk} are the components of the third order tensor representing nonlinear transport. The set of components in R_{ij} for the all the lattice elements provide all the effects of the linear beam optics, which include the influence of twiss functions on the size of the distribution, the betatron tune and the slippage undergone by the off energy particle. Based on a pre-specified synchrotron tune, the particles undergo a kick in energy at every turn, which is analogous to an RF cavity. This provides for longitudinal confinement and the synchrotron oscillations executed by the particles. The formulation of this kick is given by

$$\delta^{(2)} = \frac{(2\pi Q_s)^2}{\eta C} z + \delta^{(1)} \tag{1.44}$$

where Q_s is the synchrotron tune, and C the circumference of the ring.

The combined effect of the T_{ijk} tensors from all the elements provide for higher order effects in the beam optics. These include the natural chromaticity and correction of the same due to sextupoles. Other less important features provided by the terms T_{ijk} include higher order dispersion and momentum compaction. Yet another effect would be the quadrupole component arising from a sextupole for an off centered orbit. It may be noted that the T_{ijk} tensors break simplecticity in the beam transport. Loss in siplecticity would lead to violation of conservation of phase space area, leading to artificial damping and particle excursion especially when tracking the beam over several thousands of turns. However, chromaticity is a key higher order effect that needs to be retained in any computation of electron cloud effects on the dynamics of beams in storage rings. Chromaticity is defined by gradient of betatron tune with respect to energy offset, which is given by $Q' = dQ/(dp/p)$, where Q' is the chromaticity, Q the betatron tune and p the momentum of the

synchronous particle. These higher order effects vanish in the absence of the T_{ijk} tensors acting on the particles. In order to circumvent this problem, one can retain only the first order terms in the tracking scheme, that is the R_{ij}, thus retaining the symplectic structure of the beam transport, and yet model the chromaticity with the help of a single transfer matrix applied once per turn. If we define the transverse space variables (x, x', y, y') as t_i and the corresponding momentum dispersion component as D_i, then we may express the chormaticity transformation as

$$t_i^{(2)} = \sum_{j=1}^{4} C_{ij} t_j^{(1)} - \sum_{j=1}^{4} (C_{ij} + I_{ij}) D_j \delta \tag{1.45}$$

where I_{ij} is the respective component of the identity matrix $\mathbf{I}$ and C_{ij} that of a matrix given by

$$\mathbf{C} = \begin{vmatrix} \mathbf{Cx} & \mathbf{I} \\ \mathbf{I} & \mathbf{C_y} \end{vmatrix} \tag{1.46}$$

with

$$\mathbf{C_x} = \begin{vmatrix} \cos(Q'_x\delta) + \alpha_x \sin(Q'_x\delta) & \beta_x \sin(Q'_x\delta) \\ \frac{1+\alpha_x^2}{\beta_x} \sin(Q'_x\delta) & \cos(Q'_x\delta) - \alpha_x \sin(Q'_x\delta) \end{vmatrix} \tag{1.47}$$

and

$$\mathbf{C_y} = \begin{vmatrix} \cos(Q'_y\delta) + \alpha_y \sin(Q'_y\delta) & \beta_x \sin(Q'_y\delta) \\ \frac{1+\alpha_y^2}{\beta_y} \sin(Q'_y\delta) & \cos(Q'_y\delta) - \alpha_y \sin(Q'_y\delta) \end{vmatrix} \tag{1.48}$$

Simulations performed so far with `CMAD` have used first order tracking along with chromaticity modeled according the transformation described above.

1.2.3.2 Modeling the beam - electron cloud interaction

The general method of modeling the beam transport through the ring with electron cloud effects involves tracking a certain number of beam particles around the ring with the help of transfer maps as already described above, coupled with discrete "electron cloud interacting points" (IPs) in the ring. `CMAD` allows one to have an IP within each element with a pre-specified electron density. These IPs provide the kick, or deviation in momentum due to the electron cloud.

The beam is divided into a certain number of slices along the length of the bunch. The charge from each particle is deposited on to adjacent slices, represented by two dimensional grids extending transversely. The electron cloud at the IP is represented by a single slice, which translates to charge deposited onto a single two dimensional grid. Since each IP represents a certain length along the transport channel, this would be equivalent to a situation where all the electrons along this length are collapsed on to a single two dimensional grid. After such a decomposition, one is left with computing the interaction between a set of two dimensional charge distributions, namely the sliced beam and a single two dimensional charge distribution, namely the electron cloud. This is done with the help of a field solver and particle pusher method prescribed by the two dimensional particle-in-cell (PIC) algorithm described further in this subsection. All the forces and motion of particles are now purely transverse to the beam propagation. It is easy to justify such an approximation because the beam is ultra relativistic. As a result the electrons would experience, for all practical purposes, only a transverse field component. On the other hand, the electrons, which extend over a finite length will not have a significant longitudinal field component to perturb the motion of an ultra relativistic beam. Thus, longitudinal field components may be disregarded altogether. The

self field forces of each species acting upon themselves are also disregarded. Given the beam is ultra relativistic, we know that beam space charge forces acting upon the beam particles is insignificant. One can determine this by transforming the fields to the rest frame of the beam, or by calculating the combined effect of the electric and magnetic fields in the rest frame of the laboratory, where the forces due to the electric and magnetic fields almost cancel each other. The space charge forces due to the electrons acting upon the electrons may also be disregarded. This is because, electron densities are of the order of $10^{11} - 10^{12} m^{-3}$ while the beam consists of about 10^{10} particles confined within micron sized dimensions transversely and about a centimeter longitudinally. Thus, within the vicinity of the beam, the forces exerted by the beam space charge on the electrons is many orders of magnitude higher than the forces of the electrons acting upon each other.

In this scheme, the transverse fields produced in each of the beam slices are first computed. These slices are made to pass through the two dimensional electron distribution in succession, and the electrons are made to move accordingly with every slice passage. With a positively charged beam, the electrons would converge toward the center as the beam slices pass through and in some cases even overshoot and cross the center. This process is often referred to as "pinching". The field produced by the electrons is computed and recorded after every interaction with a beam slice or, in other words after every pinch introduced by the respective slice. Finally, these computed fields due to the electrons are acted upon the beam particles of the corresponding slice. This provides focusing to the beam particles in addition to focusing arising from the quadrupoles. The focusing caused by the electrons is not uniform leading to an amplitude dependent tune shift over a coherent tune shift. Since the beam is not rigid in this model, *ie*, it consists of discrete particles, one can study effects such as emittance growth caused by the electron cloud, distortions in beam shape and orientation due to head-tail interaction, the spread in tune amongst the particles and other such effects that cannot be seen by a rigid beam model.

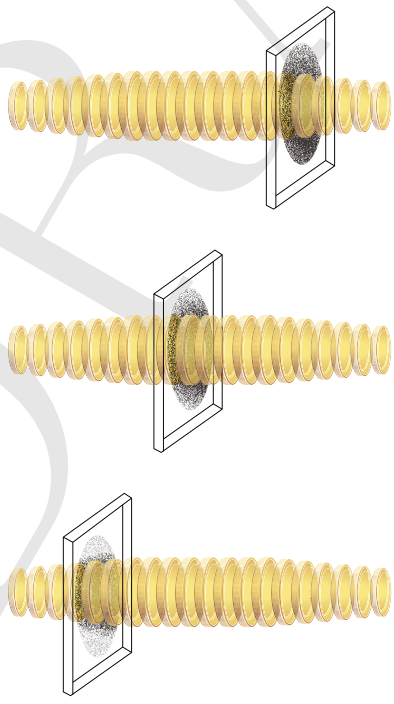

Figure 1.13: Figure describing the pinching of the cloud as the slices of the beam pass through the two dimensional cloud

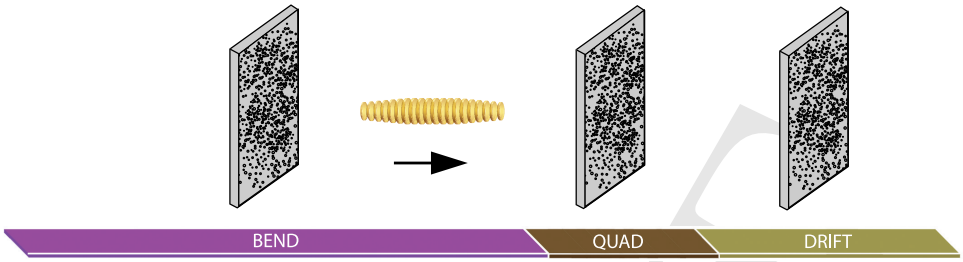

Figure 1.14: Figure describing the distribution of the two dimensional cloud slices across each element, which represents an IP

1.2.3.3 Particle-in-Cell (PIC) algorithm

The (PIC) method has been widely used in simulating many particle systems. The general method involves solving for the force fields over a mesh, and moving particles in the system based on the field calculation, a process repeated at every time step. In our case the force fields are computed by solving a two dimensional Poisson's equation over a mesh using Fourier transforms. As explained earlier, the fields need be solved over a two dimensional grid. Poisson's equation in two dimensions is

$$\frac{\partial^2\phi}{\partial x^2} + \frac{\partial^2\phi}{\partial y^2} = -\frac{\rho}{\epsilon_0}. \tag{1.49}$$

In general, the above equation may be solved in Fourier space, where it reduces to a simple equation rather than a differential one, and then taking the inverse Fourier transforms to determine ϕ. In the present case, since all values are given over a mesh, we use the discrete Fourier transform (DFT). The DFTs and their inverses are computed using the package `FFTW` [16]. The area used in the field computation spans to about 10-20 times the beam size, which is much smaller than the vacuum chamber cross section. In order for the field computation to be unaffected by these artificial boundaries, the boundary conditions are set so that it creates the effect of "open boundaries". This is done by first computing the field on the boundary nodes using Green's function for open boundaries due to the charge present in the computational domain. Using these values as boundary conditions, Poisson's equation is solved for all grid points within these boundaries using fast Fourier transforms (FFT). The charge distribution is represented by a set of macro-particles, which are computational particles carrying the weight of a finite number of physical particles. At a given time a macro-particle can be located anywhere within the computational domain. In order to solve Poisson's equation using DFTs, one needs to assign the charge of these macro-particles onto the grid nodes. Additionally, once the fields are computed, their values need to be interpolated onto the position of the particles. The schemes used for evaluating the fields from the potential by discretizing the gradient operator, the Laplacian operator to express Poisson's equation, interpolation of charge onto the nodes, interpolation of the field from the node to the particle position are all similar to that described in Ref [17]. They are briefly summarized here.

The assignment of the charge onto the grid nodes is done over a set of nine nearest neighboring points representing the nodes as shown in Fig 1.15. We use 0 to denote the first, + as the second, and − as the third nearest lines. Following the notation of Ref [17], we define H_x as the horizontal dimension of the grid and H_y as the vertical dimension. Also δx and δy are defined as the perpendicular distance from the nearest horizontal and vertical grid line respectively. The weights assigned to these nine nodes are quadratic polynomials of the ratios $r_x = \delta_y/H_y$ and $r_y = \delta_y/H_y$. The

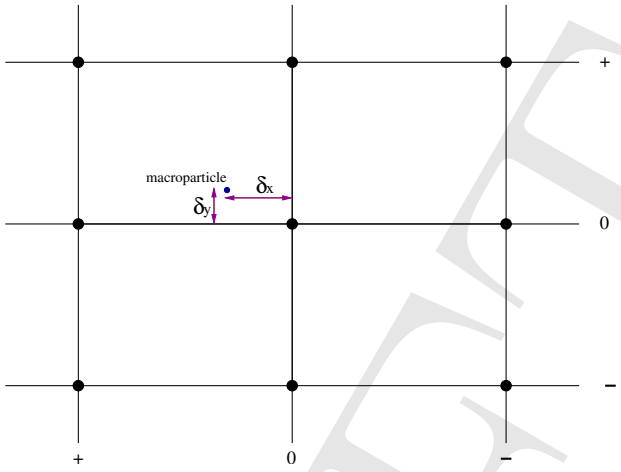

Figure 1.15: Figure illustrating the 9 point charge interpolation scheme

coefficients of the weights along the x axis are given by

$$\begin{aligned} w_x^0 &= \frac{3}{4} - r_x^2 \\ w_x^+ &= \frac{1}{2}(\frac{1}{4} + r_x + r_x^2) \\ w_x^- &= \frac{1}{2}(\frac{1}{4} - r_x + r_x^2) \end{aligned} \tag{1.50}$$

It may be noted that $w_x^0 + w_x^+ + w_x^- = 1$, which is required for satisfying charge conservation. The formulation for weighing the charges along the y axis is identical, and are denoted as w_y^0, w_y^+ and w_y^- respectively. Finally, the weight to be assigned at a node will be a product of the two one-dimensional weights based on the position of the node along the two axis. For example $w^{00} = w_x^0 w_y^0$ and $w^{+-} = w_x^+ w_y^-$ etc. The two dimensional Laplacian operator is approximated by a five point difference scheme, and Poisson's equation is discretized as follows,

$$\frac{\phi_{i-1,j} + \phi_{i+1,j} - 2\phi_{i,j}}{H_x^2} + \frac{\phi_{i,j-1} + \phi_{i,j+1} - 2\phi i, j}{H_y^2} = -\frac{\rho_{i,j}}{\epsilon_0} \tag{1.51}$$

where i and j are the horizontal and vertical indices that label the nodes over the mesh. The field is computed from the potential using the gradient operator which is approximated by a six point difference scheme. This is given by

$$\begin{aligned} E_{xi,j} &= -\frac{1}{12H_x}[(\phi_{i+1,j+1} - \phi_{i-1,j+1} + 4(\phi_{i+1,j} - \phi_{i-1,j}) + (\phi_{i+1,j-1} - \phi_{i-1,j-1})] \\ E_{yi,j} &= -\frac{1}{12H_y}[(\phi_{i+1,j+1} - \phi_{i+1,j-1} + 4(\phi_{i,j+1} - \phi_{i,j-1}) + (\phi_{i-1,j+1} - \phi_{i-1,j-1})]. \end{aligned} \tag{1.52}$$

Once the force on each of the particles is computed, their positions and velocities are advanced in time according to the values of the time step and the force exerted. In order to do this, we use the leap frog scheme when the effect of an external magnetic field is not included and the Boris [18]

integrator when the particles are influenced by an external magnetic field. The particles equations of motion to be integrated are

$$\begin{aligned} m\frac{d\mathbf{v}}{dt} &= q(\mathbf{E}+\mathbf{v}\times\mathbf{B}) \\ \frac{d\mathbf{r}}{dt} &= \mathbf{v}. \end{aligned} \tag{1.53}$$

The only situation where a nonzero magnetic field $\mathbf{B}$ is taken into account is when electron cloud particles move in the presence of a dipole field. For $\mathbf{B}=0$, the discretized integartion is given as follows,

$$\begin{aligned} \mathbf{v}_{t+\Delta t/2} &= \mathbf{v}_{t-\Delta t/2} + \frac{q}{m}\mathbf{E}_t\Delta t \\ \mathbf{r}_{t+1} &= \mathbf{r}_t + \mathbf{v}_{t+\Delta t/2}\Delta t \end{aligned} \tag{1.54}$$

Thus, we see that in this scheme, the position and velocity coordinates are always half a time step apart. In the presence of an external magnetic field, we need to solve

$$\frac{\mathbf{v}_{t+\Delta t/2}-\mathbf{v}_{t-\Delta t/2}}{\Delta t} = \frac{q}{m}\left[\mathbf{E}_t + \frac{\mathbf{v}_{t+\Delta t/2}+\mathbf{v}_{t-\Delta t/2}}{2}\times\mathbf{B}\right] \tag{1.55}$$

To do this, we follow the method of Boris [18] which involves the following expressions,

$$\begin{aligned} \mathbf{v}_{t-\Delta t/2} &= \mathbf{v}^- - \frac{q\mathbf{E}_t}{m}\frac{\Delta t}{2} \\ \mathbf{v}_{t+\Delta t/2} &= \mathbf{v}^+ + \frac{q\mathbf{E}_t}{m}\frac{\Delta t}{2} \end{aligned} \tag{1.56}$$

If we substitute the above expressions into 1.55, we get

$$\frac{\mathbf{v}^+-\mathbf{v}^-}{\Delta t} = \frac{q}{2m}(\mathbf{v}^++\mathbf{v}^-)\times\mathbf{B} \tag{1.57}$$

Thus, in order to advance the velocity in time, we need to carry out the following procedure; first compute $\mathbf{v}^-$ according to Eq (1.56) using the value of $\mathbf{E}_t$, then solve for $\mathbf{v}^+$ using Eq (1.57), and then solve for $\mathbf{v}_{t+\Delta t/2}$ once again using $\mathbf{E}_t$ and Eq (1.56). The position vector $\mathbf{r}$ is advanced in the same manner as in the zero magnetic field case.

1.2.3.4 Parallel implementation

As mentioned previously, `CMAD` has been optimized for high speed computation and runs on multiple processors. In this algorithm, each processor contains the particle distribution of one or more of the beam slices. The electrons are first moved, or pinched according to the fields produced by the beam particles of each of the slices. This is done one slice after another. After this process is completed for all the slices in one processor, a copy of the resulting electron distribution is passed onto the processor containing the adjacent slices and the pinching processor is continued. Following the pinching process from each slice, the resulting field produced by the electrons is computed and the beam particles then receive the "electron cloud kick" accordingly. This is followed by propagating each particle to the next element by applying the transfer map described earlier in the subsection. It may be noted that the process of providing the "electron cloud kick" and transportation to the next element in the lattice can be done by each processor independently, which results in considerable

saving in overall computation time when several processors are used. It is clear that optimal speed in computation is achieved when the number of processors used equals the number of slices the beam is divided into. Figure 1.16 shows a schematic describing this algorithm with each processor containing three slices. Calculations for CesrTA are regularly carried out with 100 slices using 100 processors at the National Energy Research Scientific Computation Center (NERSC).

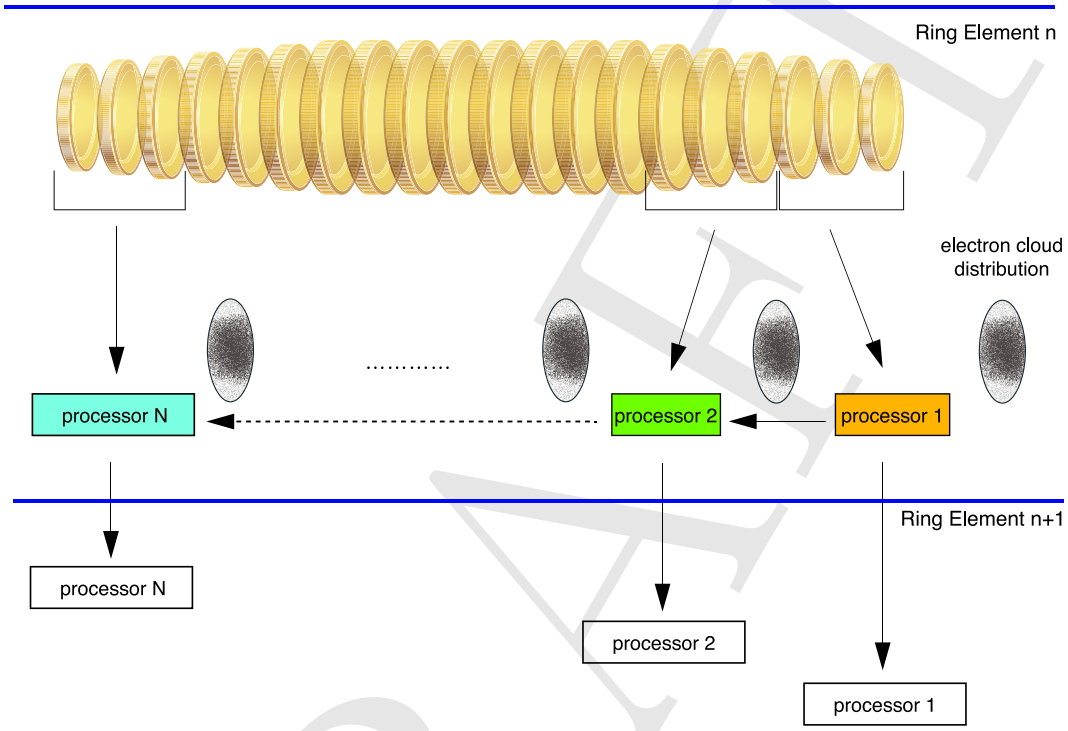

Figure 1.16: Figure illustrating the algorithm for parallel computation implemented in `CMAD`

1.3 Experimental Observations and Comparison With Simulation

1.3.1 Bunch-by-Bunch Tunes

The CesrTA program has included extensive measurements of bunch-by-bunch coherent betatron tune shifts for a variety of electron and positron beam energies, emittances, bunch population levels, and bunch train configurations [19–21]. The tune shift measurement methods are described in Section 1.1.2.

Comparisons to two advanced electron cloud simulation codes (`ECLOUD` [4, 5] and `POSINST` [6, 7]), using the methods described in Section 1.2.1, have shown that the bunch-by-bunch tune shifts result primarily from the interaction of the beam with the space-charge field of the photoelectron-seeded electron cloud in the vacuum chamber. These comparisons have allowed the accuracy of the codes to be checked, and constraints to be placed (for the conditions of the CesrTA vacuum chamber) on the codes' physics model parameters. Together with local direct measurements of the electron cloud using retarding field analyzers, shielded buttons and TE-waves, described in Chapter **??**, the tune shift measurements will help to develop a robust electron cloud model, well tested experimentally, which can be used to predict with confidence the features of the electron cloud effect in future linear collider damping rings.

1.3.1.1 General remarks on bunch-by-bunch tune shifts

The basic tools required for simulations of the bunch-by-bunch coherent tune shifts are

1. knowledge of the beam parameters, element layout and lattice, vacuum chamber characteristics, and radiation distribution (including scattered radiation) around the ring.

   We have detailed optics models for each CesrTA lattice configuration. For our tune shift simulations in 2008 through 2011, the radiation intensity for a given beam current was provided by a program called `SYNRAD`, which computes the radiation intensity striking the vacuum chamber wall (approximately a 4.5 cm $\times$ 2.5 cm elliptical Al beampipe) in the bend plane from the magnetic lattice and the beam parameters. An empirically determined "Photon reflectivity" parameter is used in the electron cloud codes to describe the scattered radiation (assumed to be uniformly distributed) striking the vacuum chamber out of the bend plane.

   As discussed in Section **??**, we have been developing a three-dimensional radiation propagation code called `SYNRAD3D` which computes the radiation intensity per unit beam current in a given lattice, including specular photon scattering in a realistic 3D model of the CesrTA vacuum chamber. This code gives the complete photon radiation distribution around the perimeter of the vacuum chamber, at any longitudinal position. We will use the results of this code to improve the tune shift simulations in future studies. Some preliminary tune shift comparisons based on `SYNRAD3D` are presented below in Section 1.3.1.7.

2. a program which uses primary photoelectron and secondary electron models to simulate the buildup of the cloud.

   We have used the 2D codes `POSINST` and `ECLOUD` to model the cloud buildup along a bunch train, and decay after the end of the train. A description of recent benchmarking comparisons between `ECLOUD` and `POSINST` can be found in Ref. [22]. For the tune shift calculations, the

electron cloud has been modeled in drifts and dipoles only, since electron cloud effects in these elements dominate the bunch-by-bunch tune shifts in the CesrTA ring.

The 3D codes `WARP/POSINST` [23, 24] and `CLOUDLAND` [25–27] have been employed to study tune shifts in quadrupoles and wigglers. The contributions to the bunch-by-bunch tune shift differences along the train from these elements is generally quite small; however, because of the presence of trapped cloud in these devices, there may be observable effects on the tune shifts of the leading bunch in a train, and on other features of the beam dynamics (see below, Section 1.3.2.15). This is an area to be studied in the future.

Further details concerning the modeling of photoelectron production are discussed in Section **??**, and also below in Section 1.3.1.7. Additional information, as well as the detailed assumptions in the secondary electron yield model, can be found in Refs. [21, 28].

3. a method of calculating the coherent tune shifts from the (dynamic) electron cloud charge densities provided by the simulation codes. This is described above in Section 1.2.1.

1.3.1.2 Initial tune shift studies to determine the reference simulation parameter values

To determine the approximate values of the electron cloud simulation parameters which reproduced measured tune shift data, a data set from 2007 was studied intensively. The radiation intensities in drifts and dipoles were fixed as computed from the lattice and the beam current. Starting with a parameter set suggested by recent direct measurements of the SEY properties of technical Al surfaces at SLAC, the internal simulation parameters in the `POSINST` code were varied. A reference parameter set, which did the best job of reproducing the 2007 data set, was determined by trial-and-error comparisons. The numerical parameters of the `POSINST` simulation (such as time step size, space charge grid size, and number of beam slices) were chosen such that variations in these numerical parameters did not change the results of the simulation significantly.

The reference values for six key parameters for the simulations are shown in Table 1.1. Fig. 1.17 shows a comparison between the 2007 data set and a `POSINST` simulation with the reference values, and two simulations with the total secondary yield parameter varied by ±10% away from the reference.

Table 1.1: `POSINST` initial reference parameter values (aluminum chamber). The same values are used for drifts and dipoles.

`POSINST` Parameter	Description	Unit	Value
`queffp`	Quantum efficiency	%	12
`refleff`	Photon reflectivity	%	15
`ek0phel`	Peak photoelectron energy	eV	5
`eksigphel`	RMS photoelectron energy	eV	5
`E0tspk`	Energy of peak true secondary yield	eV	310
`dtotpk`	Peak total secondary yield		2.0
`P1epk`	Elastic yield at zero energy		0.5
`P1rinf`	Rediffused yield at high energy		0.19

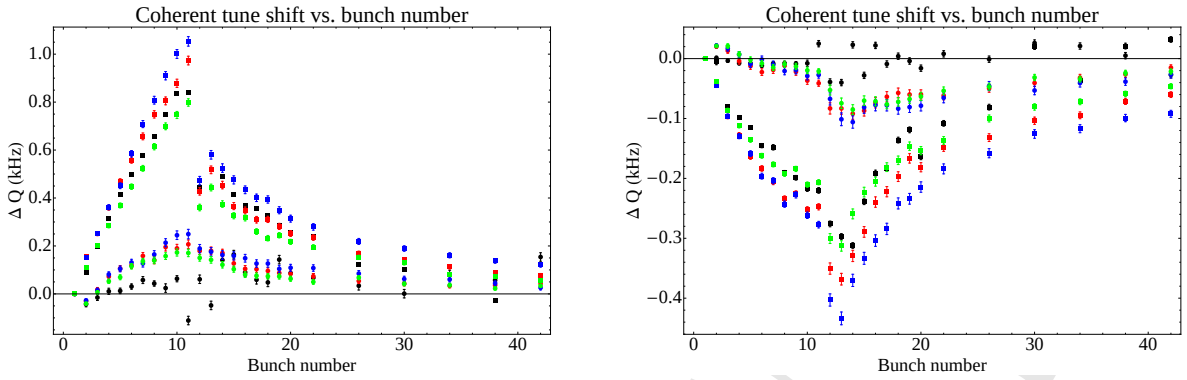

Figure 1.17: Coherent tune shifts, 2007 1.9 GeV data and `POSINST` simulations compared. Left: positron beam. Right: electron beam. The data and simulations are for a 10 bunch train with a bunch current of 0.75 mA, followed by witness bunches, all with 14 ns spacing, and 1.9 GeV beam energy. Squares: Vertical tune shift. Disks: Horizontal tune shift. Black: data. Red: `POSINST` simulation using parameters given in Table 1.1. Blue: `POSINST` simulation with Table 1.1, except peak total secondary yield = 2.2. Green: `POSINST` simulation with Table 1.1, except peak total secondary yield = 1.8.

1.3.1.3 Tune shift data summary, and comparison with `POSINST` simulations

A large variety of coherent tune shift data exist, covering a wide range of machine conditions such as beam energy, beam size, lattice configuration, particle species, bunch current, bunch train configuration, and mode of oscillation of the bunches.

The tune shift data can be grouped into four types based on the measurement technique employed:

a. "Pinged" beam measurements, for which all the bunches in the train are oscillating in phase. This measurement type is described in Section 1.1.2.1. For this mode of excitation, the horizontal tune shifts are suppressed, as discussed above in Section 1.2.1.3.

b. Measurements in which a single bunch in the train is excited with a fast kicker. This measurement type is described in Section 1.1.2.2.

c. Measurements in which the Dimtel feedback system response is used to measure the tune. In this case, the mode of oscillation of the train is unknown. This measurement type is described in Section 1.1.2.3.

d. Measurements in which the bunches in the train are self-excited; in this case also, the mode of oscillation of the train is unknown. This measurement type is described in Section 1.1.2.4.

For each of these measurement types, there are also two possible kinds of bunch patterns:

- Measurements involving witness bunches, which are single bunches placed at a variable time after the end of a train, to probe the time evolution of the cloud. For these studies, the train lengths were typically short (no more than 20 bunches).
- Measurements with long trains of bunches (up to 45 bunches), with no witnesses.

As discussed above in Section 1.2.1.3, the tune shifts depend in general on the mode of oscillation of

the train, and this dependence can be taken into account by using the "Dynamic cloud model." For type *a* data, all the bunches in the train are oscillating in phase, and the cloud buildup simulations done for comparisons with type *a* data were done by offsetting all the bunches in the train by the same amount. The offset used in the simulations was 2 mm.

For data type *b*, only a single bunch in the train is oscillating. The corresponding simulation should be done using the "Dynamic cloud model" with a single bunch offset. Simulation studies have shown, however, that when only a single bunch in the train is offset by a small displacement ($\lesssim$ 0.5 mm), tune shifts computed using the "Modified static cloud model" (Section 1.2.1.4) are close to those computed using the "Dynamic cloud model". For the simulations reported here for this data type, we have used the "Modified static cloud model" (Eq. 1.11). In the future, we will use the "Dynamic cloud model" (with a single bunch offset equal to the displacement used for the measurement) for data type *b* as well as data type *a*.

For data types *c* and *d*, the excitation of the beam is spontaneous, and the mode of oscillation is not directly measured. However, it is believed that the dependence of the tune shift on the mode of oscillation of the train is relatively weak[4], except for the special case of the horizontal tune shift in dipoles being very small for the lowest frequency multibunch mode. This belief is supported by horizontal tune spectra measurements for type *d* data, such as shown in Fig. 1.37 below. The spectrum exhibits two peaks: one smaller peak at very small tune shifts, associated with the lowest frequency multibunch mode, and another larger peak with a large tune shift, associated with all the other modes. Thus, by focusing on the frequency of the largest amplitude spectral peak, we are measuring the tune shift associated with the higher frequency multibunch modes. To compute the tune shift for the these modes, we use the "Modified static cloud model".

The major tune measurement data sets, grouped by measurement type, are the following:

type *a*: *1a.* A large series of data sets taken in 2007 and 2008, with witness bunches and short trains. These are listed in Table 1.2. Examples of data-simulation comparisons from this set are shown in Fig. 1.17, Fig. 1.18, and Fig. 1.19.

Table 1.2: Short train and witness data sets from 2007-2008 (Group *1a*).

Energy (Gev)	Species	Bunch currents	Train length	Witness length	Data sets
1.9, 2.1	Positrons	0.25, 0.5, 0.75, 1.0, 1.25, 3.0	3, 10, 11, 19, 20, 21	5-15	23
1.9, 2.1	Electrons	0.25 ,0.5, 0.75, 1.0, 1.25, 3.0	10, 11, 19, 20, 21	5-15	10
5.3	Positrons	0.75, 1.5, 5.0	3, 10	5-10	3
5.3	Electrons	1.5	10	10	1

2a. A series of data sets taken in 2009 with 45 bunch trains, with a range of bunch currents. Examples are shown in Fig. 1.20, Fig. 1.28 and Fig. 1.29.

3a. A series of data sets taken in 2010 to explore special lattice or beam conditions. Examples are shown Fig. 1.21. Studies of special lattice conditions are discussed below in Section 1.3.1.6.

[4]This supposition should be confirmed by simulations.

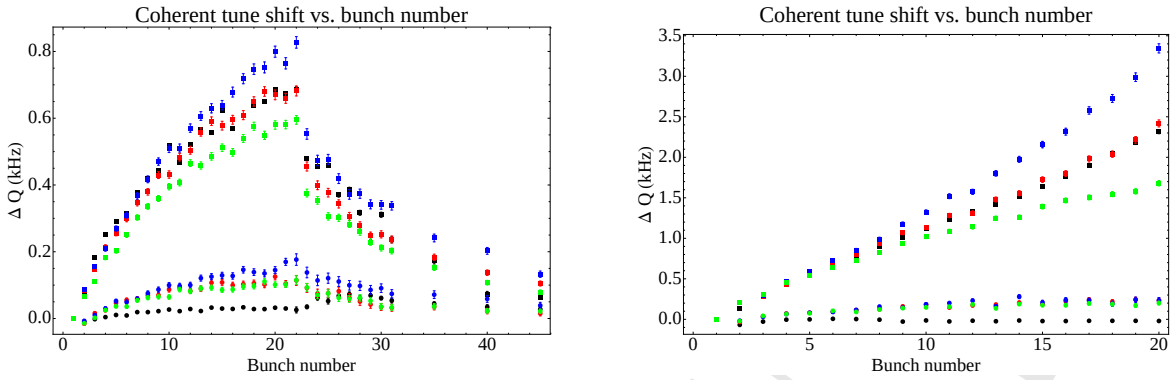

Figure 1.18: Coherent tune shifts, 2008 2.1 GeV data and `POSINST` simulations compared. Left: 21 bunch train with witnesses, 0.5 mA bunch current. Right: 20 bunch train, 1 mA bunch current. All for positrons with 14 ns spacing, and 2.1 GeV beam energy. Squares: Vertical tune shift. Disks: Horizontal tune shift. Black: data. Red: `POSINST` simulation using parameters given in Table 1.1. Blue: `POSINST` simulation with Table 1.1, except peak total secondary yield = 2.2. Green: `POSINST` simulation with Table 1.1, except peak total secondary yield = 1.8.

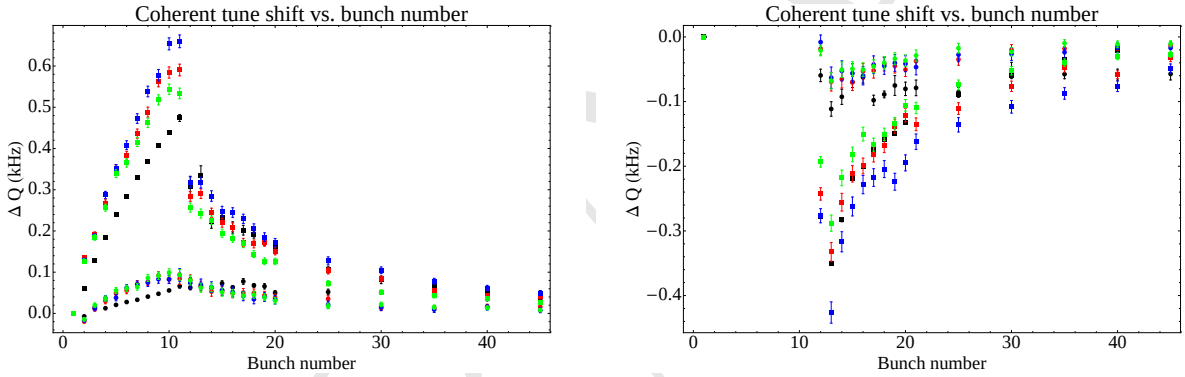

Figure 1.19: Coherent tune shifts, 2008 5.3 GeV data and `POSINST` simulations compared. Left: 10 bunch positron train with witnesses, 0.75 mA bunch current. Right: 10 bunch electron train, 1.5 mA bunch current, followed by witnesses, 0.5 mA bunch current; only the witness bunches are shown. All for 14 ns spacing, and 5.3 GeV beam energy. Squares: Vertical tune shift. Disks: Horizontal tune shift. Black: data. Red: `POSINST` simulation using parameters given in Table 1.1. Blue: `POSINST` simulation with Table 1.1, except peak total secondary yield = 2.2. Green: `POSINST` simulation with Table 1.1, except peak total secondary yield = 1.8.

Inspection of the data and simulation comparisons for the type *a* groups shows that the reference parameter set given in Table 1.1 does a fairly good job of representing the data, with the following exceptions:

- Generally, the horizontal simulated tune shifts, while small, are still larger than the data.
- The vertical tune shifts at 5.3 GeV are overestimated.
- The high bunch current (2 mA) witness bunch vertical tune shifts at 4 GeV may be underestimated.

The first two exceptions are discussed further in Section 1.3.1.7 below.

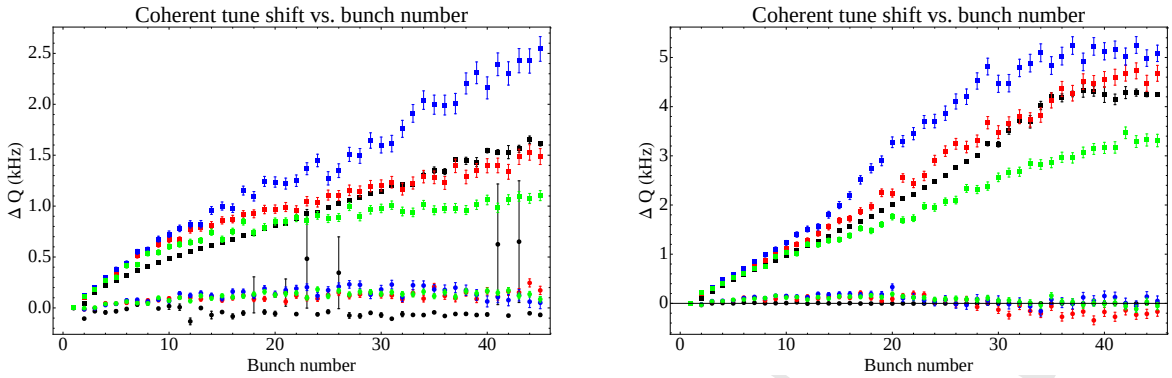

Figure 1.20: Coherent tune shifts, 2009 2.1 GeV data and POSINST simulations compared. Left: 45 bunch train, 0.6 mA bunch current. Right: 45 bunch train, 1 mA bunch current. All for positrons with 14 ns spacing, and 2.1 GeV beam energy. Squares: Vertical tune shift. Disks: Horizontal tune shift. Black: data. Red: POSINST simulation using parameters given in Table 1.1. Blue: POSINST simulation with Table 1.1, except peak total secondary yield = 2.2. Green: POSINST simulation with Table 1.1, except peak total secondary yield = 1.8.

type *b*: Tune measurements with a single bunch drive excitation with 1-2 mm amplitude. An example is shown in Fig. 1.22. Since there is no coherent oscillation of the entire train, the horizontal tune shifts are not suppressed. It is evident that the simulations overestimate the data, for the bunches near the end of the train. This disagreement may be related to the fact that the simulations were done using the "Modified static cloud model", which may not be a good approximation for this data type. More measurements of this type, in which both the mode of oscillation of the bunches and the oscillation amplitude are well-specified, are planned in the future.

type *c*: Tune measurements taken using the Dimtel feedback system. An example is shown in Fig. 1.23 and described in Ref. [28]. This is one of the few data sets taken to date with a bunch spacing of 4 ns. This data set, for which the horizontal tune shifts are quite large, clearly favors a higher value of the total peak secondary yield parameter than the reference parameter set. More data sets with this spacing are planned for future experiments.

type *d*: Tune measurements without a drive excitation, obtained from the analysis of BPM frequency spectra taken in conjunction with instability measurements, as discussed in Section 1.1.3. Examples are shown in Fig. 1.40 in the next section.

1.3.1.4 Systematic Study of Electron Cloud Model Parameters from POSINST simulations

To gain confidence in the ability of the POSINST simulation to predict the performance of future storage rings and to tune the POSINST parameters, a systematic effort was made to compare the simulations with measurements under a wide variety of conditions. Comparisons of measurements with simulations were made for 54 data runs with electron and positron beams at 1.9, 2.1, 4.0, and 5.3 GeV energy, in trains of 3 to 45 bunches, with bunch charges of 0.5 to 4.2 nC, representing the data in groups *1a* (2007-2008) and *2a* (2009).

For each data set, all six of the critical parameters shown in Table 1.1 were varied $\approx \pm 10\%$ relative to

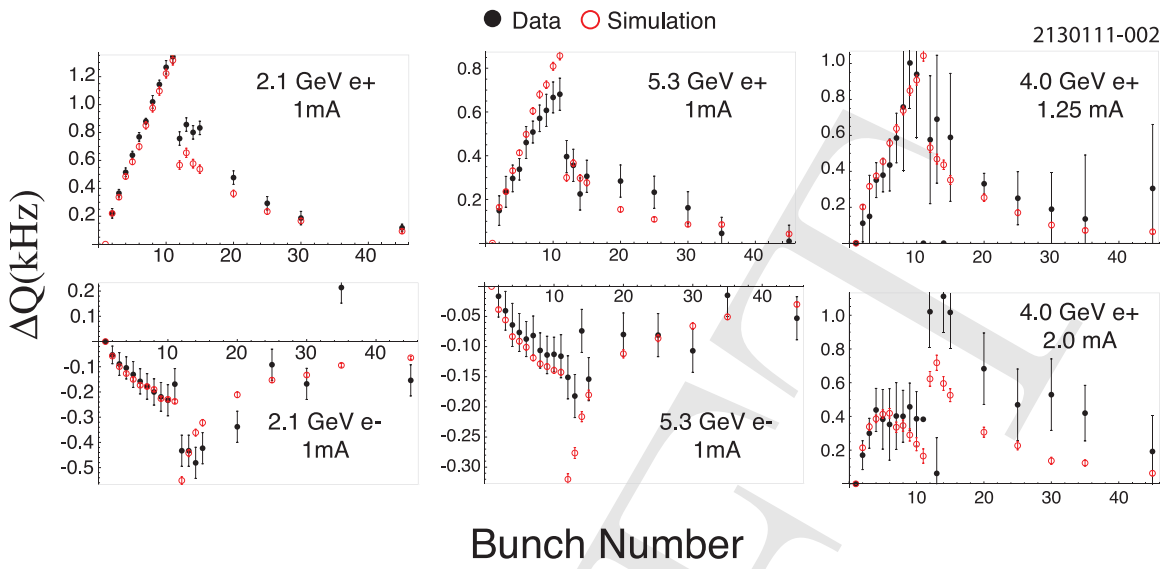

Figure 1.21: Vertical coherent tune shifts, 2010 data and `POSINST` simulations compared, using the parameters in Table 1.1.

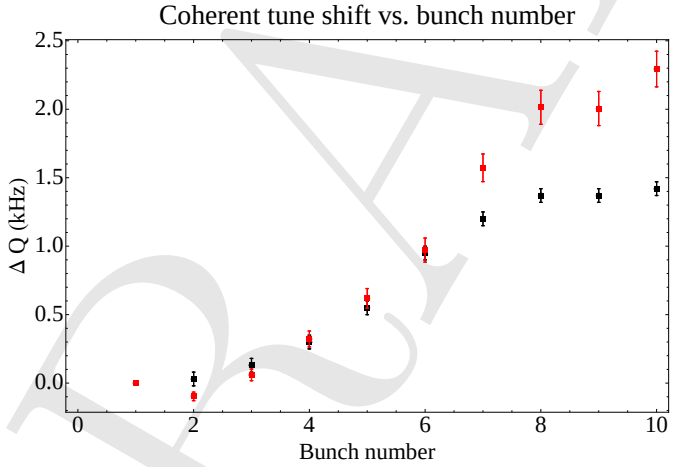

Figure 1.22: Horizontal coherent tune shifts, single-bunch-excitation data (black) and `POSINST` simulations (red) ("Modified static cloud model") compared. 10 bunch train, 4 mA bunch current, 2.1 GeV beam energy. `POSINST` simulation using parameters given in Table 1.1.

the reference parameter set. This was done independently for the horizontal and vertical tune shifts, and for the train and witness bunches, in order to monitor the consistency of the values obtained. A χ^2 was computed from the differences between the data and simulations, and a parabola was fit to the three χ^2 values to determine a best parameter value for each of the data sets.

Fig. 1.24 (left) shows the resulting values for the determination of the total secondary emission yield (SEY), for each data type, for the group *1a* and group *2a* data sets. Within the errors, the best-fit values for the total SEY parameter determined from the various data sets and data types are approximately the same.

It became quite clear during the evaluation process that the six `POSINST` parameters are not or-

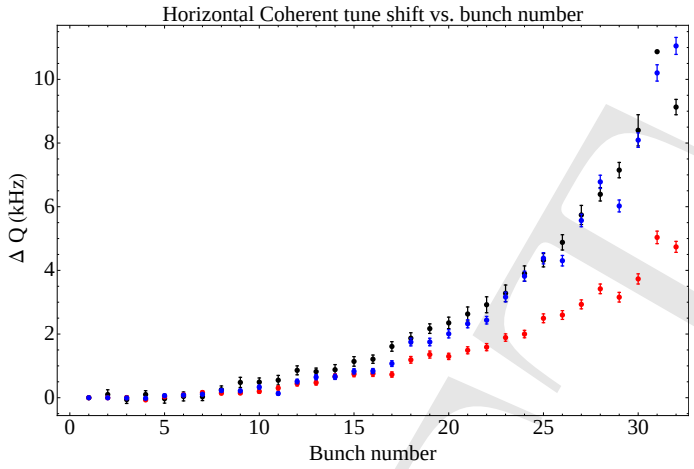

Figure 1.23: Horizontal coherent tune shifts, Dimel data (black) and POSINST simulations (red, blue) ("Modified static cloud model") compared. 32 bunch train, 0.8 mA bunch current, 2.1 GeV beam energy, 4 ns bunch spacing. Red: POSINST simulation using parameters given in Table 1.1. Blue: same simulation parameters except total peak secondary yield = 2.3

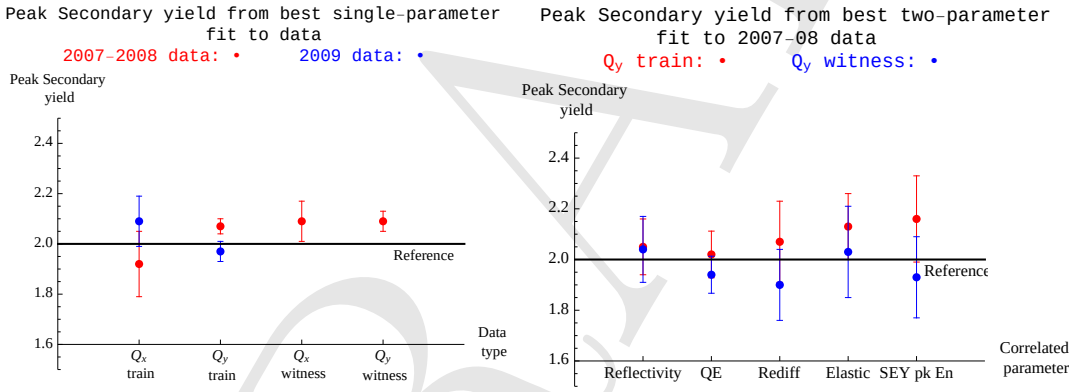

Figure 1.24: The best fit peak secondary emission yield parameter, as determined from a single-parameter fit, vs. data type (left); The best fit peak secondary emission yield parameter, as determined from a two-parameter fit, vs. the other parameter in the fit (right).

thogonal. To try to assess the correlations, we examined the secondary emission yield paired with each of the other five parameters. The fit χ^2 was evaluated at nine points for each pair, $\pm 10\%$ and zero offset from the reference value, and a two-dimensional parabolic fit was attempted at each data set. Often there was either no minimum, or a false minimum at a physically absurd value was found. In general, fits for the horizontal tunes failed, possibly because the POSINST model is inadequate, as noted above.

The results of this procedure are shown in Fig. 1.24 (right). Here we display the best-fit total SEY parameter obtained from a two-parameter fit, as a function of the other parameter, for the vertical tune data types. Although the results are consistent, the error bars are larger than for the single-parameter fits, reflecting the additional uncertainty caused by correlations between the total SEY parameter and the other parameters.

In Fig. 1.25, Fig. 1.26, and Fig. 1.27, we show the results of varying the other five critical parameters

about the reference values given in Table 1.1. The plots show the best fit values obtained from single-parameter fits using the group *1a* and group *2a* data sets separately, and the best-fit values obtained from the two-parameter fits, in which the other parameter was the peak SEY. Table 1.3 summarizes numerically the values that could be extracted from the fits that succeeded, and gives the correlations extracted from the two-parameter fits.

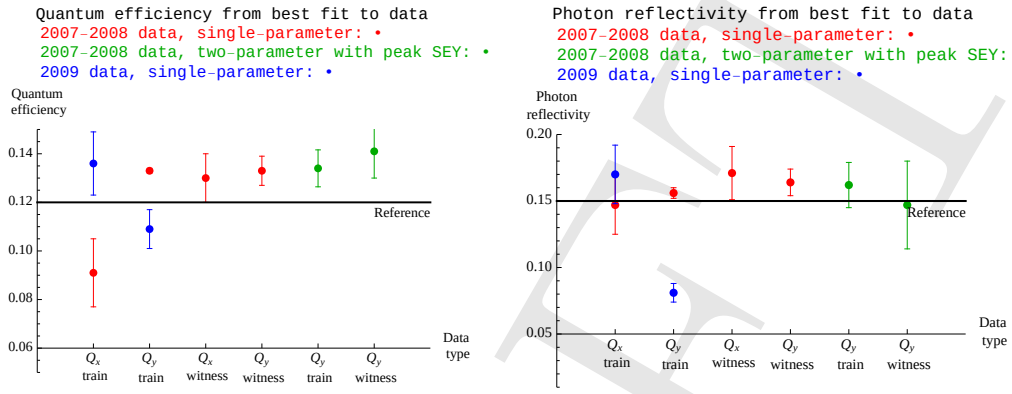

Figure 1.25: The best fit quantum efficiency parameter (left) and photon reflectivity (right), as determined from single-parameter fits and two-parameter fits with the total SEY, vs. data type. While some of the single-parameter fit results appear inconsistent, the error bars obtained from the two-parameter fits are the best estimate of the true uncertainties.

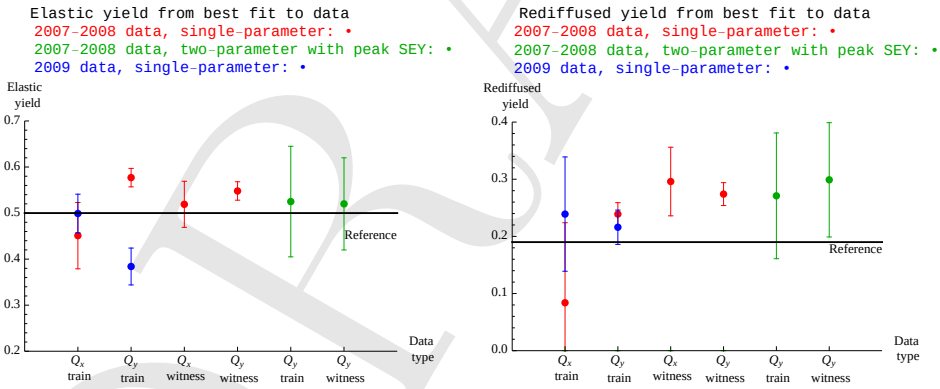

Figure 1.26: The best fit elastic SEY parameter (left) and rediffused SEY parameter (right), as determined from single-parameter fits and two-parameter fits with the total SEY, vs. data type. While some of the single-parameter fit results appear inconsistent, the error bars obtained from the two-parameter fits are the best estimate of the true uncertainties.

It is clear that the effort of fitting has not yielded a dramatic improvement in the determination of the `POSINST` parameters. In an effort to improve this technique we are using more sophisticated statistical techniques to help weed out poor measurements, which lead to misleading values of χ^2. Additional data have been taken at different bunch spacings in the hopes of better distinguishing primary from secondary electron emission.

Finally, we expect that the simulation improvements noted in Section 1.3.1.7 may resolve some of the issues.

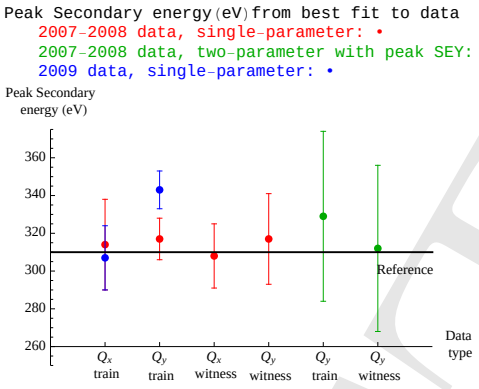

Figure 1.27: The best fit SEY peak energy parameter as determined from single-parameter fits and two-parameter fits with the total SEY, vs. data type.

1.3.1.5 Comparisons between data and ECLOUD simulations

Comparisons between CesrTA tune shift data and ECLOUD simulations have been previously reported in Refs. [21] and [20]. An example is shown in Figure 1.28, which corresponds to measurements from group *2a* for 45 positron bunches at a beam energy of 2.1 GeV with 14-ns spacing and a bunch current of 0.4 mA. The magnitude and time dependence of the vertical tune shifts are well described by the ECLOUD and POSINST simulations.

The relative contributions of the field-free and dipole regions of the ring to the vertical tune shift depend strongly on the bunch population, as can be seen by comparing Fig. 1.28 with Fig. 1.29, where the measurements were taken under identical conditions, but for a bunch population of 0.8 mA. Here the dipole contribution dominates after about 15 bunches in the train, resulting in the characteristic linear rise of the vertical tune shift. The beam kicks on the cloud electrons are strong enough for this bunch population that the secondary yield on the top and bottom of the vacuum chamber in the vertical plane containing the beam now dominate the vertical space-charge field gradients.

These measurement conditions are very similar to those described in Ref. [21]. However, the discrepancy (see Fig. 3 in [21]) between the data and the ECLOUD simulations reported in [21] has been resolved. Numerical approximations in the ECLOUD calculation have been improved, and, more importantly, the re-diffused component in the secondary yield model has been introduced. The re-diffused secondaries carry a substantial fraction of the kinetic energy of the incident cloud electrons [7]. If this contribution from re-diffused cloud electrons is omitted, the simulated dipole contribution to the vertical tune shift reaches a level about half of the measured tune shift of the 45th bunch. Figure 1.30 illustrates the effect of the re-diffused component, distinguishing the contributions to the vertical tune shift from the drift and dipole regions. The dipole contribution at the higher bunch current is responsible for the continuing increase of the vertical tune shift along the bunch train, and the slope of the increase is largely due to the re-diffused secondary yield component. We also verified that the POSINST model shows a discrepancy with the measurement similar to that of ECLOUD when its re-diffused secondary yield component is removed.

Table 1.3: Evaluating `POSINST` parameters. The reference SEY peak value is 2.0. Reference values for the other parameters are in the first column, and their best-fit values using train and witness tune shifts are in the next two columns.

Ref	Q_yTrain	Q_yWitness
	SEY peak $= 2.05 \pm 0.11$	SEY peak $= 2.04 \pm 0.13$
0.15	Reflectivity $= 0.162 \pm 0.017$	Reflectivity $= 0.147 \pm 0.033$
	Correlation $= -0.83 \pm 0.12$	Correlation $= -0.89 \pm 0.08$
	SEY peak $= 2.02 \pm 0.09$	SEY peak $= 1.94 \pm 0.07$
0.12	Quantum Efficiency $= 0.134 \pm 0.008$	Quantum Efficiency $= 0.141 \pm 0.011$
	Correlation $= -0.83 \pm 0.08$	Correlation $= -0.74 \pm 0.21$
	SEY peak $= 2.07 \pm 0.16$	SEY peak $= 1.90 \pm 0.14$
0.19	Rediffused at infinity $= 0.27 \pm 0.11$	rediffused at infinity $= 0.30 \pm 0.10$
	Correlation $= -0.84 \pm 0.12$	Correlation $= -0.89 \pm 0.04$
	SEY peak $= 2.02 \pm 0.09$	SEY peak $= 1.94 \pm 0.07$
0.50	Elastic SEY peak $= 0.53 \pm 0.12$	Elastic SEY peak $= 0.52 \pm 0.10$
	Correlation $= -0.72 \pm 0.21$	Correlation $= -0.89 \pm 0.10$
	SEY peak $= 2.02 \pm 0.09$	SEY peak $= 1.94 \pm 0.07$
310	True Secondary Peak Energy $= 329 \pm 45$	True Secondary Peak Energy $= 312 \pm 44$
	Correlation $= 0.5 \pm 0.4$	Correlation $= 0.48 \pm 0.23$

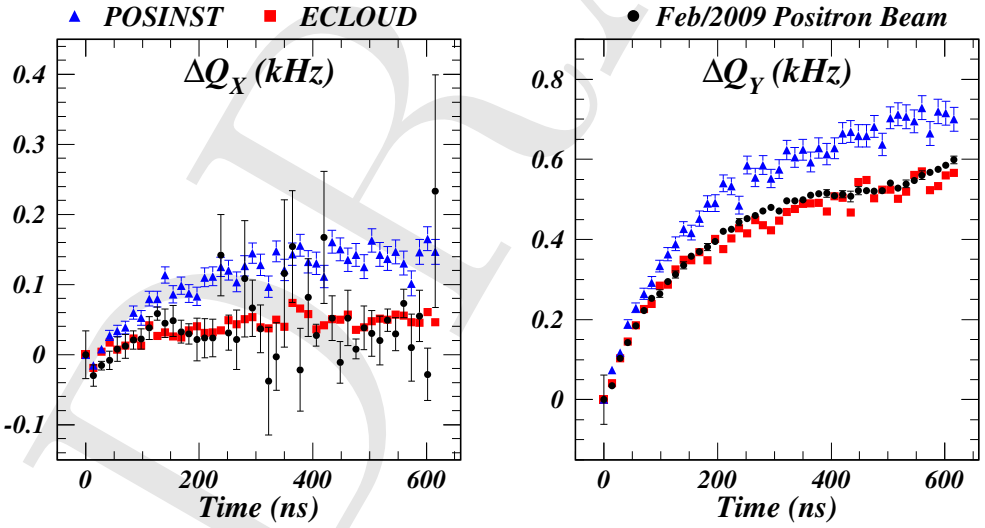

Figure 1.28: Comparison of the measured and simulated horizontal and vertical tune shifts along a 45-bunch train of 2.1 GeV positrons spaced by 14 ns. The bunch current is 0.4 mA. `POSINST` simulations using parameters given in Table 1.1. The `ECLOUD` and `POSINST` simulations show that, for this bunch current, the contribution to the vertical tune shift from the the dipole regions is only about 40% of the total tune shift, even though the ratio of dipole region length to drift region length is about 3:1.

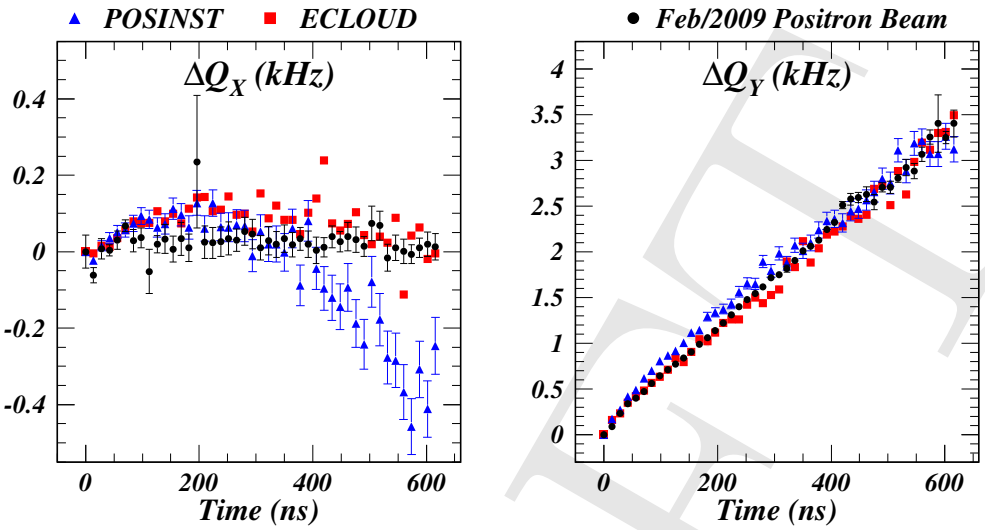

Figure 1.29: Measured and simulated tune shifts under the same conditions as for Fig. 1.28, but with double the bunch population. Under these conditions, the beam kicks are strong enough that the cloud buildup is dominated by the secondary yield on the top and bottom of the dipole vacuum chambers in the vertical plane containing the beam.

1.3.1.6 Study of the effects of solenoids in the CesrTA drifts

The tune shifts observed in CesrTA are due to electron cloud present in both the drift regions of the ring (about 179 m) and the dipole regions (about 475 m). Attempts have been made to separate the tune effects in the dipoles as opposed to the drift regions by introducing a 40-Gauss solenoidal field in the most of the drift regions. By keeping photoelectrons accelerated by the beam from hitting the walls, the effects of secondary emission should be reduced in the regions with solenoids. Data sets (group *3a*) comparing solenoids on and off are shown in Fig. 1.31. Data are shown for 2.1 GeV positrons (top left) and electrons (bottom left) and 5.3 GeV positrons (top right) and electrons (bottom right). The solid curve is the `POSINST` simulation including both dipoles and drifts, and the dotted curve includes only dipoles. The reference simulation parameters, shown in Table 1.1, were used for the simulations.

It is clear from Fig. 1.31 that the `POSINST` simulations underestimate the solenoid-on tune shifts, particularly for the case of 2.1 GeV positrons. Additional simulation work is needed here to understand this.

1.3.1.7 Improvements to electron cloud modeling for tune shifts at CesrTA

Use of the photon transport code `SYNRAD3D` The simulations described above use the photon intensities corresponding to the synchrotron-radiated photons striking the vacuum chamber in the bend plane, together with a single empirically determined "Photon reflectivity" parameter to describe the reflected photons. However, since the source of the synchrotron radiation is well known, and the reflection of the radiation from the walls can be modeled, it is possible to make reliable estimates of both the in-bend-plane and scattered radiation. These estimates allow a

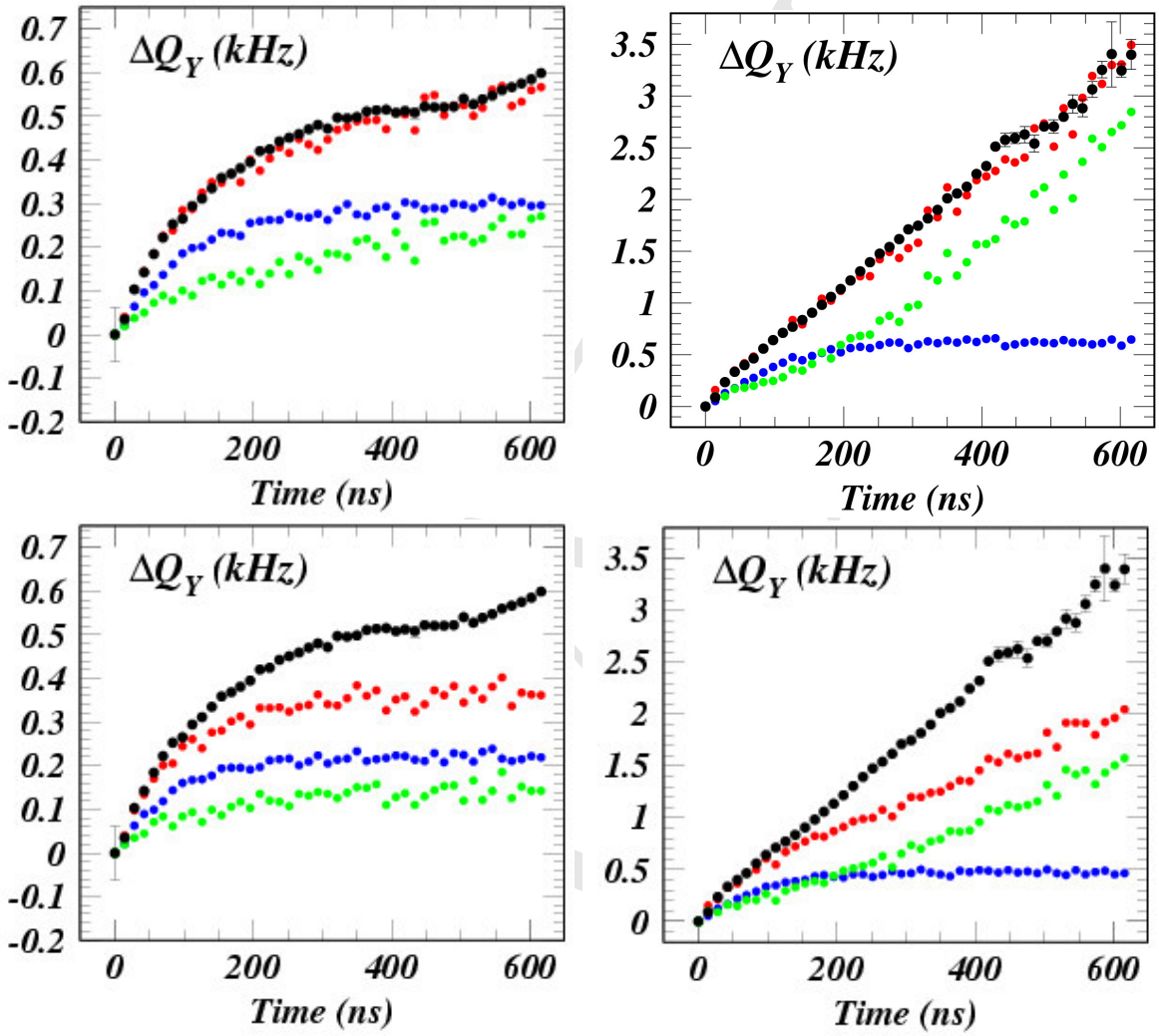

Figure 1.30: Measured and simulated vertical tune shifts under the same conditions as for Figs. 1.28 and 1.29, showing the effect of the re-diffused SEY component on the contributions from the drift and dipole regions. The green points show the dipole contribution, the blue points show the drift contribution, and the red points show their sum. The measurements are shown as black points. The left (right) column shows the results for a bunch current of 0.4 mA (0.8 mA). The re-diffused secondary yield was set to 0.19 (0.00) while maintaining the peak secondary yield at 2.0 to obtain the results in the upper (lower) row.

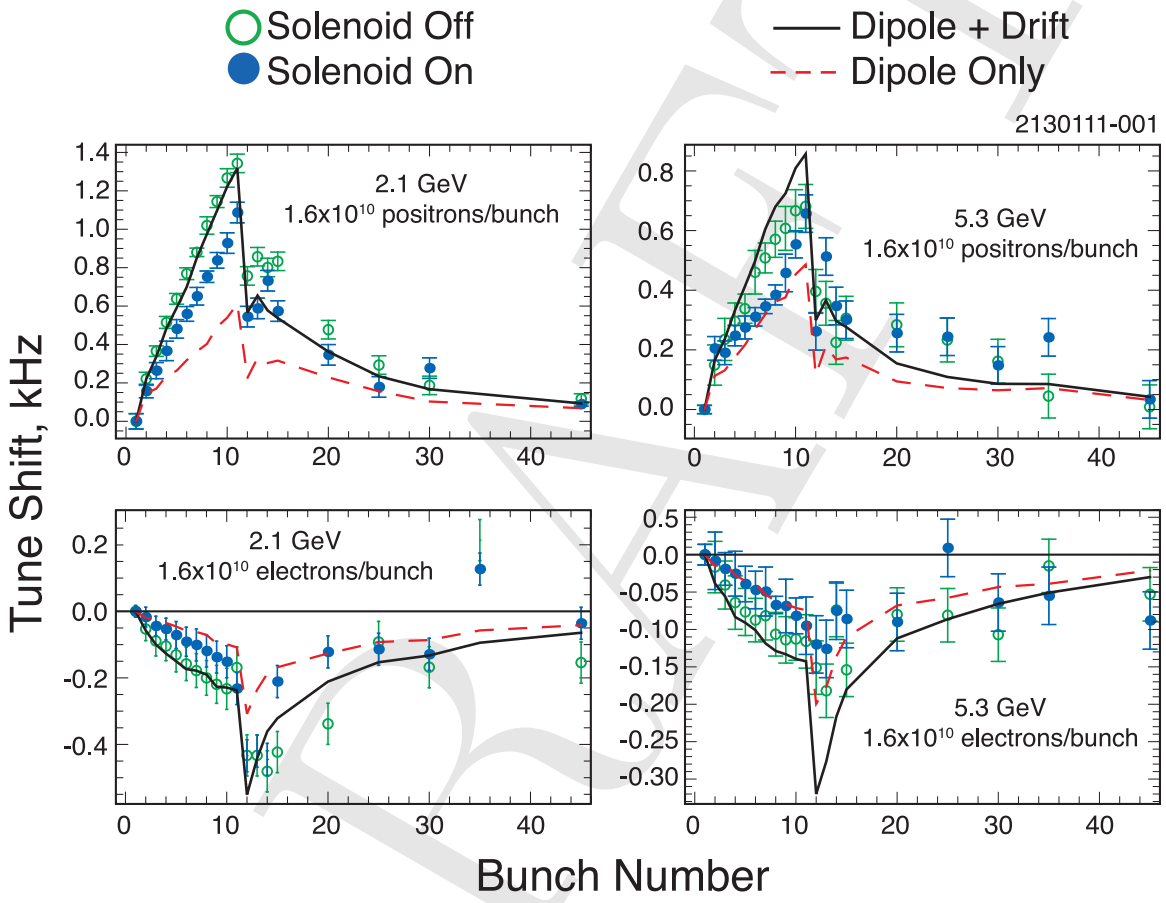

Figure 1.31: Dependence of vertical tune shifts on solenoids in drift regions. Positron (top) and electron (bottom) tune shifts vs. bunch number, for 2.1 (left) and 5.3 GeV (right) beams. The green circles and blue dots represent data taken with solenoids off and on, respectively. The solid curve is the `POSINST` simulation including both dipoles and drifts, and the dotted curve includes only dipoles, using the parameters in Table 1.1.

full characterization of the radiation absorbed on the walls to be made, without the need for an empirically determined reflectivity parameter. Since the radiation characterization can be made for any beam energy, ring lattice, and vacuum chamber profile, this greatly facilitates the extrapolation of electron cloud buildup calculations to future positron rings.

As described in Section **??**, we have developed a three-dimensional photon production, transport and scattering simulation code, `SYNRAD3D`, which can predict the distribution of photon absorption sites on the vacuum chamber wall at any longitudinal position. The predictions from `SYNRAD3D` can be read into `POSINST` or `ECLOUD` to provide a fully characterized description of the incident radiation. The description is limited by the accuracy of the vacuum chamber model, and by the approximations used in the scattering model. To date, the radiation calculations have been done with a simple, longitudinally uniform, vacuum chamber model, and with a scattering model based on purely specular reflection from an aluminum surface. However, the code has the capability to model complex vacuum chamber shapes and to include diffuse scattering.

In Fig. 1.32 and Fig. 1.33, we compare (a) the tune shifts calculated using the `SYNRAD` photon intensities for the bend plane radiation, together with an empirical reflectivity parameter describing a uniform distribution over the rest of the chamber, with (b) a calculation based on the `SYNRAD3D` photon distributions. Both calculations use the reference simulation parameters presented in Table 1.1 for the SEY model parameters. For the results derived from the `SYNRAD3D` photon distributions, we have used lower values for the empirical quantum efficiency (10.8% for dipoles, 9.7% for drifts) to optimize agreement with the vertical tune shifts for the 2.1 GeV data, and, in addition, a more realistic Lorentzian photoelectron energy distribution (see next subsection).

Examination of Fig. 1.32 shows a significant improvement in the agreement between the horizontal tune shift data and the simulations, when using the `SYNRAD3D` photon distributions. Most of this improvement results from the use of a highly nonuniform photon distribution on the vacuum chamber out of the bend plane (see, for example, Fig. **??**), as predicted by `SYNRAD3D`, in contrast to the simpler uniform distribution used in simulations based on `SYNRAD`.

Fig. 1.33 also shows an improvement in the agreement between the vertical tune shift data and the simulations. Although a discrepancy remains, we note that the quantum efficiency should be different (and lower) at 5.3 GeV than at 2.1 GeV, since the photon spectrum at 5.3 GeV is harder, and the quantum efficiency decreases at higher photon energies. Using the methodology outlined in Section **??** above, and the photon energy spectra from `SYNRAD3D` simulations, the relative reduction in quantum efficiency from 2.1 GeV to 5.3 GeV should be about 20%.

It should be noted that these `SYNRAD3D` simulations were done with a uniform elliptical vacuum chamber throughout the ring, rather than the actual CesrTA vacuum chamber, and did not include any diffuse scattering or X-ray fluorescence effects. Each of these three enhancements may make a significant difference in the results, so the current simulations, despite the improved agreement with the data, must be regarded as rather preliminary.

Photoelectron modeling (see also Section ??) In connection with studies of electron cloud effects for the LHC, direct measurements [29] have been made of the photoelectron energy spectrum produced by soft VUV photons. The measurements indicate that the photoelectron energy spectrum can be well represented by a Lorentzian with a peak and width of a few eV. Studies of the shielded button data (see Section **??**) demonstrate that, although a simple Lorentzian distribution is adequate for the photons generated by a 2 GeV CesrTA beam, for the harder photon

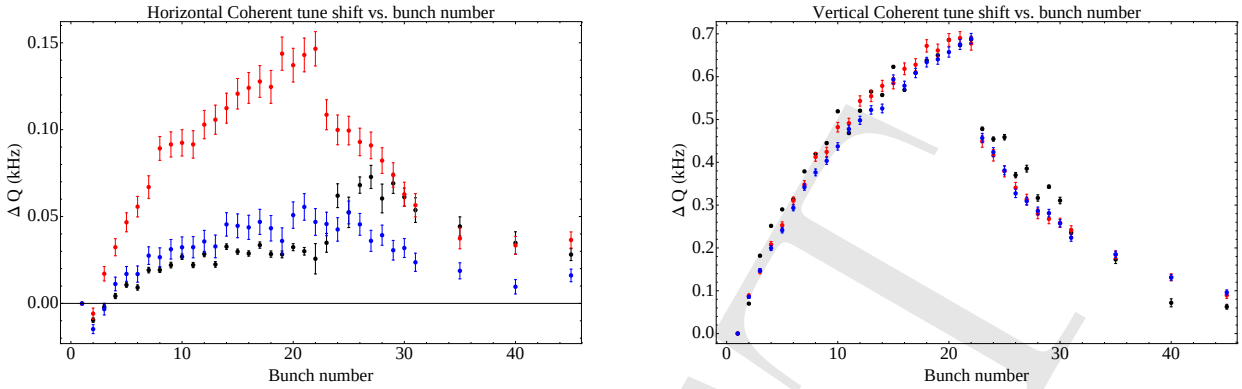

Figure 1.32: Tune shifts vs. bunch number, for 2.1 GeV data set corresponding to Fig. 1.18, left, computed (using `POSINST`) from `SYNRAD` (red points) and `SYNRAD3D` (blue) photon simulations, compared with data (black).

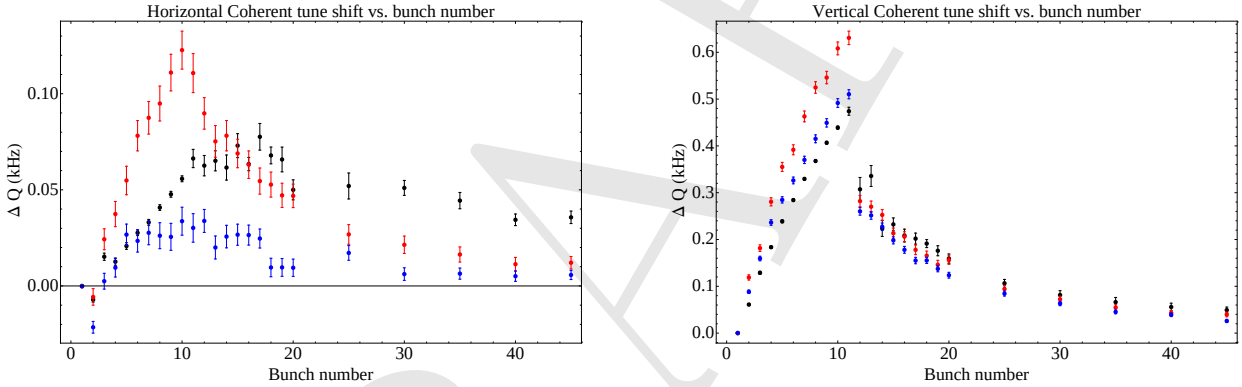

Figure 1.33: Tune shifts vs. bunch number, for 5.3 GeV data set corresponding to Fig. 1.19, left, computed (using `POSINST`) from `SYNRAD` (red points) and `SYNRAD3D` (blue) photon simulations, compared with data (black).

spectrum generated by a 5 GeV beam, a high energy tail, with a power law falloff slower than that of a Lorentzian, is required. Consequently, a new parameterization, using a Lorentzian spliced to a power law distribution with an adjustable exponent at high photoelectron energies, has been installed in `POSINST`. Preliminary re-evaluation of the tune shift simulations for both positron and electron beams at 5 GeV indicate that the presence of a high energy tail in the photoelectron energy spectrum makes only small differences in the simulated tune shifts.

1.3.1.8 Future work

Measurements at bunch spacings of 4 ns and 8 ns, similar to the proposed ILC damping ring bunch spacing of 6 ns are planned.

1.3.2 Instability Thresholds: Experimental Studies

1.3.2.1 Overview

Introduction To continue our studies of electron cloud related phenomena, we have developed the capability to make automated measurements of frequency spectra of individual bunches, to look for signals for single-bunch instabilities.

In this measurement, a button BPM at 33W (sensitive to both vertical and horizontal motion) is gated on a single bunch, and the signal is routed to a spectrum analyzer. Several frequency spectra are acquired, covering a range which spans the lowest betatron sidebands. Machine conditions, such as bunch current, magnet settings, feedback system parameters, etc. are automatically recorded and stored before and after each single-bunch spectrum is taken.

Using this system, during the recent July-August, 2010, and September runs, a number of observations were made which illuminate the dynamics of the electron-cloud/beam interaction at CesrTA. This paper will review results from these experiments.

General remarks All experiments discussed here were done at 2.085 GeV in a low emittance lattice. The machine parameters for these experiments are shown in Table 1.4.

Table 1.4: Nominal machine parameters at 2 GeV. The emittances and tunes are those of a single bunch in the machine.

Parameter	Unit	Value
Energy	GeV	2.085
Lattice		2085mev_20090516
Horizontal emittance	nm	2.6
Vertical emittance	pm	~ 20
Bunch length	mm	10.8
Horizontal tune		14.55
Vertical tune		9.58
Synchrotron tune		0.065
Momentum compaction		6.8×10^{-3}
Revolution frequency	kHz	390.13

Trains having bunches numbering from 30-45, with a bunch spacing of 14 ns, and bunch currents in the range of $0.5 - 1.25$ mA ($0.8 - 2.0 \times 10^{10}$ particles) per bunch were studied. In all cases, except where specifically noted, the beam particles were positrons.

Several systematic checks were undertaken:

- Checks were made to rule out intermodulation distortion in the BPM electronics and in the BPM itself.
- The betatron and synchrobetatron (head-tail) lines moved as expected when the vertical, horizontal, and synchrotron tunes were varied.

The longitudinal feedback was off for these measurements. The vertical and horizontal feedback were turned down to 20% of full power. Some experiments explored the effect of turning the vertical

feedback fully off.

More details on the experimental technique can be found in Section 1.1.3.

General observations The basic observation is that, under a variety of conditions, the frequency spectra exhibit the vertical $m = \pm 1$ synchrobetatron (head-tail) lines, separated from the vertical betatron line by the synchrotron frequency, for many of the bunches along the train. The amplitude of these lines typically (but not always) grows along the train.

Typically, for the bunch at which the vertical synchrobetatron lines first appear above the noise floor (which is about 40 dB below the vertical betatron line), we observe (on a bunch-by-bunch X-ray beam size monitor) growth in the beam size, which continues to increase along the train (see Section 1.3.4).

Under some conditions, the first bunch in the train also exhibits a synchrobetatron line ($m = -1$ only). The presence of a "precursor" bunch, placed about 180 ns before the train, eliminates the $m = -1$ signal in the first bunch.

Subsequent sections will present the details of these observations, together with their dependence on machine and beam parameters such as bunch current, number of bunches, chromaticity, synchrotron tune, beam emittance, vertical feedback, beam energy, and particle species. In the final section, some preliminary observations on measurements of bunch-by-bunch damping rates are presented.

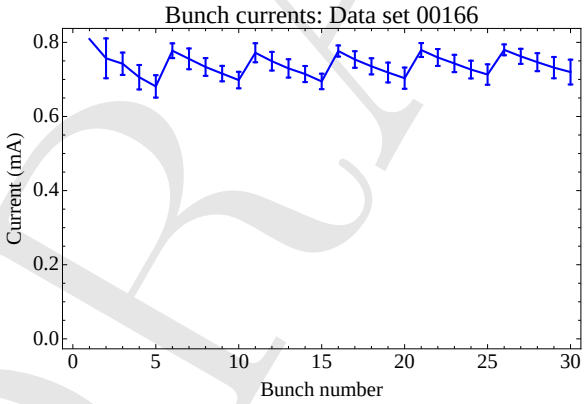

Figure 1.34: Data set 166: Bunch-by-bunch currents

1.3.2.2 Bunch-by-bunch power spectrum

To measure a bunch-by-bunch power spectrum, the machine is loaded with a bunch train with a uniform current per bunch, and software is run to automatically collect frequency spectra from a button BPM gated on the first bunch. The data acquisition takes a few minutes, and the gate is then moved to the second bunch, and so on through the train. The gate width is much smaller than the bunch spacing, so only the motion of the gated bunch is observed. The frequency spectra are 10 s averages, acquired in 4 measurements, each with a 40 kHz span, covering the range from 170 to 330 kHz.

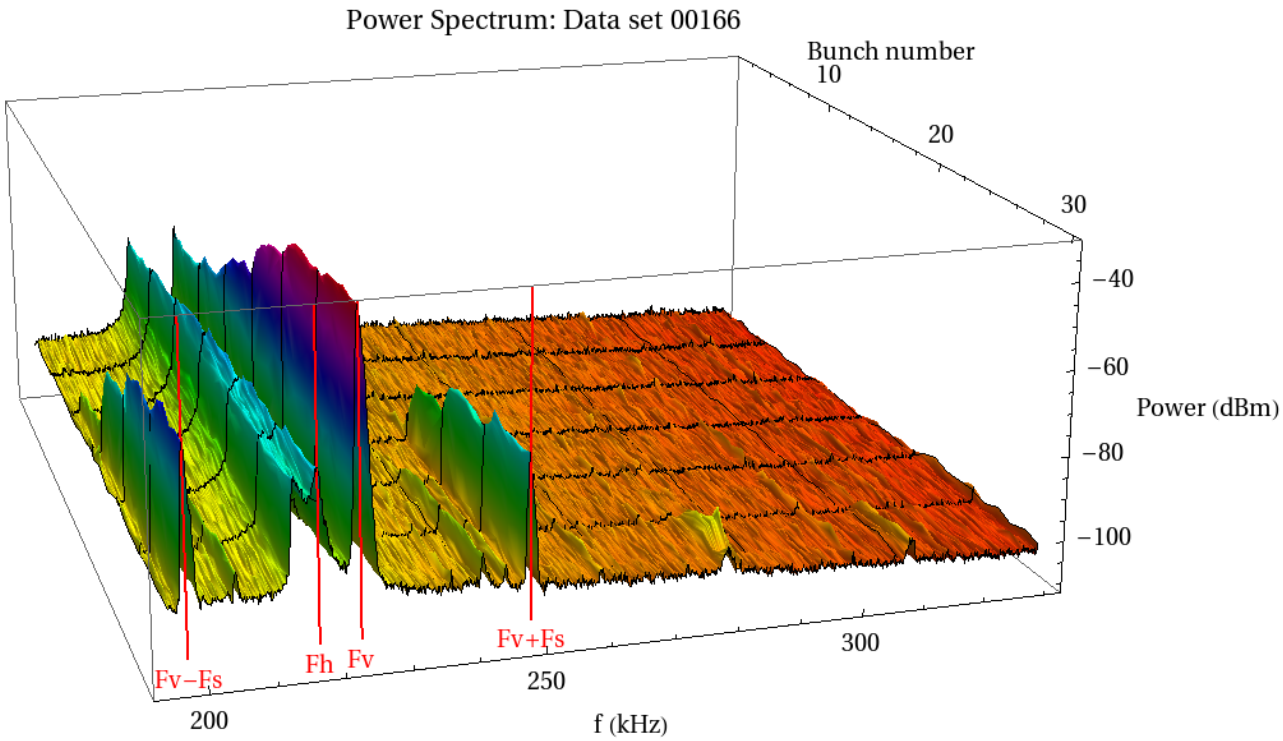

Figure 1.35: Data set 166: Bunch-by-bunch power spectrum

Since the beam has a relatively short lifetime, it is necessary to periodically pause the measurements and "top off" the bunch train. Typically, this is done after data acquisition is completed for a group of 5 bunches. Fig. 1.34 shows the beam current as a function of bunch number during a specific data set. In this figure, the current per bunch plotted for bunch n corresponds to the average value of the bunch current for all bunches earlier than bunch n; the error bar represents the rms variation in this number, principally due to irregularities in the fill. The dips at bunches 5, 10, ..., and peaks at 6, 11, ..., correspond to when the train is "topped off."

The bunch-by-bunch power spectrum observed in data set 166 is shown in Fig. 1.35. The figure plots the power spectrum for each bunch, as measured at the button BPM, vs. frequency. The four prominent peaks seen correspond, from lower to higher frequency, to the $m = -1$ vertical synchrobetatron line, the horizontal betatron line, the vertical betatron line, and the $m = +1$ vertical synchrobetatron line. Fig. 1.36 shows the spectrum of the last bunch, bunch 30, in greater detail. For this data set, the vertical chromaticity[5] was 1.16, and the horizontal chromaticity was 1.33.

The principal features exhibited in Fig. 1.34 and Fig. 1.35 are discussed in more detail in the next subsections.

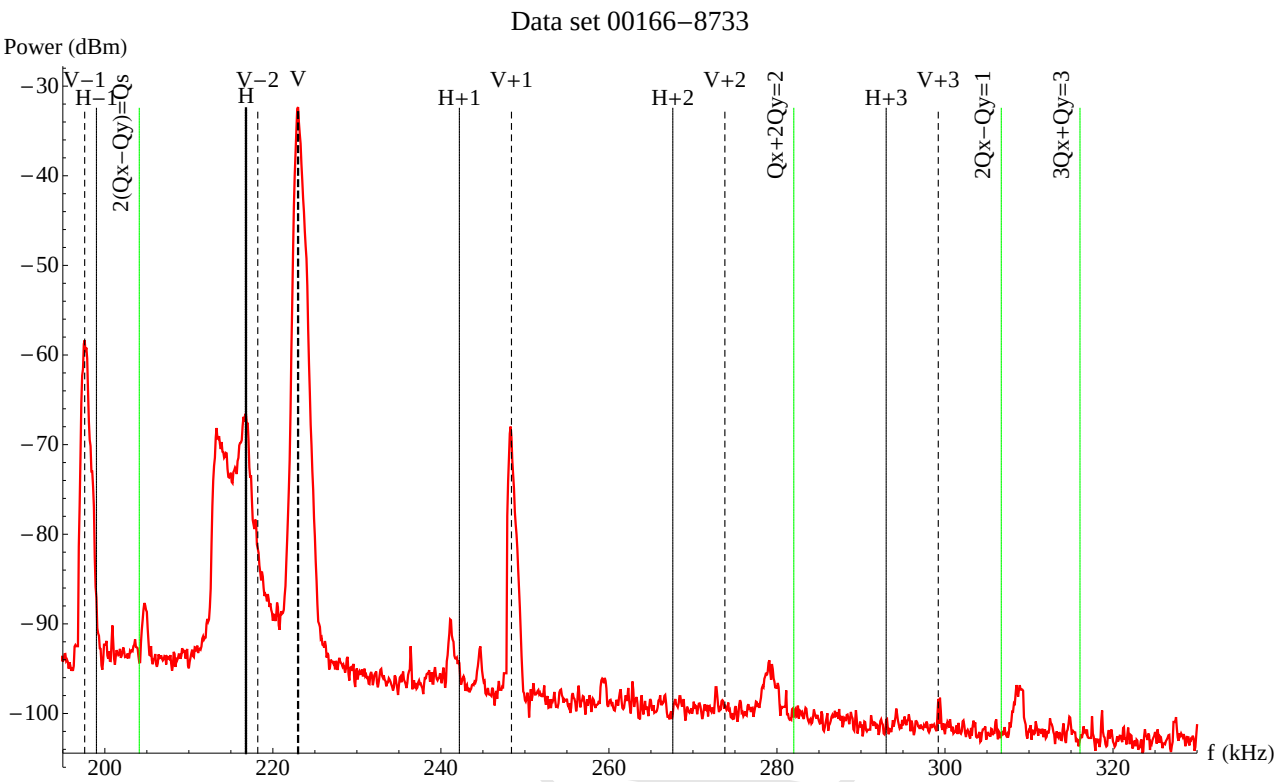

Figure 1.36: Data set 166: Power spectrum for bunch 30. The lines labelled, for example,"V+1" and "V-1" are shown at frequencies of $\pm f_s$ from the vertical betatron line ("V"), in which f_s is the synchrotron frequency. The locations of several machine resonances are also indicated.

1.3.2.3 Power spectrum features near the betatron lines

Horizontal betatron lineshape Fig. 1.37 shows the bunch-by-bunch power spectrum near the horizontal betatron line. There is a major peak which shifts up in frequency by about 4 kHz during the bunch train. This shift is attributable to the electron cloud. A quantitative comparison with simulations is presented below. In addition, there is a lower amplitude "shoulder", which appears to be roughly constant in frequency during the bunch train (i.e., there is no tune shift). A plausible explanation for this shoulder is the following: tune shift measurements and simulations (see Section 1.2.1.3) have shown that, when the all the bunches in the train are oscillating in-phase, the horizontal tune shift due to the electron cloud in a dipole-dominated ring such as CesrTA is very small. However, for the data set shown in Fig. 1.37, the bunches in the train are spontaneously excited, so a mixture of multibunch modes will be present. This mixture of multibunch modes will exhibit a spectrum of electron-cloud-induced tune shifts, ranging from nearly zero tune shift for the mode in which the bunches are oscillating in phase, to large tune shifts for modes in which bunches are oscillating with different phases. Qualitatively, this should produce a spectrum similar to that shown in Fig. 1.37.

[5]The chromaticity is defined as

$$\chi = \frac{dQ}{d\delta},$$

where δ is the relative momentum shift and Q is the tune.

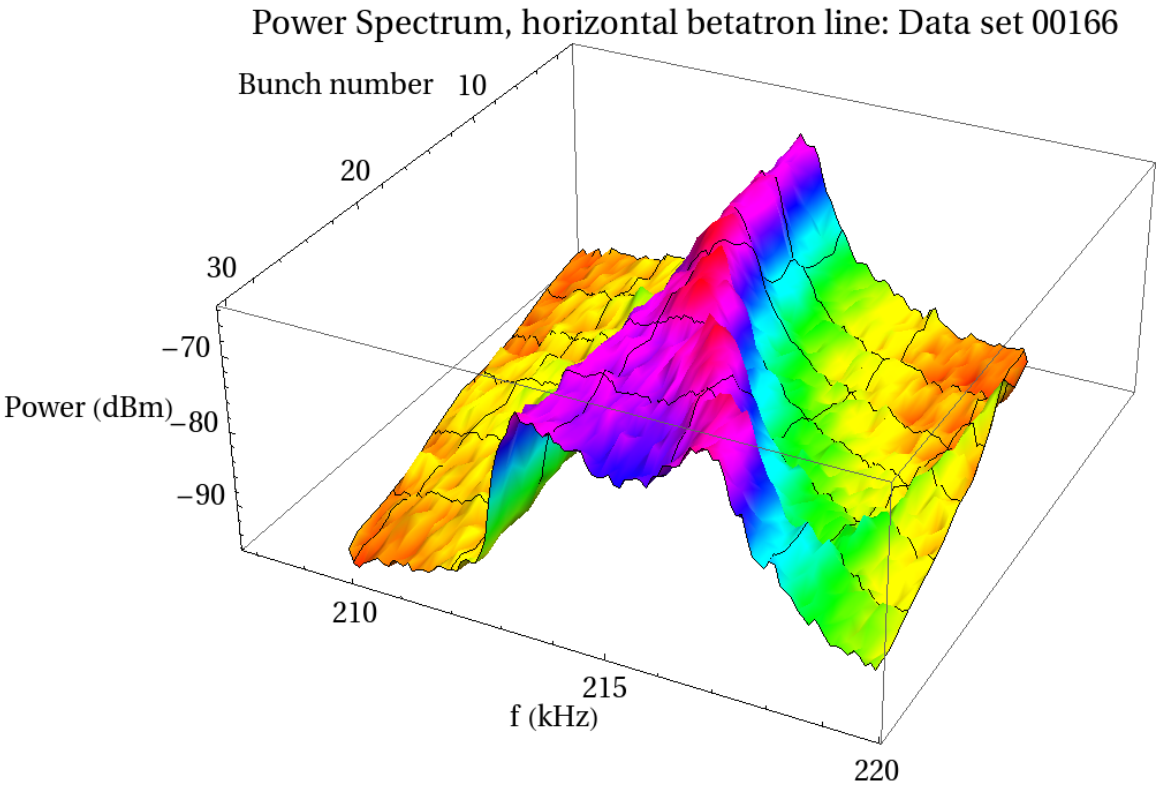

Figure 1.37: Data set 166: Bunch-by-bunch power spectrum: detail at horizontal betatron line. Chromaticity: (H,V) = (1.33, 1.16). Bunch current = 0.74 mA.

Vertical betatron lineshape Fig. 1.38 shows the bunch-by-bunch power spectrum near the vertical betatron line. In this case, there is a shift up in frequency of the major peak by about 2 kHz during the bunch train, which is again attributable to the electron cloud. In addition, there is a smaller peak at a higher frequency, present even on the first bunch, which appears to grow in amplitude and merge with the main peak near the end of the bunch train. Since this peak is present even for the first bunch, it is unlikely that it is due to a multibunch mode dependence of the vertical electron cloud tune shifts. Also, measurements and simulations (see Section 1.2.1) have shown that the dependence of the *vertical* tune shifts on the multibunch mode is much smaller than for the horizontal tune shifts. This suggests that the structure in the vertical plane may be a single-bunch effect, but we have no good explanation for it.

Horizontal and vertical betatron lines: peak power and frequency In Fig. 1.39, the peak power point[6] for each of the horizontal and vertical betatron lines is shown, as a function of

[6]For all the relative power plots shown in this paper, the plotted points were obtained as follows: A frequency region is selected, 10 kHz wide, centered approximately on the frequency of interest. The average background power level in this region is determined. Then, the maximum value of the power in this region is found, and subtracted from the background power level, to obtain the relative power.

Because of this background subtraction, if the relative power is close to zero (as in the plots of head-tail line power later in the paper), this signifies the absence of any significant peak.

The frequency plots correspond to the frequencies of the peak power points.

The errors shown in the frequency plots correspond to the bin widths of the frequency spectra (100 Hz). The errors shown in the relative power plots are estimated from the variation in the power over a spectral bin width.

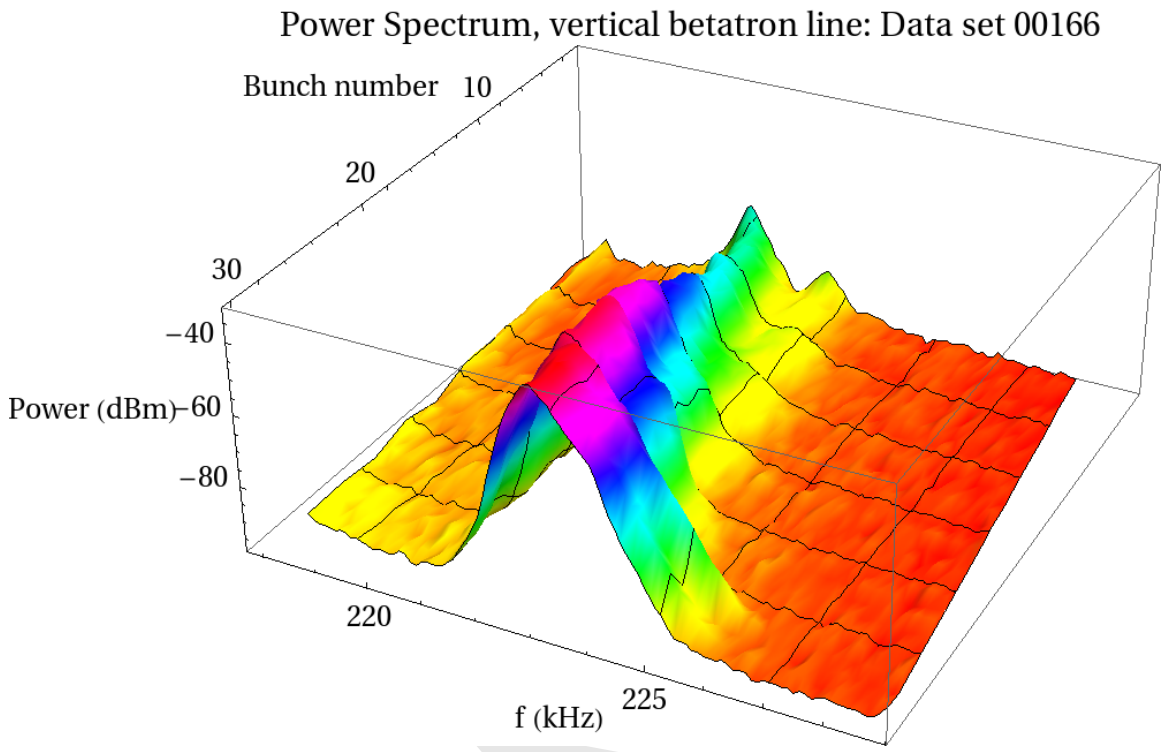

Figure 1.38: Data set 166: Bunch-by-bunch power spectrum: detail at vertical betatron line. Chromaticity: (H,V) = (1.33, 1.16). Bunch current = 0.74 mA.

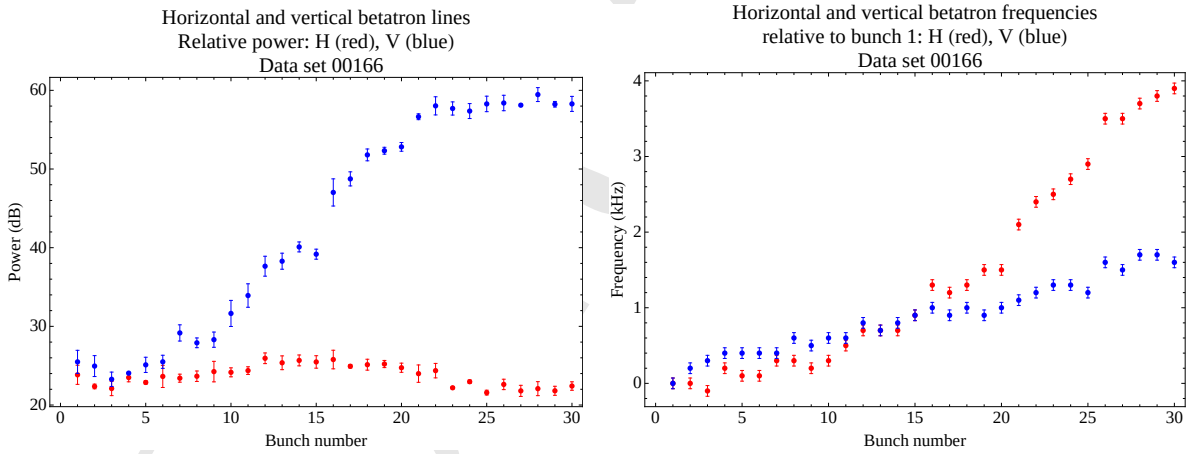

Figure 1.39: Data set 166: Left, Horizontal and vertical peak power vs. bunch number; right, Horizontal and vertical tune shifts vs. bunch number. Chromaticity: (H,V) = (1.33, 1.16). Bunch current = 0.74 mA.

bunch number. The strong excitation of vertical dipole motion is evident in the increase in vertical betatron line power along the train. There is minimal if any additional excitation in the horizontal plane.

In Fig. 1.39, the frequency of the peak power point is given, relative to the frequency of the first bunch. Thus, Fig. 1.39 illustrates the tune shift along the train, which is primarily due to the

electron cloud effect.

Comparison with electron cloud buildup simulations The cloud buildup program `POSINST` can be used to compute the cloud density corresponding to a set of beam and vacuum chamber properties at CesrTA, and from this density the tune shifts can be computed (in this case, we have used the "Modified static cloud model": see Section 1.2.1.4). These calculations can be

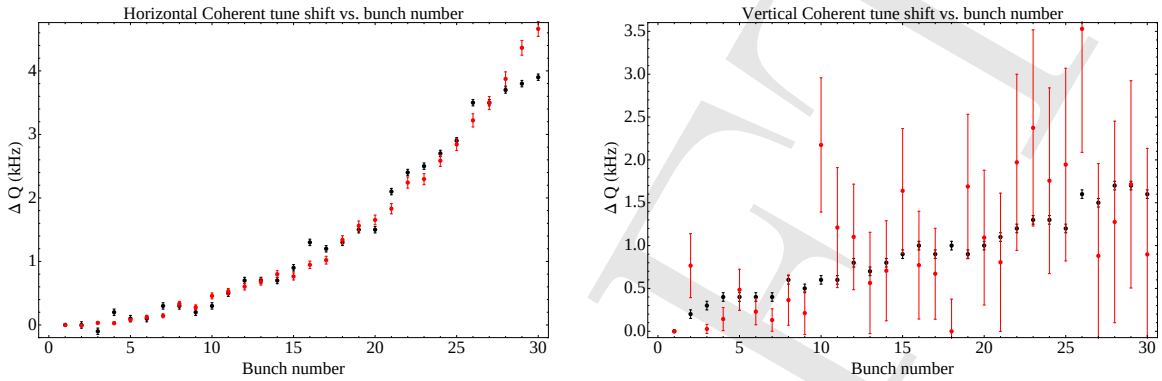

Figure 1.40: Data set 166 tune shifts: comparison between data (black) and simulation (red) from `POSINST` with parameters given in Table 1.1. Left: Horizontal tune shift vs. bunch number; right: Vertical tune shift vs. bunch number.

compared with the measured tune shifts shown in Fig. 1.39. Comparisons between simulations and measurements are shown in Fig. 1.40. The key parameters used in the `POSINST` simulation are given[7] in Table 1.1 (in Section 1.3.1).

The error bars on the simulated points are due to macroparticle statistics; for the vertical tune shifts, the comparison would benefit from an increased number of macroparticles, which was not feasible due to computer run time limitations. Nevertheless, inspection of Fig. 1.40 indicates that the simulation compares well with the data.

1.3.2.4 Estimates of the electron cloud density at the instability threshold

Cloud density from measured betatron tune shifts In this section, the measured tune shifts are used to estimate the average electron cloud density. For a lattice in which the beta functions are equal in both planes, the electron-cloud-induced tune shifts δQ_x and δQ_y may be directly related to the average electron cloud density $\langle \rho_c \rangle$ via the relation

$$\langle \rho_c \rangle = \gamma \frac{\delta Q_x + \delta Q_y}{r_e \langle \beta \rangle C}, \tag{1.58}$$

in which $\langle \beta \rangle$ is the average beta function, C is the ring circumference, γ is the beam Lorentz factor, and r_e is the classical electron radius. This relation may be used to obtain an estimate of the cloud density along the train. For CesrTA we use $C = 649$ m (sum of all drift and dipole lengths) and $\langle \beta \rangle = 16$ m. The cloud densities for each bunch resulting from this calculation are shown as the red points in Fig. 1.41.

[7] Except for the total secondary yield, which was 2.05.

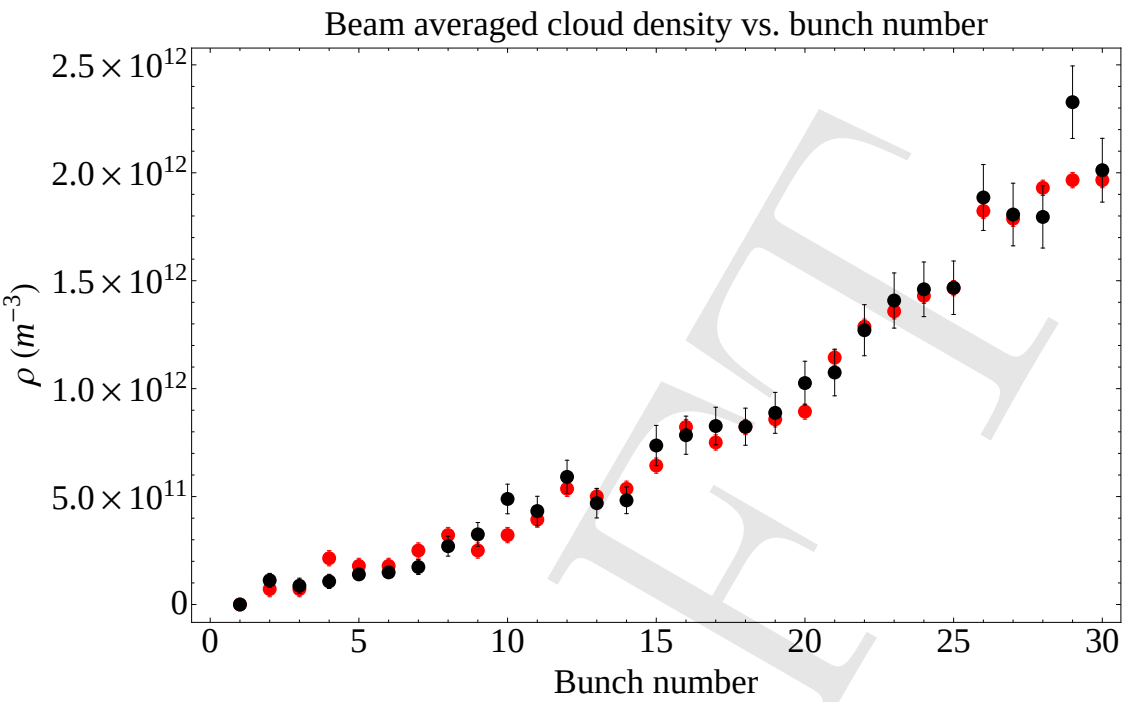

Figure 1.41: Data set 166: Average initial (i.e., before the "pinch") electron cloud density vs. bunch number, comparison between estimate from measured tune shifts (red), and simulation (black) from `POSINST` with parameters given in Table 1.1.

Comparison with electron cloud buildup simulations We can compare the cloud density, obtained from the measured tune shifts, with the density obtained from the `POSINST` simulations discussed in the previous section. This comparison is shown in Fig. 1.41. For the simulation result, shown as black dots in the figure, the cloud density is evaluated at the time corresponding to the leading edge of the bunch (i.e., before the "pinch"), and is averaged over the transverse profile of the beam. The density shown is the weighted average over drifts (total length 175 m) and dipoles (total length 474 m). It is clear from Fig. 1.41 that the cloud density computed directly from the tune shifts is quite close to the simulation result.

1.3.2.5 Vertical head-tail lines

Head-tail line power and frequency characteristics As shown in Fig. 1.35 and Fig. 1.36, there are two lines which appear in the bunch-by-bunch power spectrum, starting part way along the train, which have frequencies which are close to the betatron frequency plus and minus the synchrotron frequency. In Fig. 1.42, we plot the power and frequency (relative to the vertical betatron line, $\pm$ the synchrotron frequency) of these lines . We associate the lower frequency line with the $m = -1$ head-tail line, which arises as a result of head-tail bunch motion driven by the broadband impedance of the electron cloud. Similarly, we associate the higher frequency line with the $m = +1$ head-tail line. From Fig. 1.42, we see that these lines appear above the noise level around bunch 15 or 16. The $m = -1$ line is somewhat more strongly excited than the $m = +1$ line.

Observations of beam size growth under similar beam conditions (see Section 1.3.4) show rapid

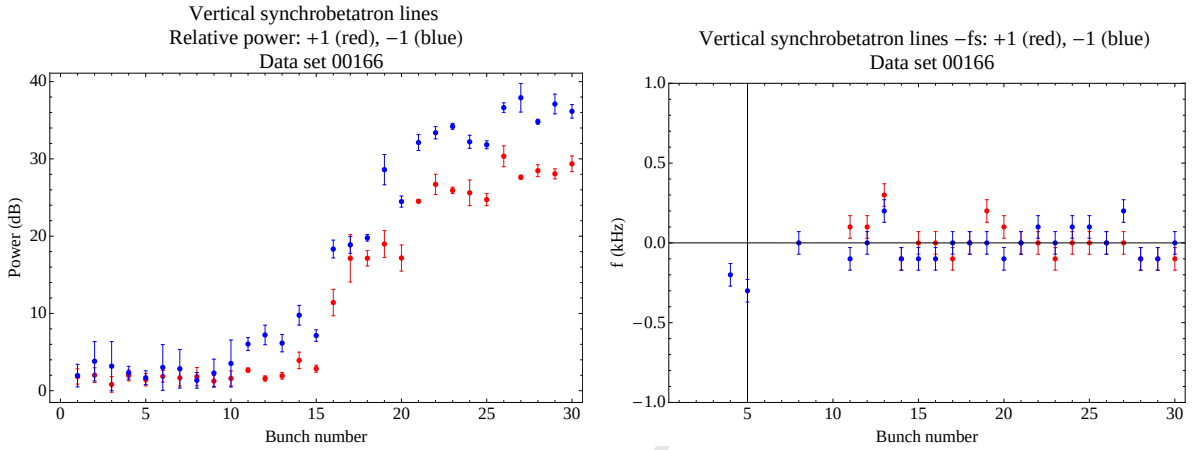

Figure 1.42: Data set 166: Vertical head tail lines: left, peak power vs. bunch number; right, frequency difference from vertical betatron line vs. bunch number, with the synchrotron frequency removed from the offset. Chromaticity: (H,V) = (1.33, 1.16). Bunch current = 0.74 mA.

emittance growth starting at about the same point in the train.

Fig. 1.42 shows that, for bunch numbers greater than about 15, where the head-tail lines appear above the background, the frequency of these head-tail lines, relative to the vertical line, is equal to the synchrotron frequency (within the errors).

Head-tail lines: correlation with cloud density Comparing Fig. 1.41 and Fig. 1.42, the average electron cloud density at which the head-tail lines are first observed can be established. For the conditions of data set 166, the head-tail lines emerge at an initial (i.e., before the "pinch") beam-averaged cloud density around 8×10^{11} m^{-3}.

1.3.2.6 Reproducibility

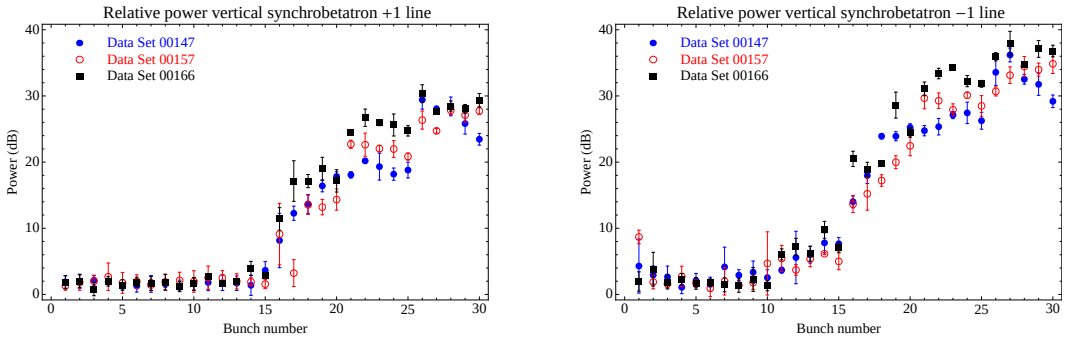

Figure 1.43: Data sets 147, 157 and 166: vertical head-tail lines compared. All sets have the same nominal bunch current and chromaticity.

The reproducibility of the observations of the head-tail lines is illustrated in Fig. 1.43. This plot shows the power in the vertical head-tail lines for three data sets taken on different dates (data set

147 on 9/25/2010, data set 157 on 9/26/2010, and data set 166 on 9/28/10) but under the same nominal machine and beam conditions. Fig. 1.43 shows that the head-tail line observations are reasonably reproducible when the machine is set to the same nominal conditions.

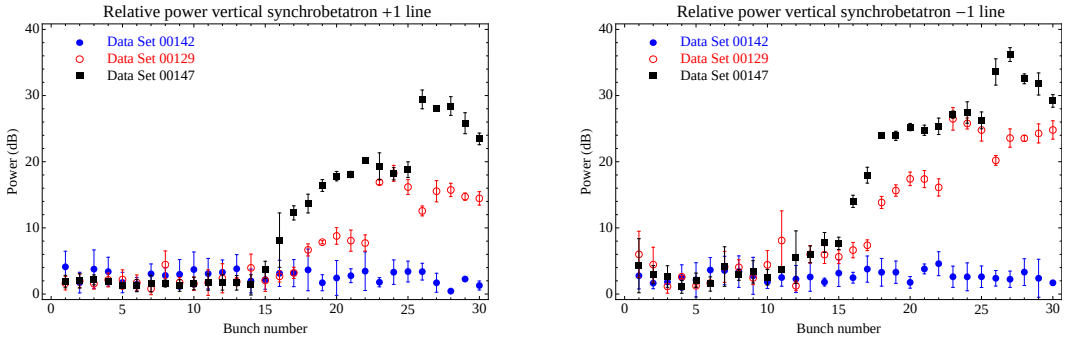

Figure 1.44: Data sets 142, 129 and 147: vertical head-tail lines compared. All sets have the same nominal bunch current (about 0.75 mA) but different chromaticities, as follows: 142: (H,V) = (1.34, 1.99); 129: (H,V) = (1.07, 1.78); 147: (H,V) = (1.33, 1.16)

1.3.2.7 Chromaticity dependence

The chromaticity dependence of the head-tail lines is illustrated in Fig. 1.44. For all data sets, the nominal bunch current was abut 0.74 mA. We see that for data set 142, with a higher value of the vertical chromaticity than data set 147, there are no head-tail lines observed. For data set 129, with lower values of both chromaticities than data set 142, but a higher value of the vertical chromaticity than data set 147, head-tail lines are observed, but their onset is a few bunches later in the train, and the excitation levels are lower, than in data set 147, which has the lowest vertical chromaticity.

1.3.2.8 Current dependence

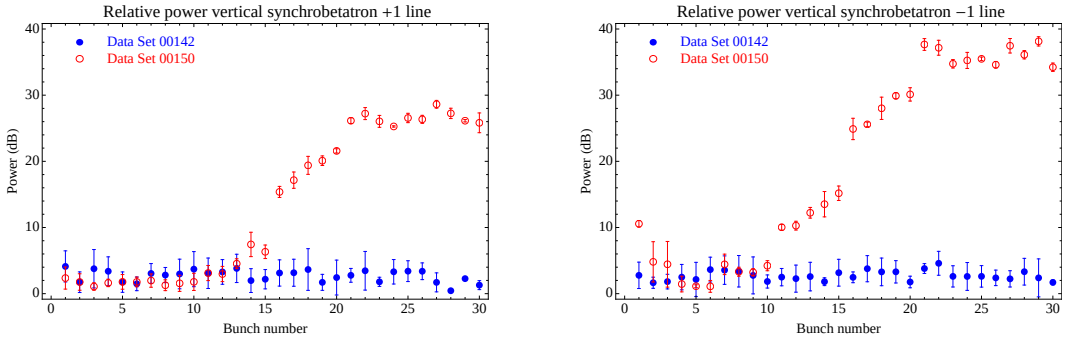

Figure 1.45: Data sets 142 and 150: vertical head-tail lines compared. Both sets have the same chromaticity [(H,V) = (1.34, 1.99)] but different bunch currents as follows: 142: 0.74 mA; 150: 0.95 mA

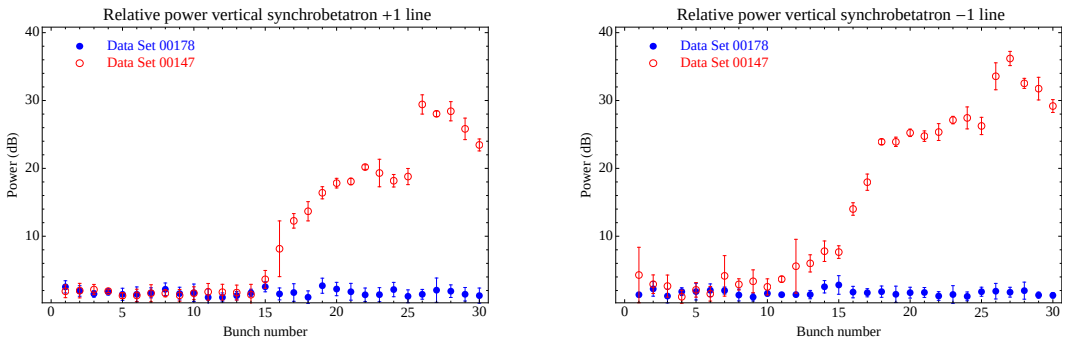

Figure 1.46: Data sets 147 and 178: vertical head-tail lines compared. Both sets have the same chromaticity [(H,V) = (1.33, 1.16)] but different bunch currents as follows: 147: 0.74 mA; 178: 0.5 mA

The current dependence of the head-tail lines is illustrated in Fig. 1.45 and Fig. 1.46. In Fig. 1.45, both data sets have the same chromaticity, but the data set with the lower bunch current (data set 142) shows no head-tail lines, while the higher current data set (data set 150) shows head-tail lines staring to emerge around bunch 12. Similarly, in Fig. 1.46, both data sets have the same (lower) chromaticity, but the data set with the lower bunch current (data set 178) shows no head-tail lines, while the higher current data set (data set 147) shows head-tail lines staring to emerge around bunch 13.

1.3.2.9 Bunch number dependence

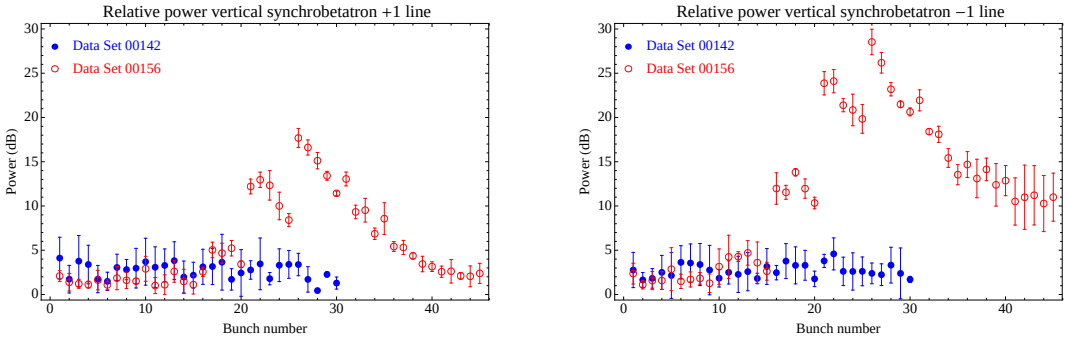

Figure 1.47: Data sets 142 and 156: vertical head-tail lines compared. Both sets have the same chromaticity [(H,V) = (1.34, 1.99)] and bunch current (0.74 ma), but different numbers of bunches, as shown in the figure. The increased amplitude in data set 156 at bunches 21 and 26 is an artifact due to refilling of the train at these bunch numbers.

The bunch number dependence of the head-tail lines is illustrated in Fig. 1.47. Both data sets have the same chromaticity and bunch current, but data set 156 contains 45 bunches in the train. The vertical tunes of the first bunch were slightly different for the two runs: for run 142, it was about 227 kHz, while for run 156 the tune was about 221 kHz. No head-tail lines are observed in data set 142 out to the end of the train, bunch 30. But with 45 bunches, head-tail lines are observed starting around bunch 18, then growing to a peak around bunch 25, and falling off at the end of

the train. The fact that the head-tail lines are seen with a 45 bunch train with the same bunch current as a 30 bunch train for which no lines are seen, is suggestive that there is a residual cloud density which lasts more than one turn, and which depends on the total current.

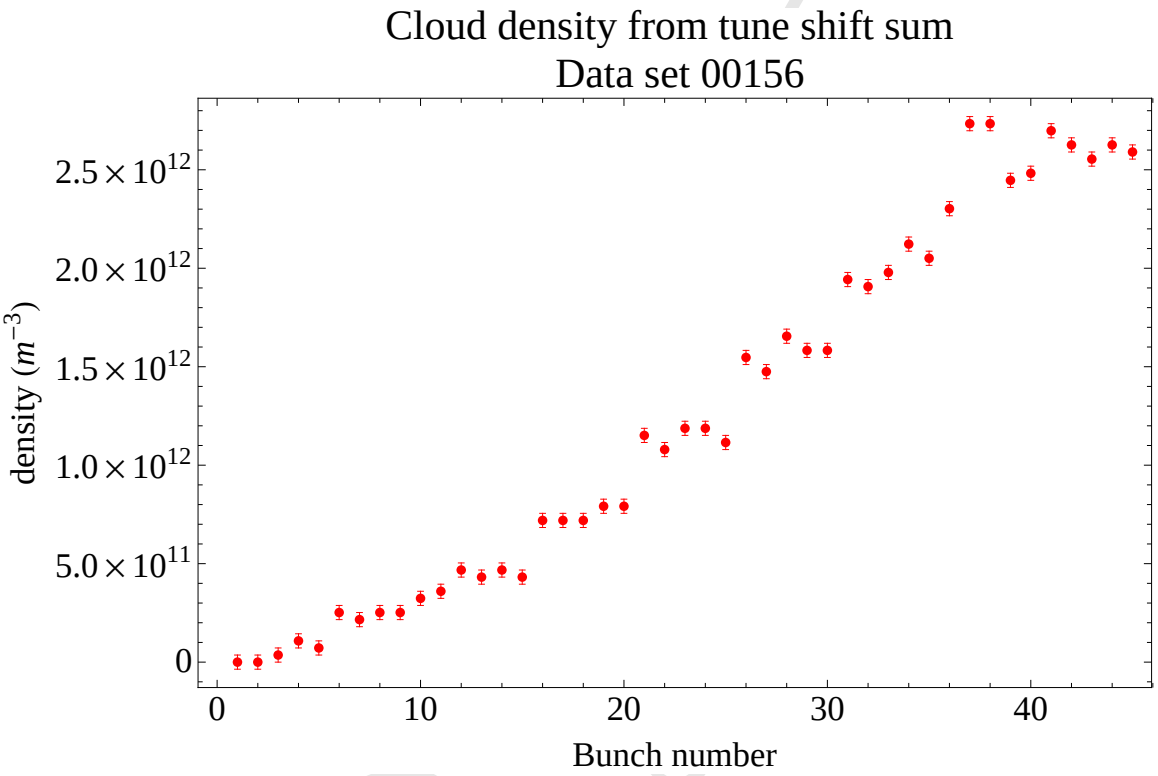

Figure 1.48: Data set 156: Average initial electron cloud density vs. bunch number, estimate from measured tune shifts

45 bunch train: Correlation with cloud density In Fig. 1.48, we show the cloud density as a function of bunch number, computed from the measured tune shifts, as discussed above. Comparison with Fig. 1.47 shows that the head-tail lines emerge from the background at a cloud density of about 8×10^{11} m^{-3}, which is the same as the threshold density found for data set 166, even though the vertical chromaticity was higher for data set 156. The fall-off of the head-tail lines after bunch 25 suggests that the instability is saturating. Yet the cloud density continues to increase after bunch 25 (at least until around bunch 35) as Fig. 1.48 shows. The head-tail instability threshold is expected to be sensitive to the vertical beam size, so what may be happening is that the instability is driving vertical beam size growth along the train, and the increase in the threshold as the beam size increases provides a mechanism for the instability to saturate.

1.3.2.10 Synchrotron tune dependence

The synchrotron tune dependence of the head-tail lines is illustrated in Fig. 1.49. Both data sets have the same chromaticity and bunch current, but data set 151 has a reduced synchrotron frequency of 20.7 kHz, and an increased bunch length of 12.8 mm. The nominal frequency and bunch length, for data set 147, are 25.4 kHz and 10.8 mm.

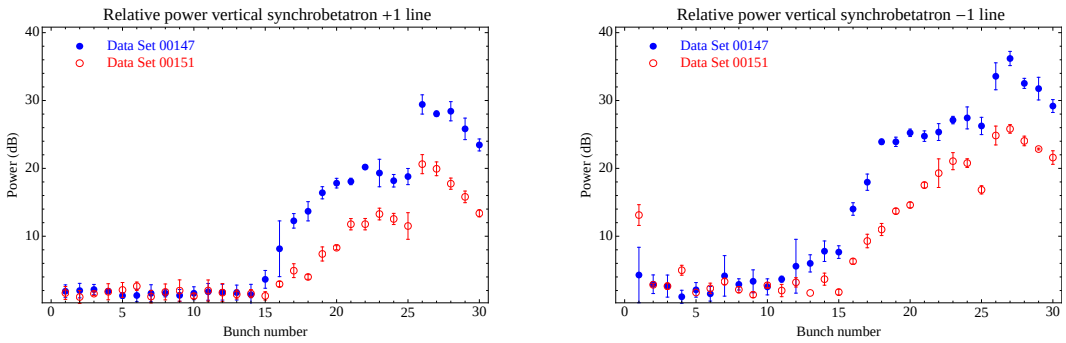

Figure 1.49: Data sets 147 and 151: vertical head-tail lines compared. Both sets have the same chromaticity [(H,V) = (1.33, 1.16)] and bunch current (0.74 mA), but different values of the bunch length and synchrotron frequency, as follows: 147, $f_s = 25.4$ kHz and $\sigma_z = 10.8$ mm; 151, $f_s = 20.7$ kHz and $\sigma_z = 12.8$ mm.

For both data sets, the separation between the vertical betatron lines and the head-tail lines equals the synchrotron frequency. Fig. 1.49 shows that the head-tail line threshold is about the same in both cases, but the power in the lines grows more slowly with bunch number for the data set with a reduced synchrotron frequency, and longer bunch length.

1.3.2.11 Single-bunch vertical emittance dependence

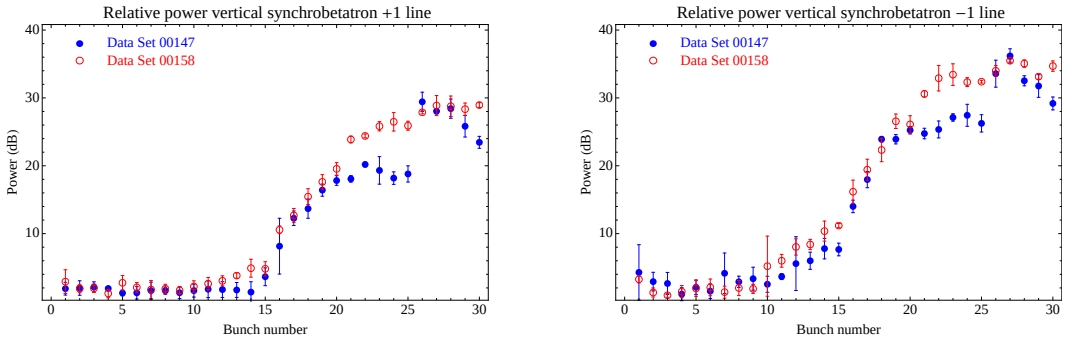

Figure 1.50: Data sets 147 and 158: vertical head-tail lines compared. Both sets have the same chromaticity [(H,V) = (1.33, 1.16)] and bunch current (0.74 mA), but different values of the single-bunch vertical emittance, as follows: 147, Vertical emittance $\sim$ 20 pm; 158, Vertical emittance $\sim$ 300 pm

The vertical emittance dependence of the head-tail lines is illustrated in Fig. 1.50. Both data sets have the same chromaticity and bunch current, but data set 158 has an increased single-bunch vertical emittance of 300 pm[8]. The nominal single-bunch vertical emittance, for data set 147, is $\sim$ 20 pm.

Fig. 1.50 shows that the head-tail line growth is very similar for the two different vertical emittances. The power in the lines seems to saturate at a lower level for the data set with smaller vertical

[8]This number was estimated from a lattice model, not directly measured.

emittance. However, there is not a great deal of difference, which is peculiar, since the electron cloud head-tail instability is expected to be considerably more severe for smaller vertical emittance. Another observation which explores the vertical emittance dependence of the head-tail lines is shown

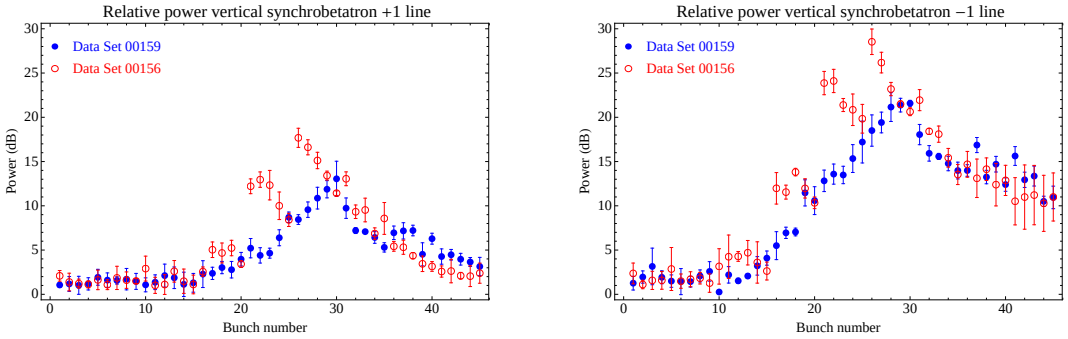

Figure 1.51: Data sets 156 and 159: vertical head-tail lines compared. Both sets have 45 bunches, the same chromaticity [(H,V) = (1.34, 1.99)] and bunch current (0.74 mA), but different values of the single-bunch vertical emittance, as follows: 156, Vertical emittance $\sim$ 20 pm; 159, Vertical emittance $\sim$ 300 pm

in Fig. 1.51. Both data sets have 45 bunches and have the same chromaticity and bunch current, but data set 159 has an increased single-bunch vertical emittance of $\sim$ 300 pm. The single-bunch vertical emittance, for data set 156 is $\sim$ 20 pm.

Inspecting Fig. 1.51, we see that, in this case, the power in the lines peaks at a lower level, and at a later bunch, for the data set with larger vertical emittance. This would suggest that the instability is stronger for the case of smaller vertical emittance, as expected.

1.3.2.12 Vertical feedback dependence

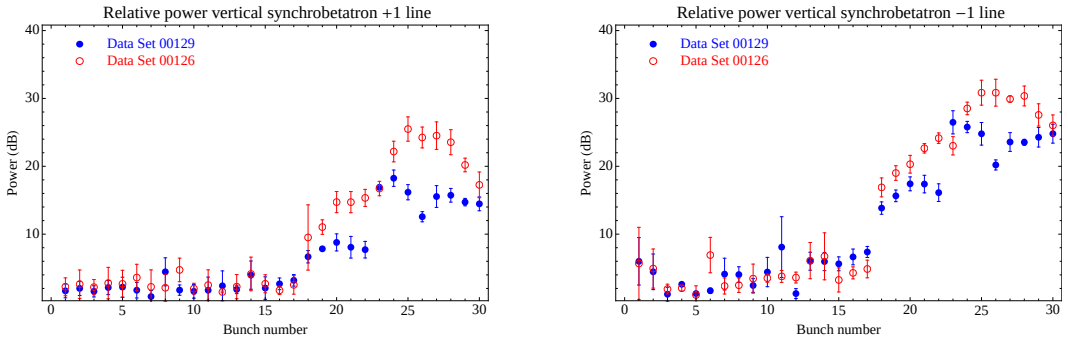

Figure 1.52: Data sets 126 and 129: vertical head-tail lines compared. Both sets have the same chromaticity and bunch current, but different values of the vertical feedback, as follows: 126, Vertical feedback off; 129, Vertical feedback at 20% of full gain.

The vertical feedback dependence of the head-tail lines is illustrated in Fig. 1.52. Both data sets have the same chromaticity and bunch current, but data set 126 has the vertical (dipole) feedback

off. For data set 129, as for all the other data sets discussed here (except 126), the vertical feedback is set to 20% of full gain.

Fig. 1.52 shows that the head-tail line threshold is about in the same place for these two data sets. But for data set 126 (feedback off), the power peaks a few dB higher than for data set 126, and then falls off.

1.3.2.13 Beam energy dependence

In data set 165, the structure of the frequency spectrum was studied for a beam energy of 4 GeV. Fig. 1.53 shows the beam current as a function of bunch number for this data set. The bunch current was about 1.1 mA/bunch. The machine parameters for this measurement are presented in Table 1.5

Power spectrum Fig. 1.54 shows the power spectrum as a function of bunch number. Clearly visible are the horizontal and vertical betatron lines, the head-tail line above the vertical, and another line around 285 kHz. The line at 285 kHz corresponds to excitation of the $Q_x + 2Q_y = 2$ resonance.

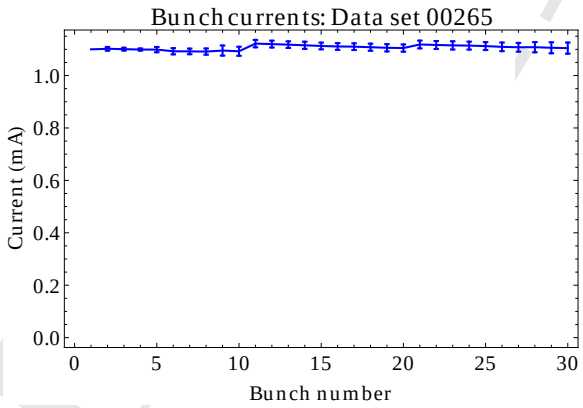

Figure 1.53: Data set 265: Bunch-by-bunch currents, 4 GeV beam energy

Betatron lineshapes Fig. 1.55 shows the bunch-by-bunch power spectrum near the horizontal betatron line. As at 2 GeV, there is a major peak which shifts up in frequency by about 4 kHz during the bunch train. This shift is attributable to the electron cloud. Fig. 1.56 shows the bunch-by-bunch power spectrum near the vertical betatron line. There is considerably more structure in this line than at 2 GeV, including a splitting of the main peak which persists throughout the train, and some smaller satellite peaks which seem to develop after bunch 20.

Vertical head-tail lines In Fig. 1.57, we plot the power and frequency (relative to the vertical betatron line, $\pm$ the synchrotron frequency) of the head-tail lines. We see that these lines appear above the noise level around bunch 18. The lower frequency line ($m = -1$ head-tail line) is close to the horizontal line, and is weakly excited, so its power is not well determined, and it is omitted from the frequency plot. The frequency plot shows that, for the ($m = +1$ head-tail line), the head-tail

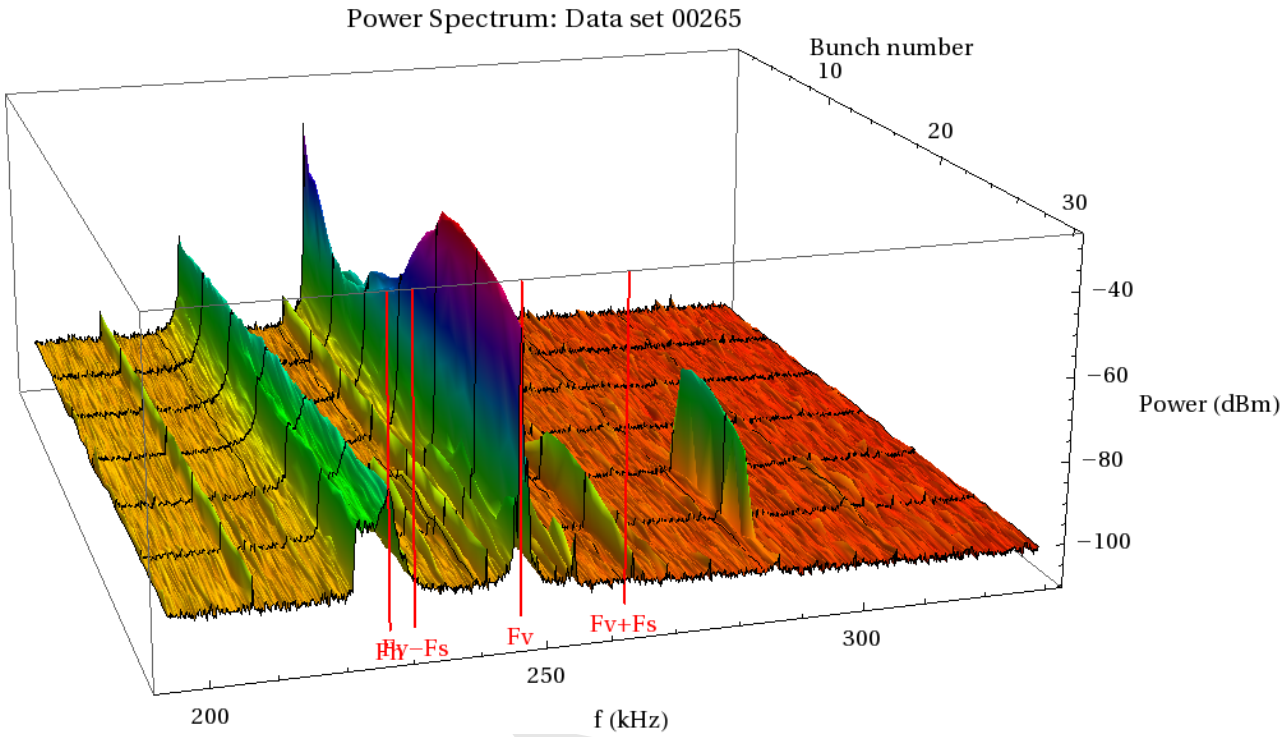

Figure 1.54: Data set 265: Bunch-by-bunch power spectrum, 4 GeV. Chromaticity: (H,V) = (1.3, 1.4). Bunch current = 1.1 mA.

line frequency minus the vertical betatron line frequency differs from the synchrotron frequency by about 1 kHz. This is in contrast to the observations made at 2 GeV, for which this difference is essentially zero.

Instability threshold estimate In Fig. 1.58, we show the cloud density as a function of bunch number, computed from the measured tune shifts, as discussed above. Comparison with Fig. 1.57 shows that the head-tail lines emerge from the background at a cloud density of about 2×10^{12} m^{-3}.

1.3.2.14 Particle species dependence

The species dependence of the bunch-by-bunch power spectrum is illustrated by comparing data set 166 (Fig. 1.35) and data set 154 (Fig. 1.59). Both data sets have the same chromaticity and bunch current, but data set 154 is for electrons. For electrons, we see less vertical excitation along the train, and smaller head-tail line excitation, than for positrons. The large tune shifts observed with the positron beam are also absent. The details of the different structures of the head-tail lines for electrons and positrons can be seen in Fig. 1.60. For electrons, the head-tail lines start later in the train, grow more slowly, and at their maxima are 20 dB lower than the positron head-tail lines.

The positron head-tail excitation is presumably due to electron cloud effects. The physical mechanism responsible for the head-tail excitation in the electron case is not likely to be either electron

Table 1.5: Nominal machine parameters at 4 GeV. The emittances and tunes are those of a single bunch in the machine.

Parameter	Unit	Value
Energy	GeV	4.00
Lattice		4000mev_23nm_20090816
Horizontal emittance	nm	23
Vertical emittance	pm	~ 180
Bunch length	mm	17.2
Horizontal tune		14.55
Vertical tune		9.58
Synchrotron tune		0.041
Momentum compaction		6.3×10^{-3}
Revolution frequency	kHz	390.13

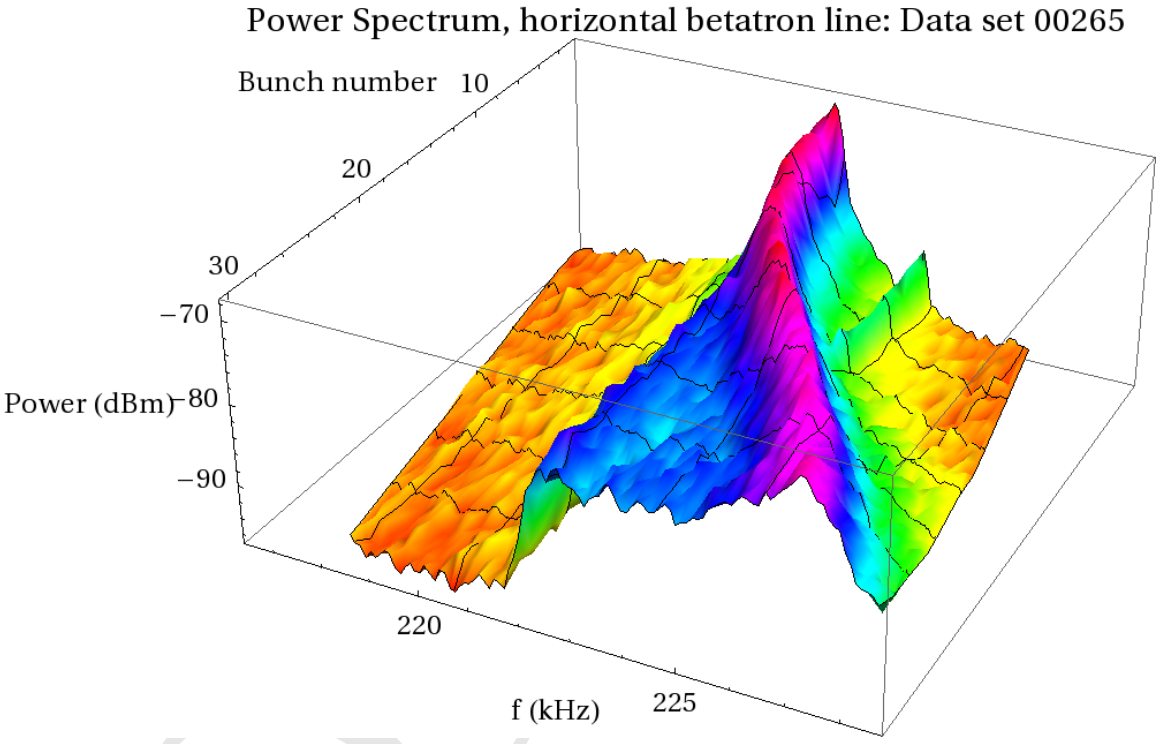

Figure 1.55: Data set 265: Bunch-by-bunch power spectrum: detail at horizontal betatron line, 4 GeV. Chromaticity: (H,V) = (1.3, 1.4). Bunch current = 1.1 mA.

cloud or positive ions. It may be due to the broad-band impedance of the machine itself.

1.3.2.15 Precursor bunch dependence

In Fig. 1.61, the power spectrum of bunch 1 for data set 151 is shown (red trace). Note the presence of a prominent $m = -1$ head-tail line. This line disappears for the second bunch, and does not re-appear until much later in the train, as shown in Fig. 1.62. Moreover, beam size measurements (see Section 1.3.4) indicate that the first bunch in the train is frequently larger in size than the

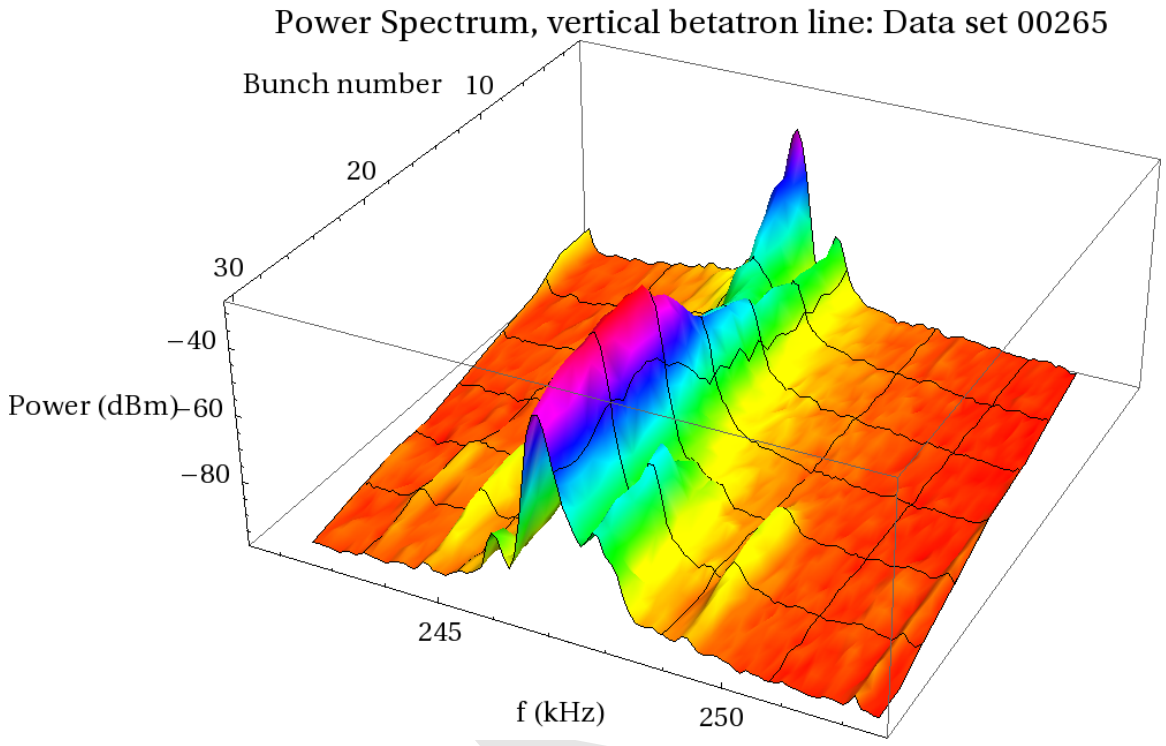

Figure 1.56: Data set 265: Bunch-by-bunch power spectrum: detail at vertical betatron line, 4 GeV. Chromaticity: (H,V) = (1.3, 1.4). Bunch current = 1.1 mA.

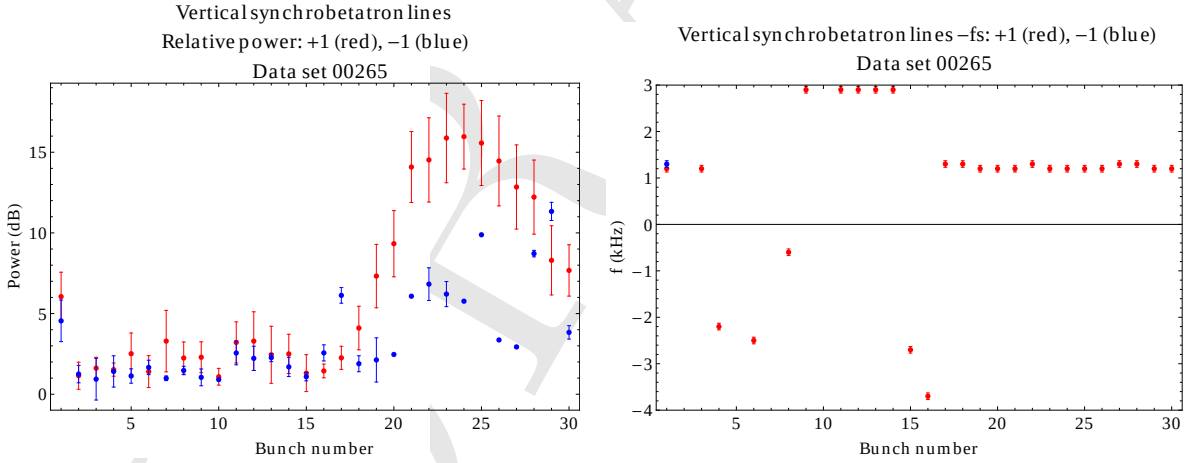

Figure 1.57: Data set 265: Vertical head tail lines: left, peak power vs. bunch number; right, frequency difference from vertical betatron line vs. bunch number, with the synchrotron frequency removed from the offset. Beam energy 4 GeV. Chromaticity: (H,V) = (1.3, 1.4). Bunch current = 1.1 mA.

next few bunches.

This suggests that the cloud density near the beam, which persists after the train ends, may be sufficiently high, even for the first bunch in the train, that spontaneous head-tail motion occurs. However, the interaction of the first bunch with this cloud evidently decreases the cloud density

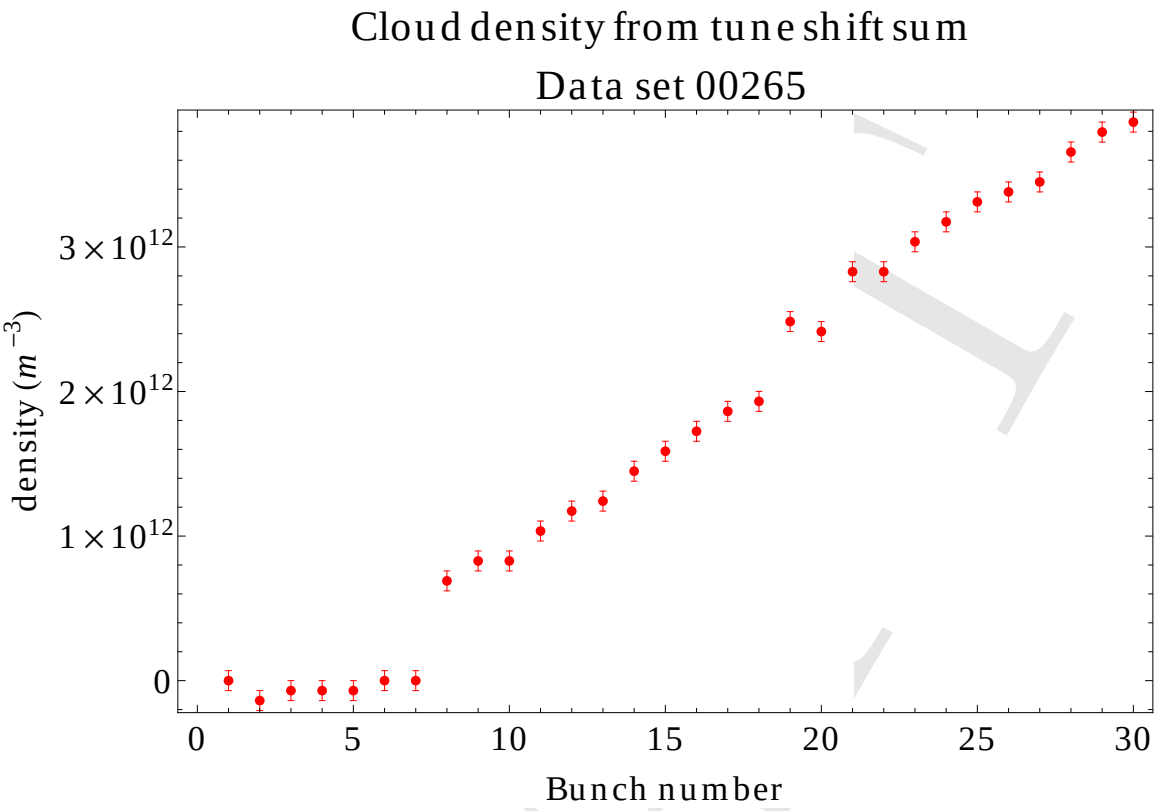

Figure 1.58: Data set 265: Average initial electron cloud density vs. bunch number, estimate from measured tune shifts. 4 GeV beam energy.

near the beam, so that bunch 2 does not suffer from spontaneous head-tail motion.

Simulations and witness bunch measurements indicate that the electron cloud lifetime in dipoles and drifts is much shorter than one turn in CesrTA. Cloud density which persists for many turns may be due to trapped cloud in quadrupoles and wigglers. Simulations and RFA measurements in quadrupoles have both indicated that trapped cloud may be present.

To test this hypothesis, in data set 153, a 0.75 mA "precursor" bunch was placed 182 ns before bunch 1. Otherwise, conditions were the same as for data set 151. The spectrum of the first bunch for data set 153 is shown (blue trace) in Fig. 1.61. Note that the lower head-tail line is now absent. In addition, the structure seen on the upper edge of the vertical betatron line in Fig. 1.61 is disappears. Finally, there is a small line at 235.7 kHz (13.6 kHz above the vertical betatron line) which also disappears when the precursor bunch is introduced.

It is quite interesting to note that the frequency difference between the head-tail line of the first bunch for data set 151 (shown in Fig. 1.61) and the vertical betatron line is 20.2 ± 0.1 kHz, which is significantly different from the synchrotron frequency, 20.7 kHz. The head-tail lines which develop later in the train, both above and below the vertical betatron line, always have a separation equal to the synchrotron frequency, within the measurement errors (see Fig. 1.39).

We have observed a prominent $m = -1$ head-tail line for the first bunch in the train in two other data sets: data set 150 (see Fig. 1.45) and data set 157 (see Fig. 1.43). In both of these cases, the $m = -1$ line is separated from the vertical betatron line by significantly less (typically 0.6 to

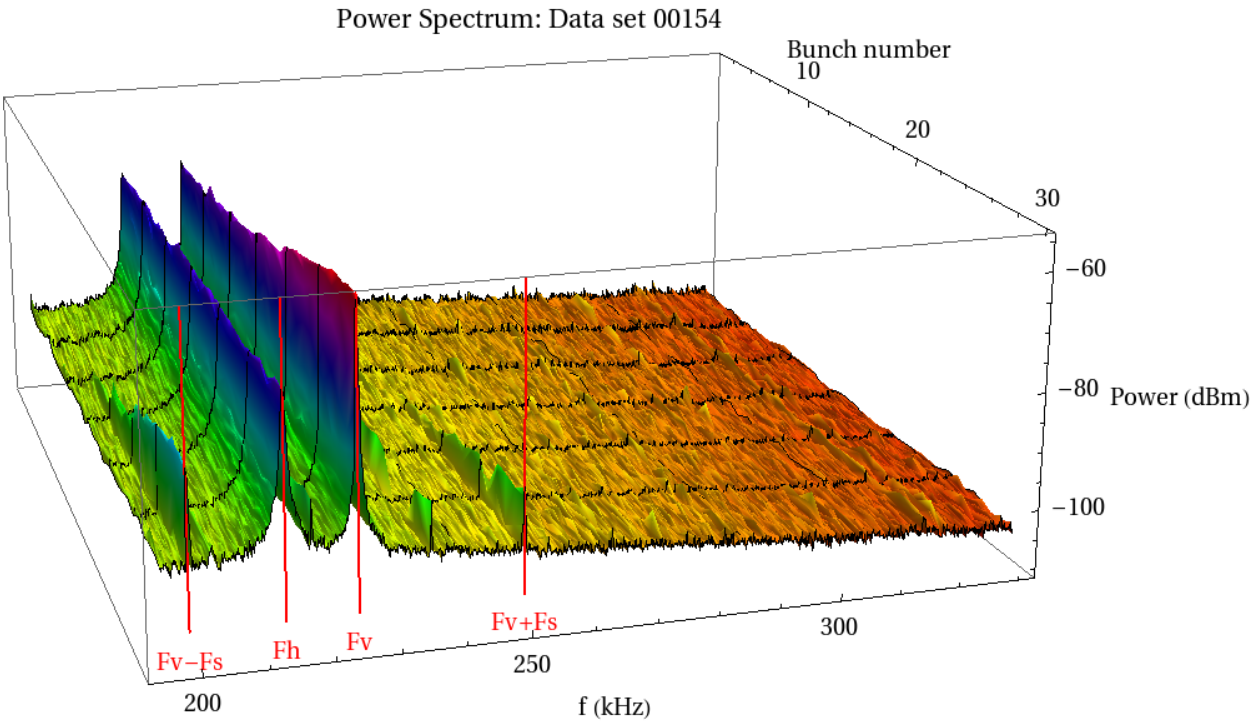

Figure 1.59: Data set 154: Bunch-by-bunch power spectrum. This data set is for electrons, but has the same chromaticity and bunch current parameters as data set 166 (Fig. 1.35).

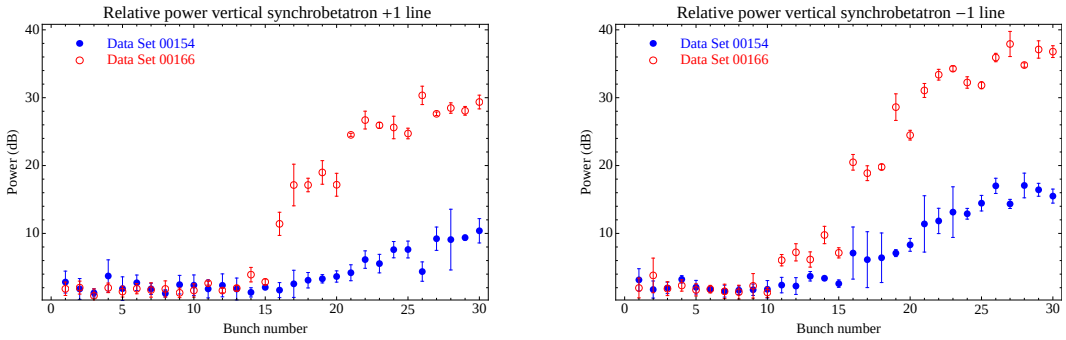

Figure 1.60: Data sets 166 and 154: vertical head-tail lines compared. Both sets have the same chromaticity and bunch current, but data set 166 was taken with positrons, and data set 154 was taken with electrons

0.7 kHz) than the synchrotron frequency , and there is a doublet structure to the vertical betatron line, as shown in Fig. 1.61 for data set 151. In Fig. 1.62, the power in the vertical head-tail lines is shown as a function of bunch number, for data sets 151 and 153. The figure shows little difference between the head-tail line growth for the two data sets. The data set without the precursor bunch has a slightly higher line power near the end of the train.

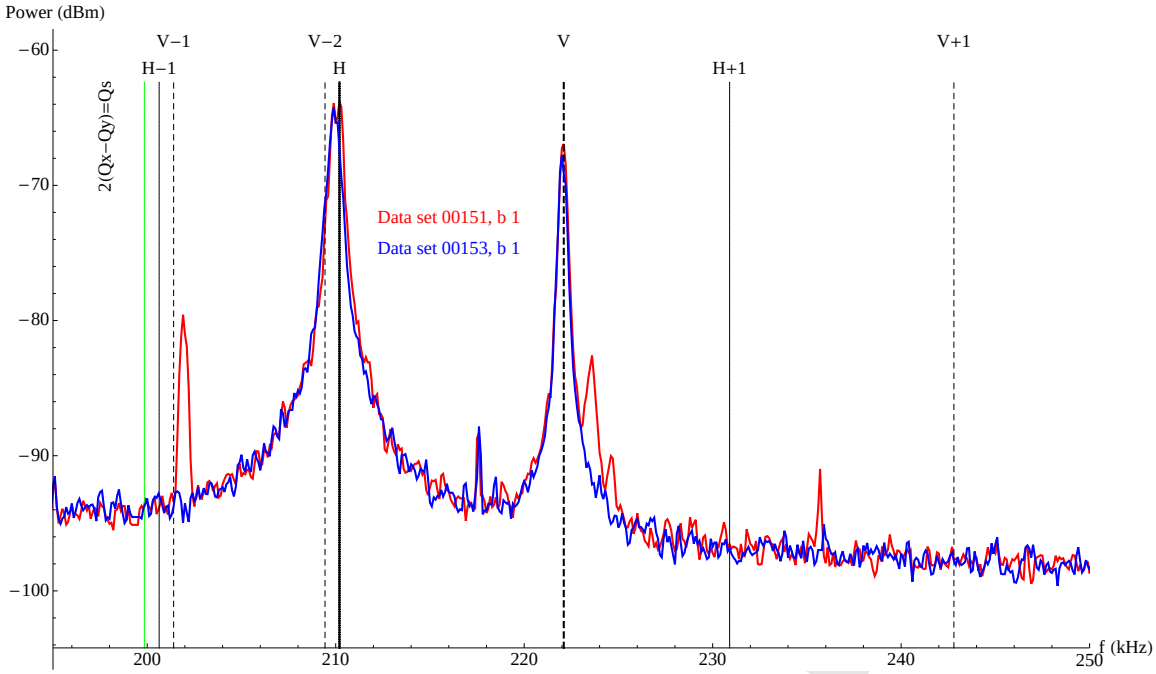

Figure 1.61: Data set 151 and 153 : Power spectrum, bunch 1 compared. The lines labelled, for example,"V+1" and "V-1" are shown at frequencies of $\pm f_s$ from the vertical betatron line ("V"), in which f_s is the synchrotron frequency. For these data sets, $f_s = 20.7$ kHz. The location of a machine resonance is also indicated.

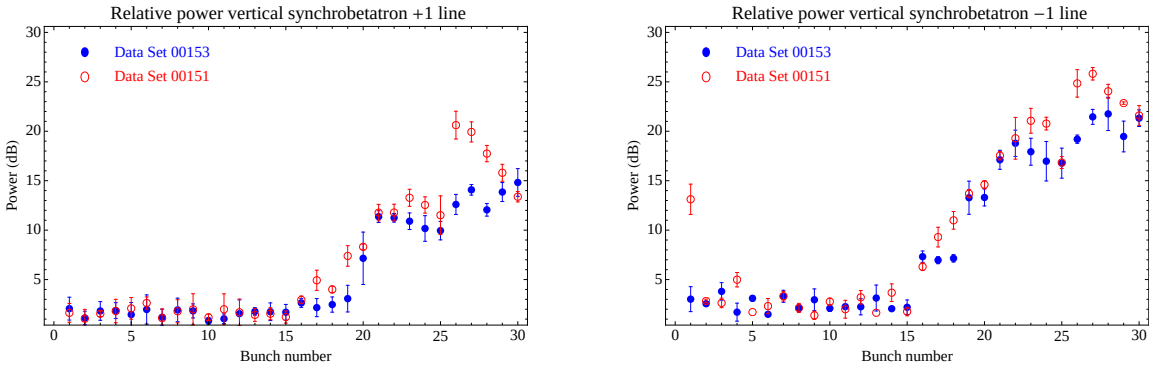

Figure 1.62: Data sets 151 and 153: vertical head-tail lines compared. Both sets have the same chromaticity and bunch current, but there is a precursor bunch present for data set 153, as described in the text.

1.3.2.16 Single bunch current variation experiment

To explore further the dynamics of the interaction of the last bunch in the train with the cloud, a series of power spectral measurements were made, in which the current in the first 29 bunches in a 30 bunch train was fixed, but the current in the last bunch was varied. The power spectrum with the last bunch at 0.25 mA (data set 167) is compared with the power spectrum with the last bunch at 1.25 mA (data set 171) in Fig. 1.63.

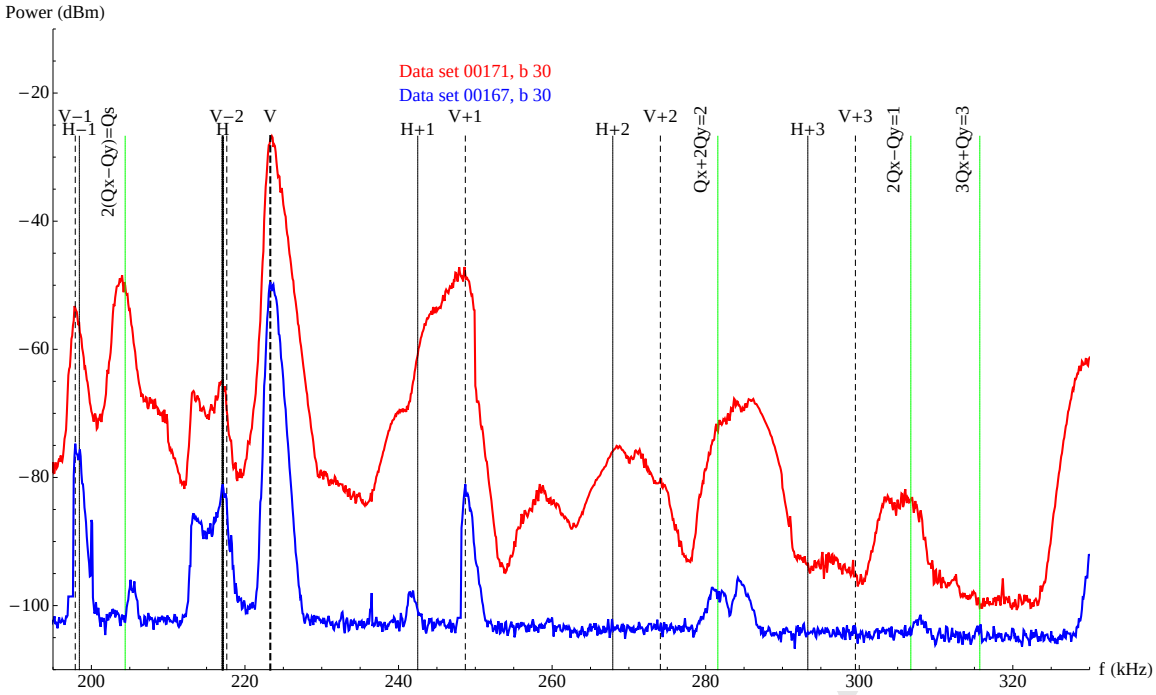

Figure 1.63: Data set 167 and data set 171: Power spectrum, bunch 30 compared. The lines labelled, for example,"V+1" and "V-1" are shown at frequencies of $\pm f_s$ from the vertical betatron line ("V"), in which f_s is the synchrotron frequency. The locations of several machine resonances are also indicated.The first 29 bunches had a nominal current of 0.75 mA/bunch. Chromaticity: (H,V) = (1.33, 1.16). For data set 167, bunch 30 had a current of 0.25 mA. For data set 171, bunch 30 had a current of 1.25 mA.

The vertical excitation of the bunch, both at the vertical betatron line and at the head-tail lines, is much larger for the higher current bunch. The $m = +1$ head-tail line appears to acquire a low-frequency shoulder at the higher current.

In addition, the frequency of the vertical betatron line is almost independent of the current in the bunch. The shift from 0.25 mA to 1.25 mA is less than 0.2 kHz. Note that this behavior is very different from what would be expected for a conventional machine impedance, for which one would expect a strong current dependence for the tune.

1.3.2.17 Conclusions

The basic observation is that, under a variety of conditions, single-bunch frequency spectra in multi-bunch positron trains exhibit the $m = \pm 1$ head-tail (HT) lines, separated from the vertical line by the synchrotron frequency, for some of the bunches during the train. A summary of more detailed observations follows in the following bullets.

- For a 30 bunch train with 0.75 mA/bunch at 2.1 GeV beam energy, the onset of the HT lines occurs at a ringwide initial (i.e., before the "pinch") beam-averaged cloud density of around 8×10^{11} m^{-3} (assuming no cloud density at the start of the train).
- For a 30 bunch train with 1.1 mA/bunch at 4 GeV beam energy, the onset of the HT lines

occurs at a ringwide initial (i.e., before the "pinch") beam-averaged cloud density of around 2×10^{12} m^{-3} (assuming no cloud density at the start of the train).

- The betatron lines exhibit structure which varies along the train. The vertical line power grows along the train and has a fine structure that is not understood.
- The onset of the HT lines depends strongly on the vertical chromaticity, the beam current and the number of bunches.
- For a 45 bunch train, the HT lines have a maximum power around bunch 30; the line power is reduced for later bunches.
- There is a weak dependence of the onset of the HT lines on the synchrotron tune, the single-bunch vertical emittance, and the vertical feedback. The relatively weak dependence of the HT line onset on the single-bunch vertical emittance is contrary to expectations for the electron cloud effect. It is possible that, due to incoherent emittance growth along the train, the vertical emittance of the bunch at which the instability starts is larger than the single-bunch vertical emittance.
- Under identical conditions, HT lines also appear in electron trains, but the onset is later in the train, develops more slowly, and is weaker, than for positrons. The HT excitation for electrons may be due to the broadband impedance of the ring.
- Under some conditions, the first bunch in the train also exhibits a head-tail line ($m = -1$ only). The presence of a "precursor" bunch can eliminate the $m = -1$ signal in the first bunch, and also leads to the onset of the HT lines at a later bunch in the train. The implication is that there is a significant cloud density near the beam which lasts many turns. Indications from RFA measurements and simulations indicate this "trapped" cloud may be in the quadrupoles and wigglers.
- There is a strong dependence of the HT line structure observed on last bunch in a 30 bunch train, as a function of the current in that bunch. But the frequency of the vertical betatron line of this bunch is only very weakly dependent on the current in the bunch.
- Future work will include more checks for systematics (looking at different BPMs, for example), as well as measurements at different bunch spacings and beam energies.

1.3.3 Mode Growth Rates

In addition to the power spectrum measurements described in the previous section, in which spontaneous excitations of single bunches are passively monitored, we have also made measurements in which we actively excite a single bunch in a train, and measure the rate at which the bunch damps after the excitation is turned off. These bunch-by-bunch damping rate measurements come in two varieties:

- $m = 0$ *(dipole mode).* In this case, we drive a single bunch by delivering a narrow pulse to the transverse feedback system's kicker. We observe the $m = 0$ motion (betatron line) on a button BPM, gated on the same bunch. Using a spectrum analyzer in zero span mode, tuned to the betatron line, we measure the damping rate of the $m = 0$ line's power after the drive is turned off.

- $m = \pm 1$ *(head tail modes).* In this case, we apply a CW drive to the RF cavity phase, to provide a large amplitude longitudinal excitation. We then perform a transverse drive-damp measurement, as in the previous case, but with the spectrum analyzer tuned to the head-tail line's frequency.

A number of measurements were made to investigate the systematics of this technique. More details can be found in Section 1.1.4.

Results will be shown here for five data sets in which 30 bunch trains with currents of about 0.75 mA/bunch were studied for two of the data sets and three more with currents of about 0.35 mA/bunch.

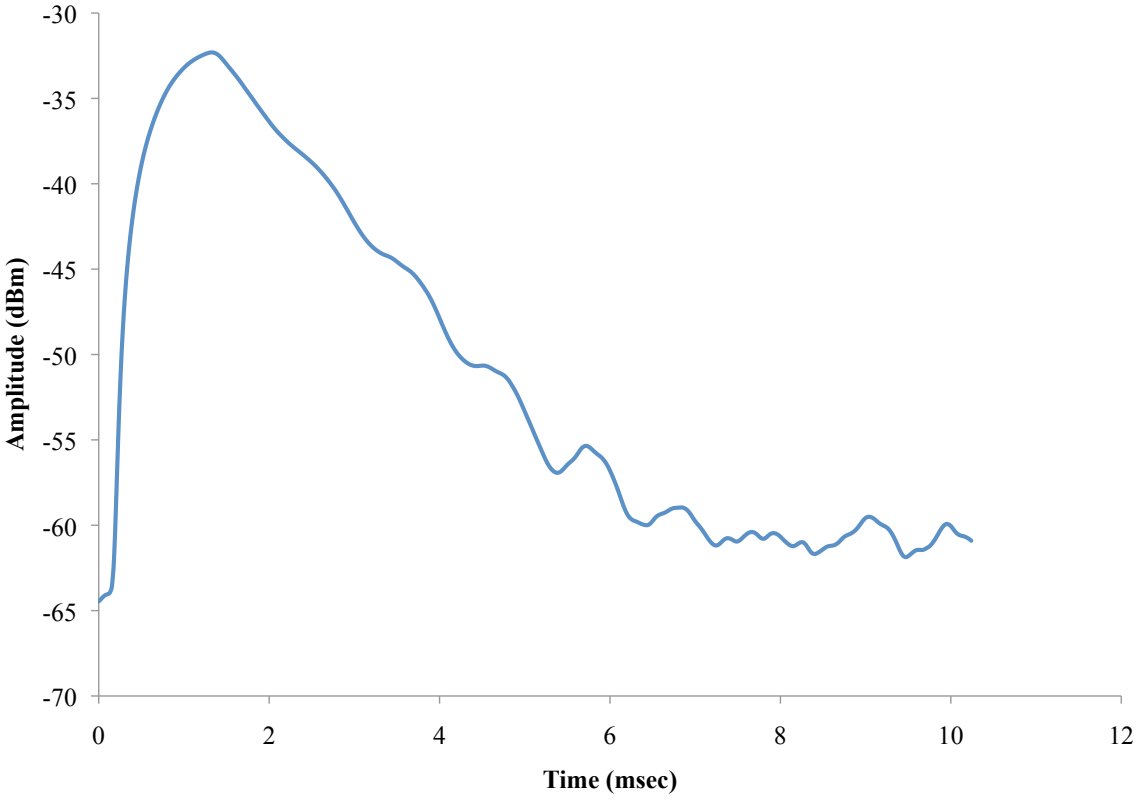

Figure 1.64: Plot of the amplitude vs. time for a drive-damp measurement of a m = 0 mode.

For the two data sets, we show the line power as a function of time, and bunch number. For data set 182 (Fig. 1.72), the $m = 0$ mode was excited and monitored. For data set 177 (Fig. 1.73), the $m = -1$ mode was excited and monitored.

Quantitative Analysis of Drive-damp Measurements The analysis of the data for these drive-damp measurements utilized two different fitting methods. The first and most obvious is to fit the amplitude of the mode spectrum to an exponential decay (or more properly, since the mode amplitude is measured in the dBm, a linear fit to the amplitude in dBm vs. time.) The second fitting method, which has been employed for all of the measurements presented here, was inspired by the observation that a number of the damping waveforms exhibit a more complicated decay than a simple exponential decay. Examples of the most common of these non-exponential decays are shown

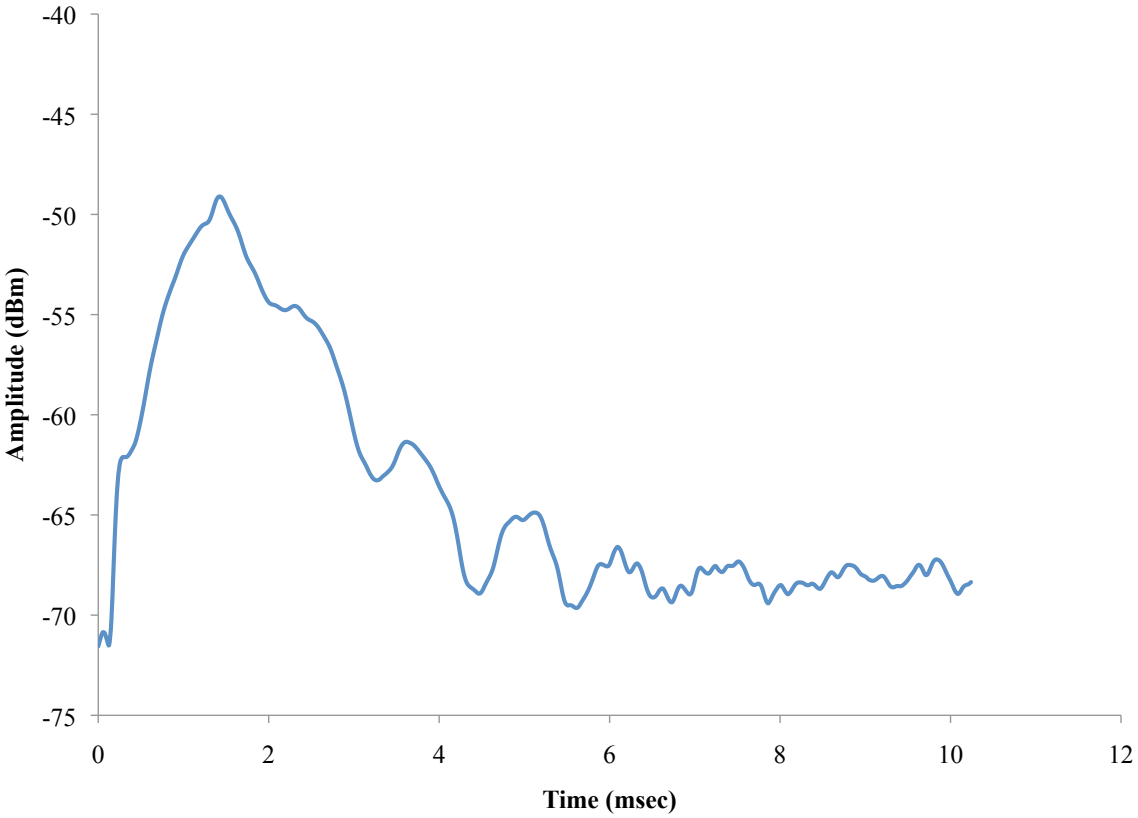

Figure 1.65: Plot of the amplitude vs. time for a drive-damp measurement of a m = -1 mode.

in Fig. 1.64 and Fig. 1.65. The characteristic feature in these two plots is an exponential decay of what appear to be two modes of slightly different frequency, generating a damped interfering decay of their combined amplitudes. There is an explanation of this effect in some cases. In the case when there is a simple exponential damped oscillation and the center frequency of spectrum analyzer is mistuned away from the actual frequency of the mode, an exponential decay with a beat frequency becomes visible with the amplitude of the beats increasing as the center frequency detuning is increased. As a result during the drive-damp measurements care is taken to manually adjust the spectrum analyzer center frequency to minimize the observed oscillation amplitude. Nonetheless in number cases there is still a significant damped oscillatory signal present in the damping plot and this may be exhibiting a real damped oscillation of two independent coupled modes of oscillation. Taking a broader view of drive-damp measurements, since the real interest is in determining the longest characteristic decay time for the mode of oscillation, one is actually interested in the amplitude envelope that fully contains the beams displacement vs. time. As a result our analysis of the damped decay of the beams vertical oscillation utilizes a fit to two modes of nearly the same frequency, each having their own damping rate. We then write the time evolution of the vertical position of a bunch as

$$y(t) = \mathrm{Re}\{Y(t)\} = \mathrm{Re}\{a_1 \exp(j\omega_1 t - \alpha_1 t) + a_2 \exp(j\omega_2 t - \alpha_2 t)\}$$

where a_1 and a_2 are the modes position amplitudes, α_1 and α_1 the mode damping rates, and ω_1 and ω_2 the mode angular frequencies. Since the spectrum analyzer displays the amplitude as the

power in the spectral line at the center frequency vs. time, we must write the power as

$$\begin{aligned} &\textit{Power in } y(t) \propto \{Y(t)\, Y(t)^*\} \\ &\quad = a_1^2 \exp(-2\alpha_1 t) + a_2^2 \exp(-2\alpha_2 t) + 2a_1 a_2 \exp\{-(\alpha_1 + \alpha_2)\, t\} \cos \Delta\omega t \end{aligned}$$

where $\Delta\omega = \omega_1 - \omega_2$. Since we are interested particularly in the longest-lived oscillation, we will generally focus on the one mode of these two that has the longer damping time, i.e. the lower damping rate. So we will fit the drive-damp data to this two damped oscillator model and by convention assign $\alpha_1 < \alpha_2$ (unless the oscillation amplitude of the longer-lived mode is a very small contribution to the bunch's vertical displacement.) Plots of the damping rate will display results from the second fitting method, i.e. the value determined to be α_1.

1.3.3.1 Observations

We have made drive-damp measurements of positron beams under different conditions. They will be described here as the measurements of single bunches for the study of CESR's "baseline" stability and measurements of trains ob bunches to characterize the electron cloud effects.

Single Bunch Damping Rates To characterize the overall stability of CESR-TA we have measured the single bunch positron damping rates in a variety of different settings of the vertical feedback gain and the vertical chromaticity. These were studied in same optics at 2.08 GeV as were used for the 30 bunch train drive-damp measurements described below. Only a single operating parameter is varied as a part of each set of observations. All of the single bunch measurements were made at 0.75 mA.

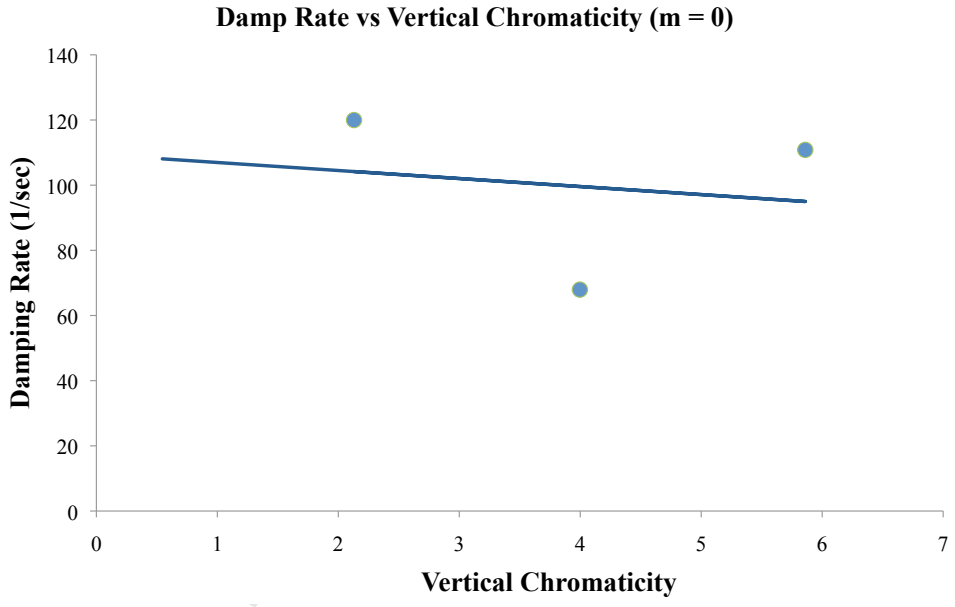

Figure 1.66: Single bunch damping rate for the vertical dipole mode vs. vertical chromaticity.

Single bunch damping rates were measured for the vertical dipole mode and both vertical head-tail modes. Figures 1.66, 1.67 and 1.68 display these damping rates as a function of the vertical

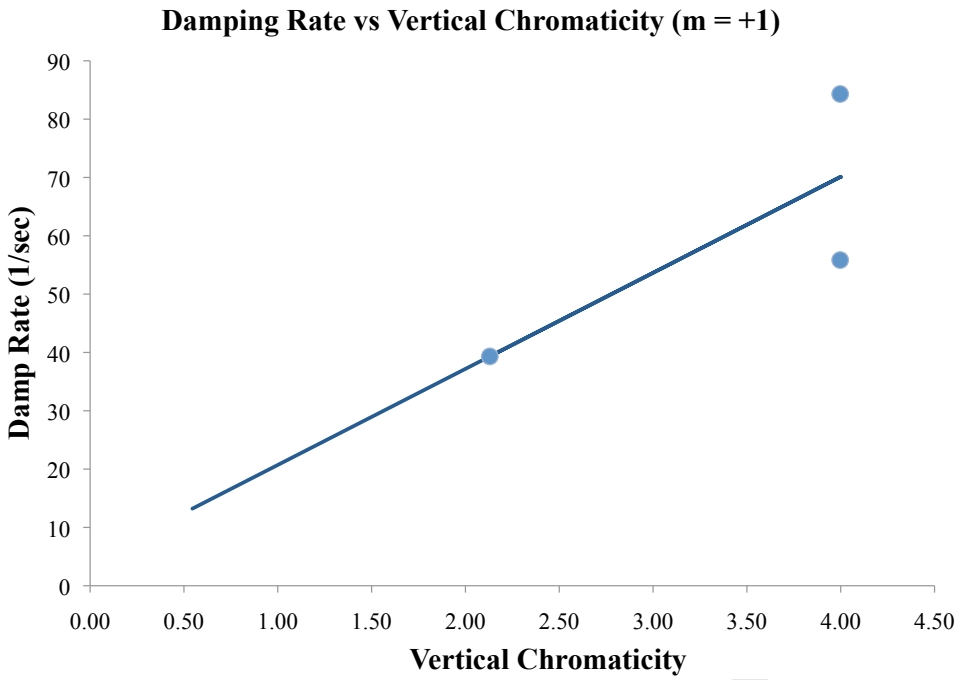

Figure 1.67: Single bunch damping rate for the vertical m = +1 head-tail mode vs. vertical chromaticity.

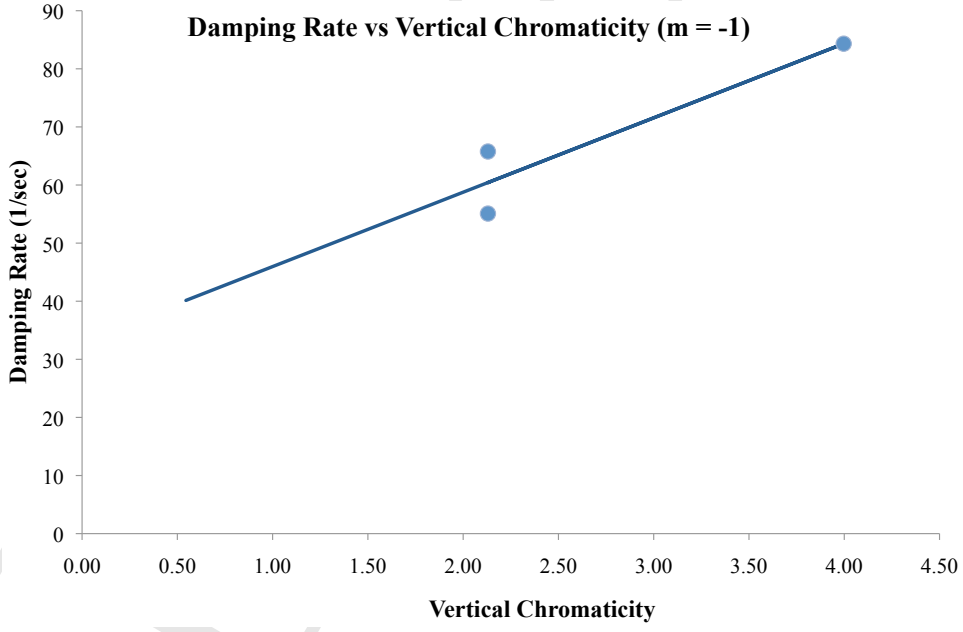

Figure 1.68: Single bunch damping rate for the vertical m = +1 head-tail mode vs. vertical chromaticity.

chromaticity (where the chromaticity is $Q = dQ/d\delta$, where δ is the fractional energy deviation.) The vertical feedback was turned off for these measurements. The figures also have a plot of the best linear fit to the measured data points. The results of the linear fits may generally be written

as

$$\alpha_v = \frac{\partial \alpha_v}{\partial I}\left(\frac{I_b}{1\ mA}\right) Q'_v + \alpha_{v0}$$

where the chromaticity contribution is expected to scale with current and the constant term is expected to be the radiation damping contribution. The linear fits for the three figures are

$$\alpha_v = \left[(-3 \pm 20)\left(\tfrac{I_b}{1\ mA}\right) Q'_v + 110 \pm 60\right] \sec^{-1} \qquad for\ m = 0\ mode$$

$$\alpha_v = \left[(21 \pm 18)\left(\tfrac{I_b}{1\ mA}\right) Q'_v + 4 \pm 46\right] \sec^{-1} \qquad for\ m = 1\ mode$$

$$\alpha_v = \left[(17 \pm 6.6)\left(\tfrac{I_b}{1\ mA}\right) Q'_v + 33 \pm 14\right] \sec^{-1} \qquad for\ m = -1\ mode$$

where there are uncertainties included for the fits with over-constrained data and where I_b is the current in the bunch. Within uncertainties the head-tail modes display a fairly similar dependence on the vertical chromaticity. Although this is not determined accurately, the zero chromaticity damping rate is consistent with the vertical radiation damping rate of 18 s^{-1}. In this first measurement for the dipole (m=0) mode gives a result, which is much less damping than is expected. This dependence will need to be re-measured at the next convenient time.

Measurements of the damping rates were made as a function of the 14 ns vertical dipole feedback system setting. Figures 1.69, 1.70 and 1.71 plot the vertical damping rates for the vertical dipole mode and both vertical head-tail modes, respectively. These measurements were undertaken with the vertical and horizontal chromaticities set to 2.13 and 0.58, respectively. The damping rates of the head-tail modes are a surprisingly stronger function of the vertical feedback than would be anticipated, while, as expected, the vertical dipole mode is a function of the feedback and all will be proportional to the current per bunch. The figures also contain the best linear fit to the observed data. The best linear fits for the three figures may be written as

$$\alpha_v = \left[Q'_v\,(-620 \pm 80)\left(\tfrac{I_b}{1\ mA}\right)\left(\tfrac{Fdbk\ Cmd}{1000}\right) + 130 \pm 42\right] \sec^{-1} \qquad for\ m = 0\ mode$$

$$\alpha_v = \left[Q'_v\,(-590)\left(\tfrac{I_b}{1\ mA}\right)\left(\tfrac{Fdbk\ Cmd}{1000}\right) + 39\right] \sec^{-1} \qquad for\ m = 1\ mode$$

$$\alpha_v = \left[Q'_v\,(-300 \pm 130)\left(\tfrac{I_b}{1\ mA}\right)\left(\tfrac{Fdbk\ Cmd}{1000}\right) + 80 \pm 57\right] \sec^{-1} \qquad for\ m = -1\ mode$$

where uncertainties for the fit values are given when the fits are over-constrained. The feedback off values for the damping rates are remarkably consistent with those calculated from the preceding fits for chromatic and radiation damping, with the values for the m = 0, +1, and -1 modes being 105, 38 and 60 s^{-1}, respectively. The damping rates due to feedback for the two head-tail modes are also reasonably consistent with being the same. These sets of results for the chromatic and feedback damping are necessary calibrations for the damping rates for trains of bunches presented next.

Figure 1.69: Single bunch damping rate for the vertical dipole (m = 0) mode vs. vertical dipole feedback.

Damping Rates for Trains of Bunches A series of drive-damp measurements were taken with 30 bunch trains in September and December of 2010 and June of 2011. We present here the data analyzed from the September 2010 and June 2011 runs. (The December 2010 run has an orphaned set of data, which is still being analyzed.) All of the data sets were taken at 2.08 GeV with 30 bunch trains of positrons. The earlier data sets (177 and 182) were taken with approximately 0.75 mA, while the later data sets (697, 699 and 700) had approximately 0.35 mA stored bunches. The lower current runs were undertaken to allow the electron cloud to build up more slowly through the train. The damped amplitudes for each bunch in these data sets have been fit to the two damped oscillator model. In some cases the fitting algorithm had difficulty converging on reasonable values. This can occur when 1) the bunchs oscillation signal level is too low, 2) the bunchs motion exhibits large oscillations after the initial motion has damped out, confusing the fitter, 3) the bunchs motion is unstable and the algorithm is attempting to fit undamped motion or 4) the fitter algorithm is not able to converge on a reasonable solution. The damping rates for these bunches are not plotted in the figures below, which display the damping rate vs. bunch number within the train.

For the first two of the data sets, we show the line power as a function of time, and bunch number. For data set 182 (Fig. 1.72), the $m = 0$ mode was excited and monitored. For data set 177

Figure 1.70: Single bunch damping rate for the vertical dipole (m = +1) mode vs. vertical dipole feedback.

(Fig. 1.73), the $m = -1$ mode was excited and monitored. The damped amplitudes for each bunch in these data sets are displayed for $m = 0$ mode (Fig. 1.74) and the $m = -1$ mode (Fig. 1.75).

In data set 182 (Fig. 1.72), we can see that the first bunch is more easily excited than the next few bunches, but the damping rates are similar. But further along the train, the excitation level increases and the damping time gets very long near the end of the train. In the damping rate plot (and Fig. 1.74) we observe that the beam stability is relatively constant through the train (with some reduction in stability in the neighborhood of bunches 8 through 12) and then generally decreases (damping rate decreases) as we proceed from bunch 21 onward. The fastest rates observed for the first bunches are consistent with what is expected from the feedback system, chromatic and radiation damping (approximately 200 s^{-1}.) Bunches after number 26 have amplitudes and damping rates consistent with unstable motion.

In data set 177, we see a similar trend, except that the first 20 bunches all appear to have similar damping times and excitation levels (with the notable exception of bunch 13, which does appear to have a much higher damping rate.) Again, further along the train, the excitation level increases and after bunch number 20 the damping time gets very long as we approach the end of the train.

Figure 1.71: Single bunch damping rate for the vertical dipole (m = -1) mode vs. vertical dipole feedback.

The fastest damping rates observed for the first 20 bunches are consistent with being somewhat less than what is expected from the feedback system, chromatic and radiation damping (approximately 110 s^{-1}.)

The next three data sets were also taken at 2.08 GeV with single 30-bunch trains of positrons, but in these cases the current per bunch was lowered to 0.35 mA to allow the instability to develop over a larger number of bunches in the train. The m = 0 (dipole) mode was excited for data set 700. While the m = -1 and +1 (head-tail) modes were driven for data sets 697 and 699, respectively. For the data set 697 the vertical and horizontal chromaticities were -0.20 and 0.73, respectively, while for data sets 699 and 700 the vertical and horizontal chromaticities were changed to -2.07 and 0.79, respectively. The vertical chromaticity in particular needed to be at these low values in order to produce unstable head-tail motion within the train. For these sets we operated with the Dimtel feedback system and the data-taking software gated off the vertical feedback for the bunch being measured.

The damping rate vs. bunch number plot (Fig. 1.76) for data set 700 indicates a slight increase in the damping rate for the first bunch; after the first bunch the next 17 or so bunches have damping rates that are similar. There are a few exceptional bunches (e.g. bunches 11 and 19) that appear to

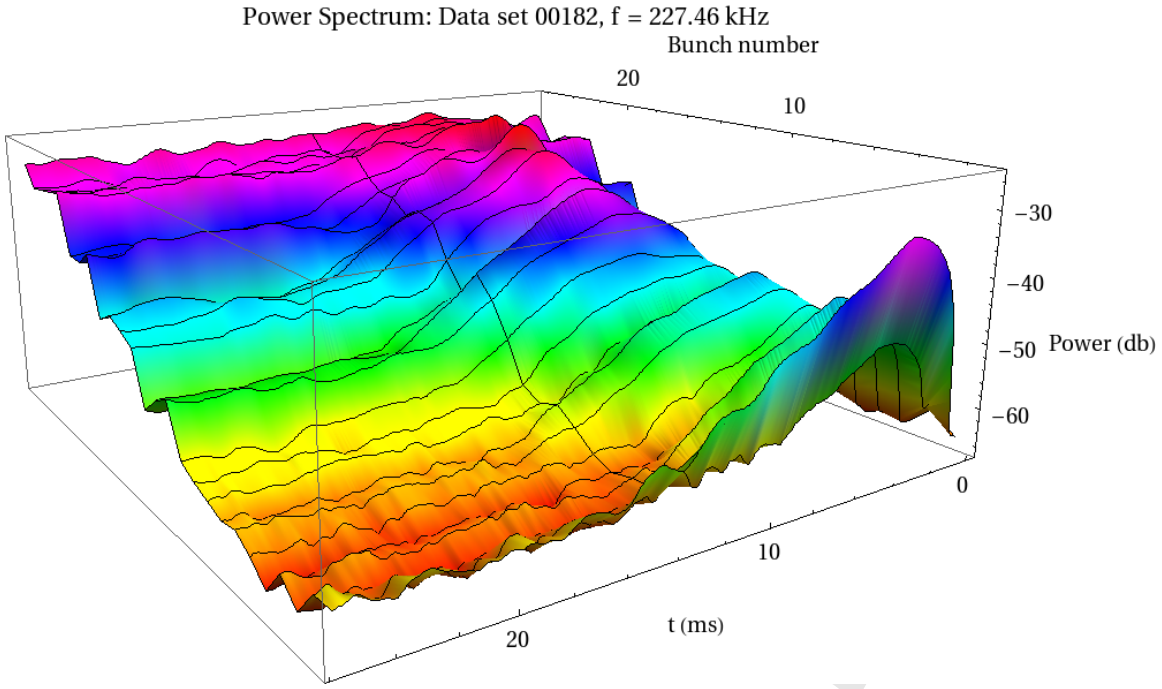

Figure 1.72: Data set 182: Grow-damp measurements for $m = 0$ mode. Chromaticity: (H,V) =(1.28,2.39). Bunch current = 0.72 mA

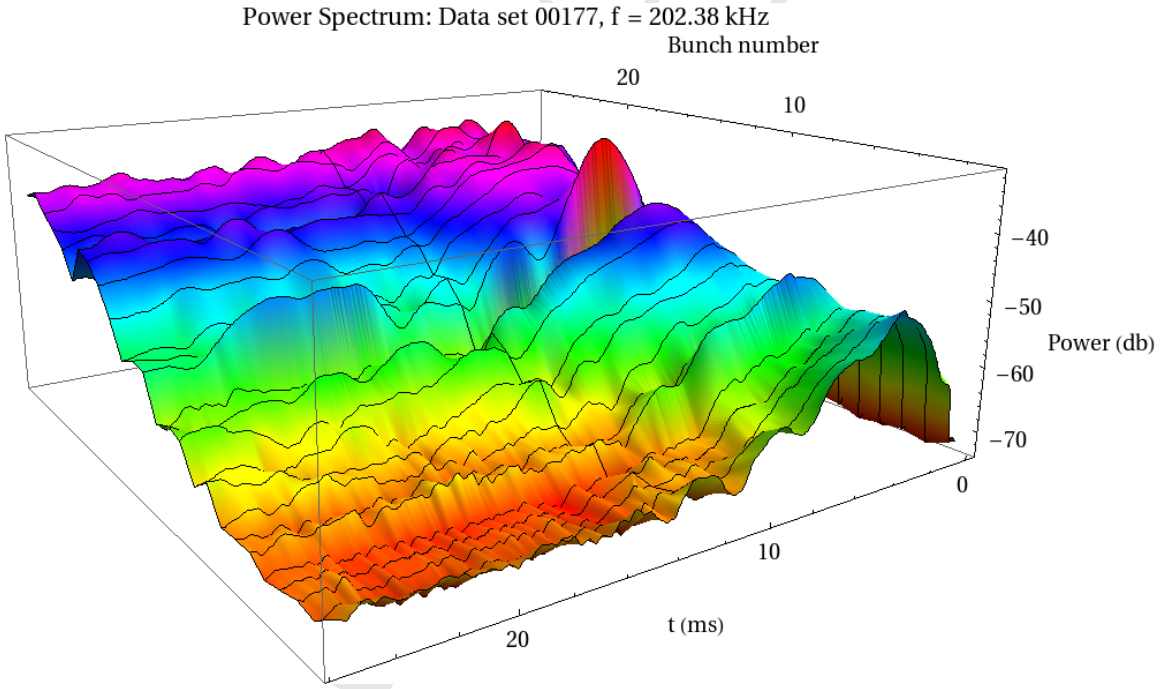

Figure 1.73: Data set 177: Grow-damp measurements for $m = -1$ mode. Chromaticity: (H,V) =(1.28,2.39). Bunch current = 0.75 mA

be less stable and even a bunch (number 8) that seems to have a much great damping rate than its neighbors. (There is some suspicion that the data acquisition softwares communications pathway,

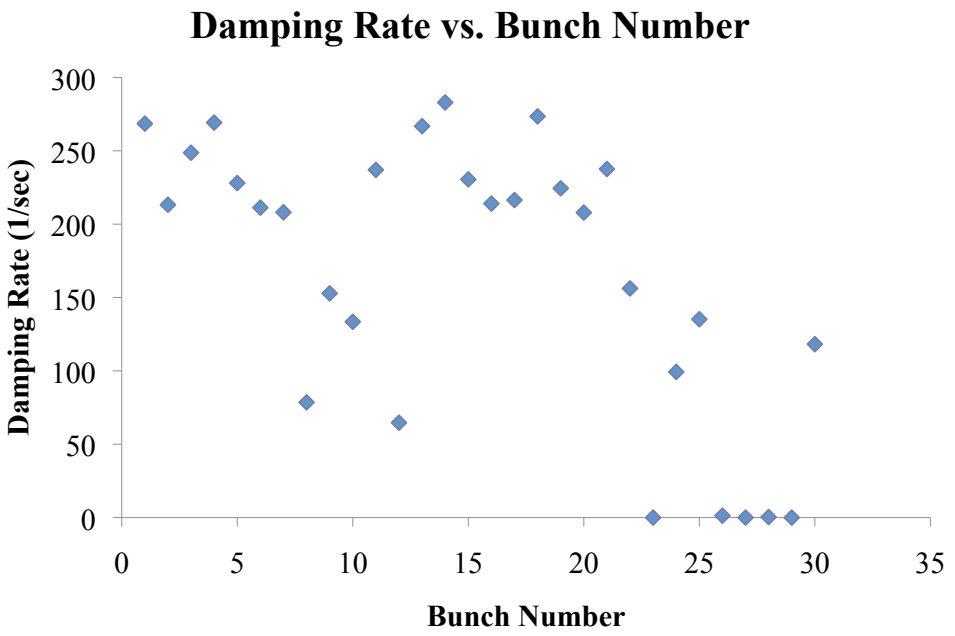

Figure 1.74: Damping rate for the vertical m = 0 dipole mode vs. the bunch number of a 30-bunch-long train of positrons. Data set 182. Chromaticity: (H, V) =(0.58, 2.13) and the vertical feedback setting is 20% of full scale with these giving an estimated damping rate of 200 s^{-1}. Bunch current = 0.72 mA.

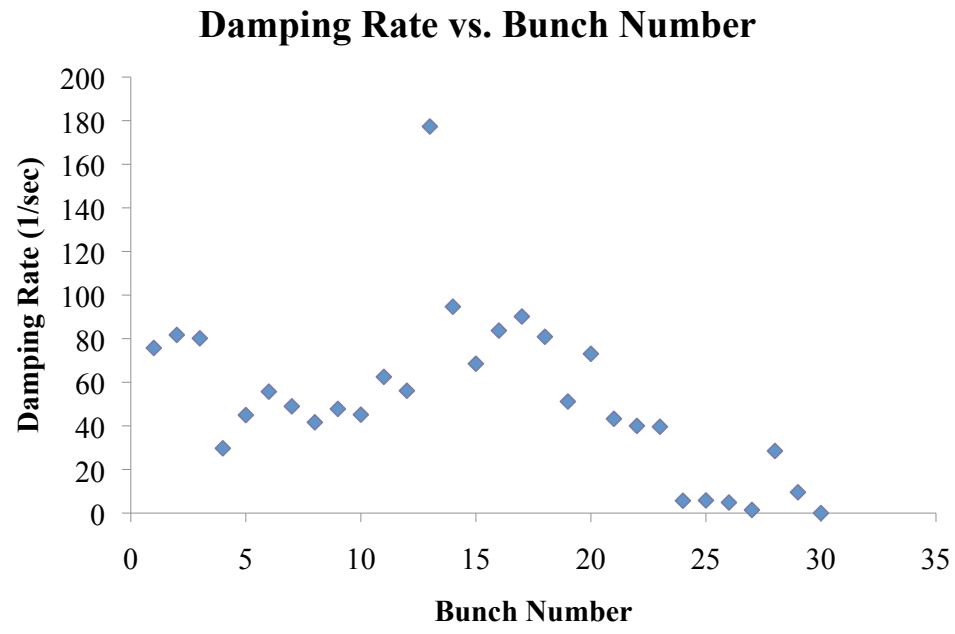

Figure 1.75: Damping rate for the vertical m = -1 head-tail mode vs. the bunch number of a 30-bunch-long train of positrons. Data set 177. Chromaticity: (H, V) =(0.58, 2.13) and the vertical feedback setting is 20% of full scale with these giving an estimated damping rate of 110 s^{-1}. Bunch current = 0.75 mA.

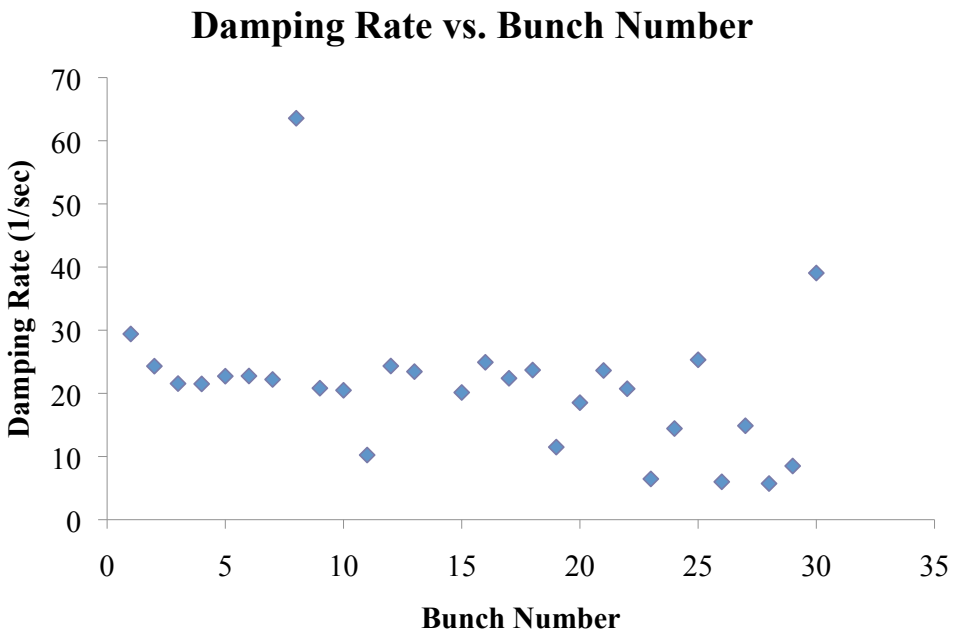

Figure 1.76: Damping rate for the vertical m = 0 dipole mode vs. the bunch number of a 30-bunch-long train of positrons. Data set 700. Chromaticity: (H, V) =(-2.07, 0.79) and the vertical Dimtel feedback is in operation, but is gated OFF for the bunch being measured. This gives an estimated damping rate of 110 s^{-1} for the measured bunch. Bunch current = 0.35 mA

needed to gate off the feedback for bunch 8, may have failed during this bunchs measurement.) The damping rate seems to fluctuate toward less stability as we approach the end of the train beginning at bunch 19. The damping rates observed for the first 18 bunches (approximately 20 s^{-1}) are much less than what is expected from the feedback system, chromatic and radiation damping (approximately 110 s^{-1}.)

As is typical for the observations of head-tail damping for the m = +1 mode (Fig. 1.77) and the m = -1 mode (Fig. 1.78) there tend to be larger fluctuations in the measured damping rates. The estimate of the combination of the chromatic and radiation damping rate for the m = +1 mode is approximately 20 s^{-1}. A similar estimate for the m = -1 mode is approximately 3 s^{-1} (consistent with zero.) In both cases we see a decrease of stability occurring in the range of bunch 16 to 25 within the accuracy of the present measurements. This is also the range of bunches, for which the dipole (m = 0) mode indicates larger fluctuations in stability from bunch to bunch. For the m = +1 mode the damping rate for the first third of the train is consistent with or slightly less than chromatic and radiation damping, while for the m = -1 mode the damping rate for the first third is also in neighborhood of the magnitude of chromatic and radiation damping, although the measured damping rates appear to be consistently slightly higher. The large fluctuations in damping, beginning around bunch 20 of the train, represent the fact that the fitting routine is becoming somewhat confused by the growth of a single unstable oscillation. This instability begins about 20 ms after the drive signal is turned off and the head-tail motion has damped, grows to a peak amplitude about 30 ms later and then damps in another 20 ms. For the last bunches in the train the peak amplitude in this unstable pulse can exceed the initial head-tail motion by a factor of three.

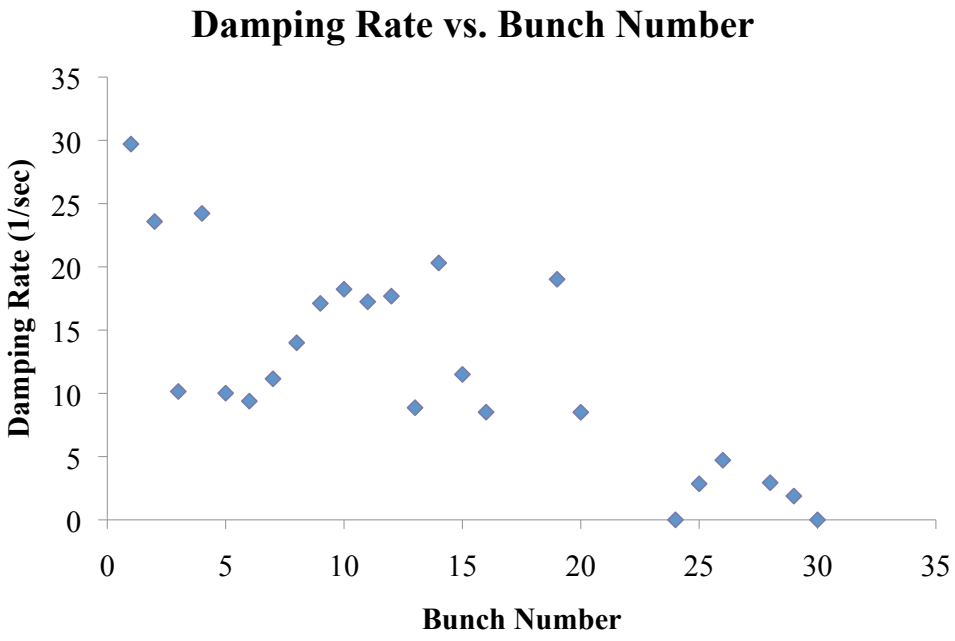

Figure 1.77: Damping rate for the vertical m = +1 head-tail mode vs. the bunch number of a 30-bunch-long train of positrons. Data set 699. Chromaticity: (H, V) =(-2.07, 0.79) and the and the vertical Dimtel feedback is in operation, but is gated OFF for the bunch being measured. This gives an estimated damping rate of 20 s^{-1} for the measured bunch. Bunch current = 0.35 mA.

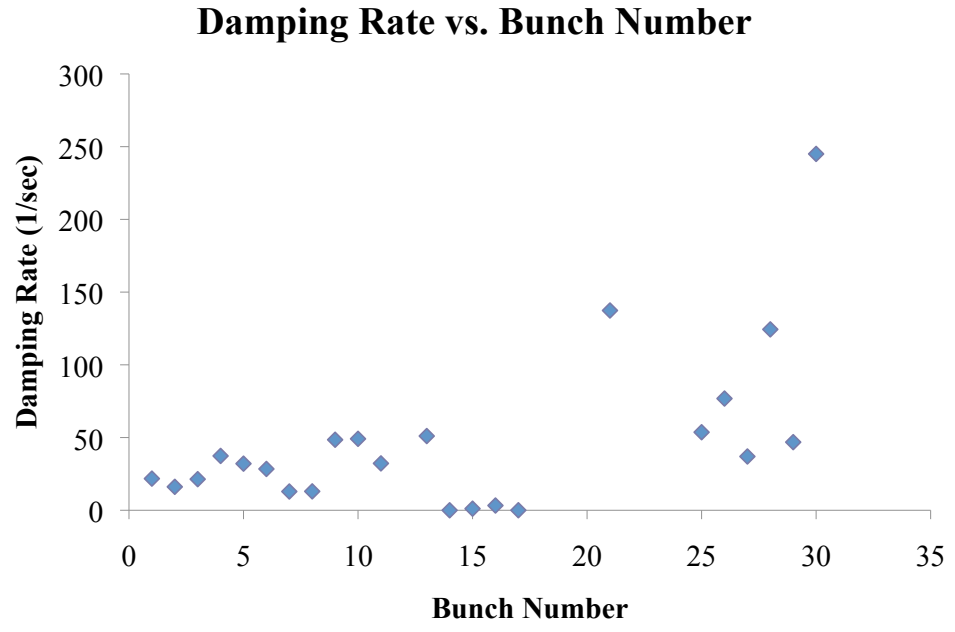

Figure 1.78: Damping rate for the vertical m = -1 head-tail mode vs. the bunch number of a 30-bunch-long train of positrons. Data set 697. Chromaticity: (H, V) =(-0.20, 0.73) and the vertical Dimtel feedback is in operation, but is gated OFF for the bunch being measured. This gives an estimated damping rate of roughly 3 s^{-1} for the measured bunch. Bunch current = 0.35 mA.

Conclusions from Drive-damp Measurements This technique is useful for studying stability of bunches within trains before the motion becomes unstable. In the conditions that we have studied, the damping rate for motion of bunches in the train lessens as the electron cloud builds up. The vertical dipole and head-tail modes become unstable at approximately the same bunch within the train, although the data is suggestive of the head-tail modes becoming unstable at a slightly earlier bunch than when the dipole mode destabilizes. The quality of the present data is not sufficient to specify whether the head-tail and dipole motion initially becomes unstable for the same bunch or not. However, what is clear is that motion of the bunches remain stable with essentially the same damping rates until it becomes unstable with a transition over relatively few bunches later in the train.

What can be said is that the effects of the electron cloud on the bunches within a train have both similarities to and differences from the dynamics typically observed for convention accelerator impedances. For a transverse cavity mode excited resonantly by a train of bunches, if the Q of this mode is low enough that the cavity field decays before the train returns, one would expect the energy contained in the interaction between the cavity mode and the beam is only carried forward from one turn to the next by the beam itself.

The part of the coherent interaction between the bunch and the electron cloud, which is similar to that of an RF cavity mode, is as follows. If all of the bunches within the train have transverse feedback applied except for the one, which is being observed, then the motion of this particular bunch will become unstable when the deflection from that the cavity mode grows (more rapidly than the mechanisms that damp the beam) as the amplitude of the bunchs displacement increases. This is true both for dipole and head-tail modes. Now for a conventional low-Q RF cavity transverse mode, the peak deflection is 90deg out of RF phase with the energy loss from the bunch that excites the mode. Thus for this transverse mode to deflect the bunch either 1) it must have a very large transverse impedance or 2) the time for its field to vary must be comparable to the temporal length of the bunch. A similar conclusion can be drawn for the effect of the electron cloud that has accumulated partway through the train. At this location there must be a rapid temporal variation in the clouds field in order to drive a bunch to become unstable, i.e. this must be a fairly high frequency phenomena.

However, the electron cloud has a characteristic, which is unlike a cavity deflecting modes interaction with the beam. If all bunches within the train are stabilized except one, then this bunch can feel a constant deflection from the accumulated RF fields from earlier bunches. This will cause a constant perturbation of the orbit, but will not inherently drive this bunch unstable. This implies that the strength of the instability will grow proportional to the current in this bunch, but will not matter where the bunch is within the train; all positions will be nearly equivalent. Since the electron cloud builds up along the train, the strength of the electron cloud-beam interaction grows along the train. This will cause unstable motion, which is not present for earlier bunches, to develop in later bunches in the train. These drive-damp measurements presented here support this view. Also, since the bunch, at which head-tail motion becomes unstable, is essentially the same bunch, at which dipole motion becomes unstable, this implies that the electron clouds interaction occurs over longitudinal distances less than the bunch length. This would allow the center and tail of the bunch to feel the transverse kick.

1.3.3.2 Future work

Future measurements are planned to repeat the single bunch damping rates vs. changes in the chromatic damping.

1.3.4 Emittance Growth Along Bunch Trains: Experimental Studies

1.3.4.1 Introduction

At CesrTA, bunch-by-bunch beam sizes are measured using an x-ray monitor (see Sec. **??**) built on the D Line of the CHESS light source for viewing positrons, as shown in Figure 1.79. (A similar line for viewing electrons is installed at the C Line.) The detector can read out bunch-by-bunch, turn-by-turn signals at 14 ns or 4 ns spacing. Three sets of x-ray optics can be selected in the optics box: Coded Aperture (CA), Fresnel Zone Plate (FZP) and an adjustable slit. The coded aperture mask permits single-shot, photon-statistic-limited resolutions of $\sim 2-3$ μm at beam sizes of 10-20 μm[30]. This section will discuss measurements made using these optics. Comparisons are made with similar observations at KEKB[31, 32] when appropriate.

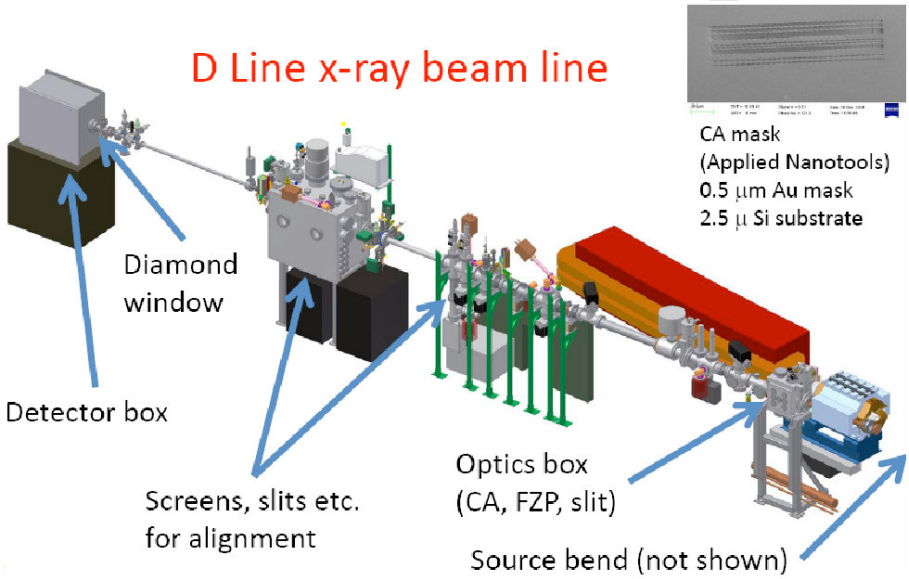

Figure 1.79: Layout of x-ray beam line for viewing positron beams at CesrTA.

1.3.4.2 Bunch current dependence

Initial data were taken with the bunches at 14 ns spacing, using 45-bunch trains. For each bunch, the turn-by-turn vertical sizes and positions were fitted, and then the sizes were averaged over all turns. For each bunch the rms of the positions were calculated represent the motion of the bunch. Figures 1.80, 1.81 and 1.82 show the bunch-by-bunch sizes and rms motions along the train at bunch currents of 0.5 mA, 1.0 mA and 1.3 mA, respectively. For the 1.0 and 1.3 mA/bunch cases, a slow growth can be seen starting at the beginning of the train, with the bunch size growing more rapidly after around bunch 25 for 1.0 mA, and around bunch 20 for 1.3 mA. This is consistent with

the cloud density increasing more rapidly along the train as bunch currents increase. As discussed above in Sec. 1.3.2.5, what appears to be a synchrotron-betatron sideband signal is present from all bunches from the fast blow-up threshold to the end of the train, perhaps indicating that incoherent emittance growth is seen below the threshold, and a coherent instability after that.

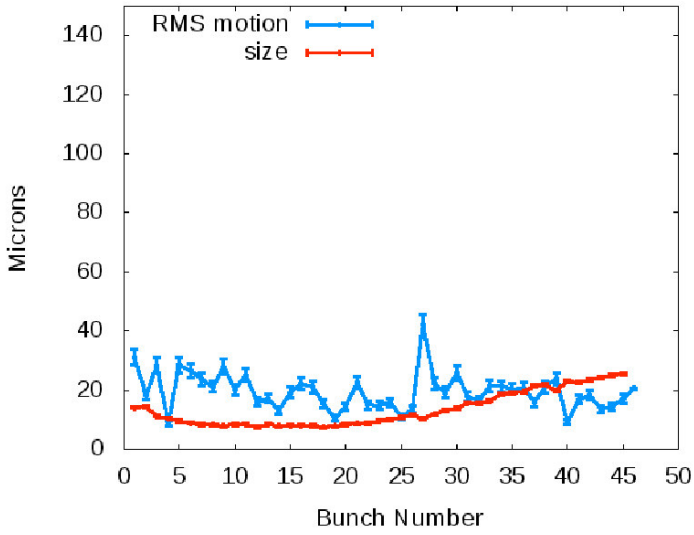

Figure 1.80: Bunch-by-bunch beam size and rms motion at 14 ns spacing with 0.5 mA/bunch (128 turns).

The head of the train was also seen to be somewhat enlarged. The cause of this is under investigation, but is believed to be possibly due to long-lived trapped electrons in the CesrTA ring which is dipole- and wiggler-dominated (unlike KEKB, where no such effect was evident), and/or possibly due to feedback tuning issues. The tail of the train is also seen to fall off gradually in size, an effect which was not observed at KEKB, where the beam size simply saturated going to the back of the train. The reason for this difference is not yet understood. It is worth mentioning that the bunch lifetimes followed roughly the measured beam sizes, with longer lifetimes for bunches with larger measured sizes, as might be expected from Touschek effect, which provides backing evidence that the sizes really do vary in the manner reported by the x-ray monitor.

Finally, Figure 1.83 shows the bunch-by-bunch position spectrum as measured by the x-ray monitor. The vertical tune line can be seen at the upper part of the plot, shifting downward in frequency (upward in tune units), due presumably to the electron cloud density increasing along the train.

1.3.4.3 Chromaticity change

At KEKB, the coherent instability threshold was found to change with the chromaticity, with higher chromaticities pushing the onset of the instability back along the train. At CesrTA, two sets of measurements were taken varying the chromaticity, one at 14 ns spacing and one at 4 ns spacing. Figure 1.84 shows the bunch-by-bunch size and rms motion for a vertical chromaticity of 1.2, and Figure 1.85 for a vertical chromaticity of 2.2. Here the transverse feedback gains were set very low (20% in vertical and horizontal directions, with longitudinal off), which is different from the cases

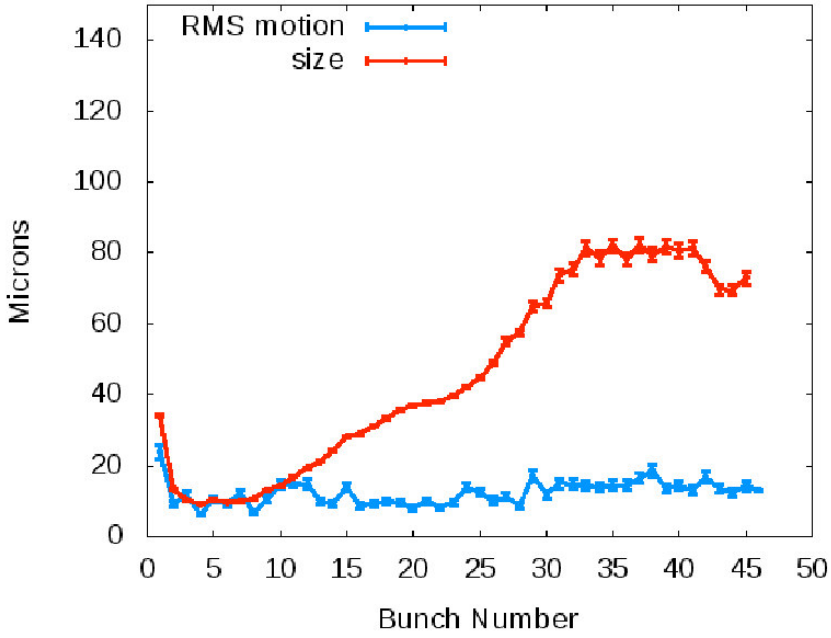

Figure 1.81: Bunch-by-bunch beam size and rms motion at 14 ns spacing with 1.0 mA/bunch (128 turns).

shown in the preceding section, where all feedback were at full normal gain settings, resulting in greater dipole oscillations towards the tail of the train. It can be seen that while raising the vertical chromaticity suppressed the dipole oscillations to some extent, the beam sizes along the train do not change, and neither does the blow-up threshold appreciably.

Figures 1.86 and 1.87 show the results at 4 ns spacing, for vertical chromaticities of ~ -0.8 and ~ -0.4, respectively. Again, the blow-up threshold is not seen to change noticeably. (The reason for the sudden drop off in bunch size at the end of the train is not clear, but may relate to the dipole oscillation becoming so large that much of the beam image is no longer contained on the detector, resulting in bad fits.)

It is also seen that the blow-up threshold does not change appreciably when changing from 14 ns spacing to 4 ns spacing. This may be due to the cloud lifetime being very long in the dipole-dominated CesrTA, and so does not decay appreciably over the space of 14 ns, making the cloud density a function of the number of preceding bunches. This is different from KEKB, where the instability threshold depends on the bunch spacing as well as the bunch currents.

The reason for the insensitivity to chromaticity change, in contrast to the case at KEKB, is not known, though it may be noted that the total chromaticity changes tried so far at CesrTA are smaller than those tried at KEKB (several units). It should also be mentioned that the sideband appearance threshold was observed to change with chromaticity, as shown above in Sec. 1.3.2.7.

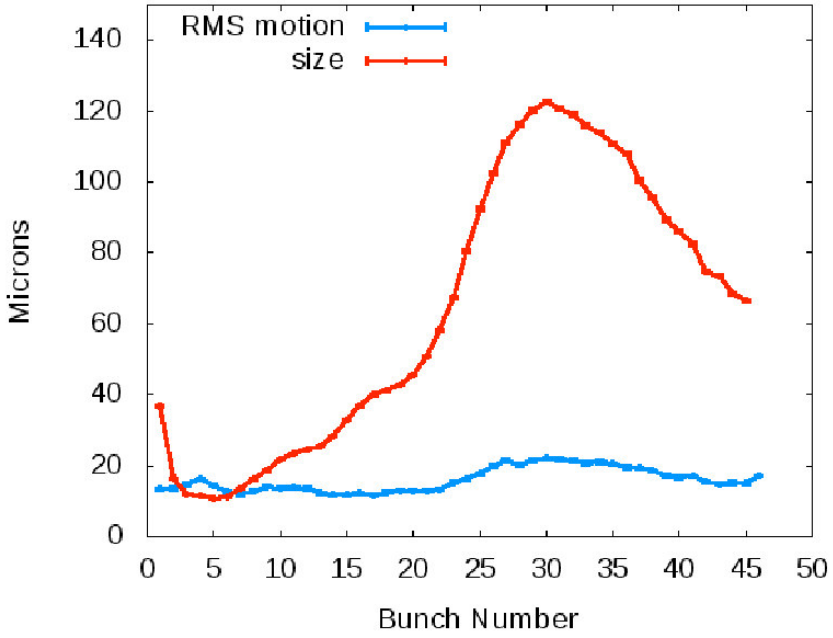

Figure 1.82: Bunch-by-bunch beam size and rms motion at 14 ns spacing with 1.3 mA/bunch (4096 turns).

1.3.4.4 Emittance variation

At KEKB, it was found that changing the initial beam size did not change the blow-up instability threshold. The initial beam size at CesrTA was also varied, using dispersion bumps through two wiggler sections in the L1 and L5 regions of the ring. The data for the enlarged-emittance beam, with an estimated smearing function of $\sim$ 30 μm (to be taken in quadrature with the natural beam size) are shown in Figure 1.88. This should be compared with the un-enlarged beam data of Figure 1.86. It can be seen that while the overall beam size is enlarged, the blow-up threshold is at the same location, around bunch 10. These data shown were taken at 4 ns spacing; similar results were found at 14 ns spacing.

The reason for the lack of dependence of the threshold on the beam size can be seen from Eq. 1.39. The phase factor χ is 8.9 for CesrTA (see Tab. 1.6), which is larger than the numerically estimated natural $Q \sim 7$ for a coasting beam[9]. In this case, the threshold is independent of vertical beam size.

Eq. 1.39 only applies at zero chromaticity. At non-zero chromaticity, there is an additional dependence of the threshold on the beam size. Typically for these measurements, CesrTA was operated with a relatively small vertical chromaticity. However, it is possible that measurements at much larger vertical chromaticities would show a dependence of the blow-up threshold on initial beam size.

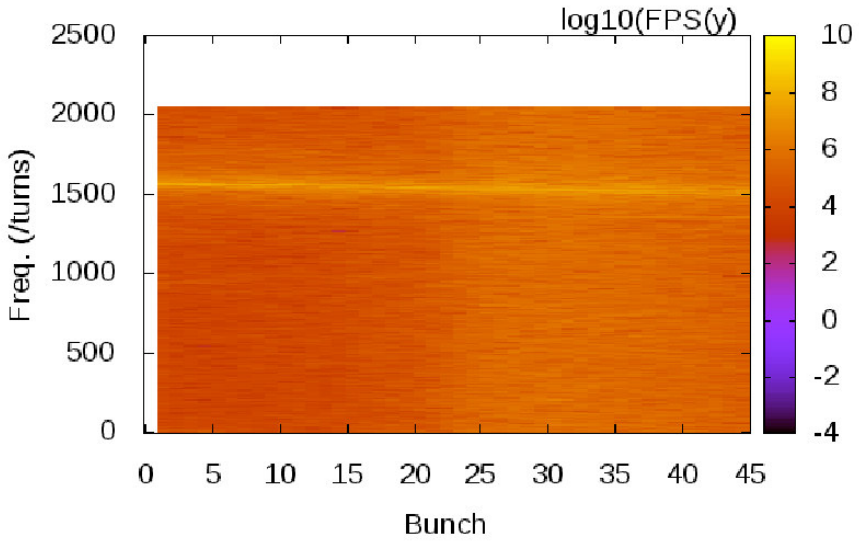

Figure 1.83: Fourier power spectrum of beam position measured by x-ray monitor at 14 ns spacing with 1.3 mA/bunch (4096 turns).

1.3.4.5 Feedback gain change

Finally, it was observed that the transverse bunch-by-bunch feedback had no effect on the coherent instability signal at KEKB [31]. Figures 1.89 and 1.90 show two different setting of the transverse feedback gain at CesrTA : 20% and 40% gain settings respectively, for both vertical and horizontal feedback. While the dipole motion behaviour changes somewhat with the change in gains, the blow-up behaviour is not changed at all, consistent with results seen at KEKB.

1.3.5 Instability threshold and emittance growth: Comparison with simulations

1.3.5.1 Analytical Estimates

Using the formulae presented in Sec. 1.2.2, Table 1.6 gives the key instability parameters for CesrTA at 2.1 and 4 GeV, based on the parameters given in Tables 1.4 and 1.4. At 2.1 GeV, the analytical estimate of a threshold density of 1.3×10^{12} m^{-3} is about 60% higher than the measured threshold of 8×10^{11} m^{-3} presented in Sec. 1.3.2.5. At 4 GeV, the estimate of a threshold density of 2.65×10^{12} m^{-3} is about 30% higher than the measured threshold of 2×10^{12} m^{-3} presented in Sec. 1.3.2.13.

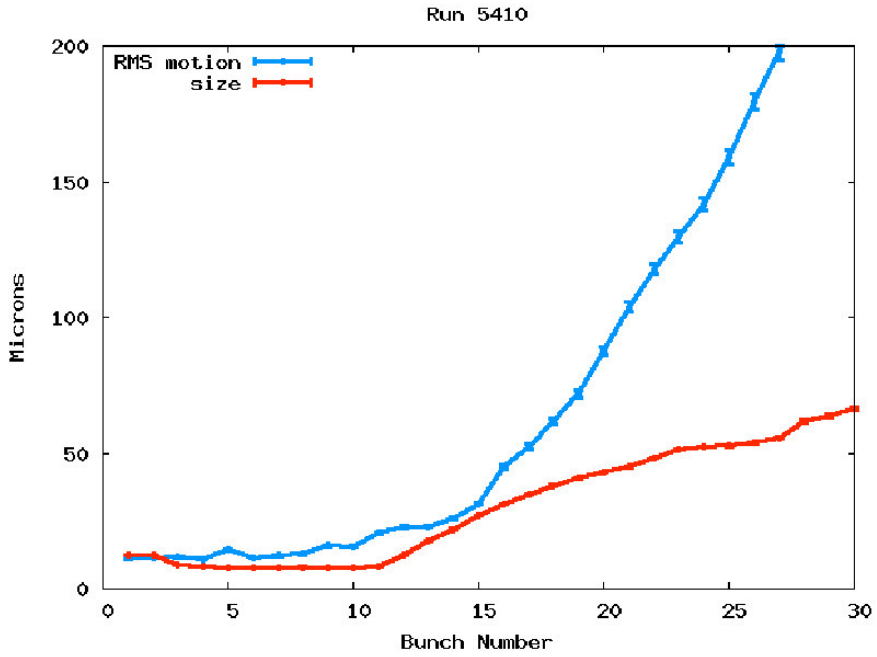

Figure 1.84: Bunch-by-bunch beam size and rms motion at 14 ns spacing, 0.75 mA/bunch, vertical chromaticity ~ 1.2.

Table 1.6: Analytical estimates of CesrTA EC instability thresholds

	CesrTA: 2.1 GeV	CesrTA: 4 GeV
Circumference L (m)	768	768
Energy E (GeV)	2.1	4.0
Bunch population N_+ ($\times 10^{10}$)	2	2
Emittance ε_x (nm)	2.6	40
Momentum compaction α ($\times 10^{-4}$)	68.0	63.0
Rms bunch length σ_z (mm)	10.5	17.2
Rms energy spread σ_E/E ($\times 10^{-3}$)	0.81	0.93
Horizontal betatron tune ν_x	14.57	14.57
Vertical betatron tune ν_y	9.62	9.62
Synchrotron tune ν_s	0.065	0.041
Damping time $\tau_{x,y}$ (ms)	56.4	19.5
Average vertical beta function β_y (m)	16	16
Electron frequency $\omega_e/2\pi$ (GHz)	43	11.3
Phase angle χ	9.5	4.1
Threshold density $\rho_{e,th}$ ($\times 10^{12}$ m^{-3})	1.3	2.65
Tune shift at threshold $\Delta\nu_{x+y}$ ($\times 10^{-3}$)	10.7	11.6

1.3.5.2 PEHTS simulations (adapted from [1])

Single-bunch instability Particle-in-cell simulations for the beam-electron-cloud interaction, using the PEHTS code [2], were executed to evaluate the threshold of the single-bunch instability. The machine parameters were taken to be those in Table 1.7.

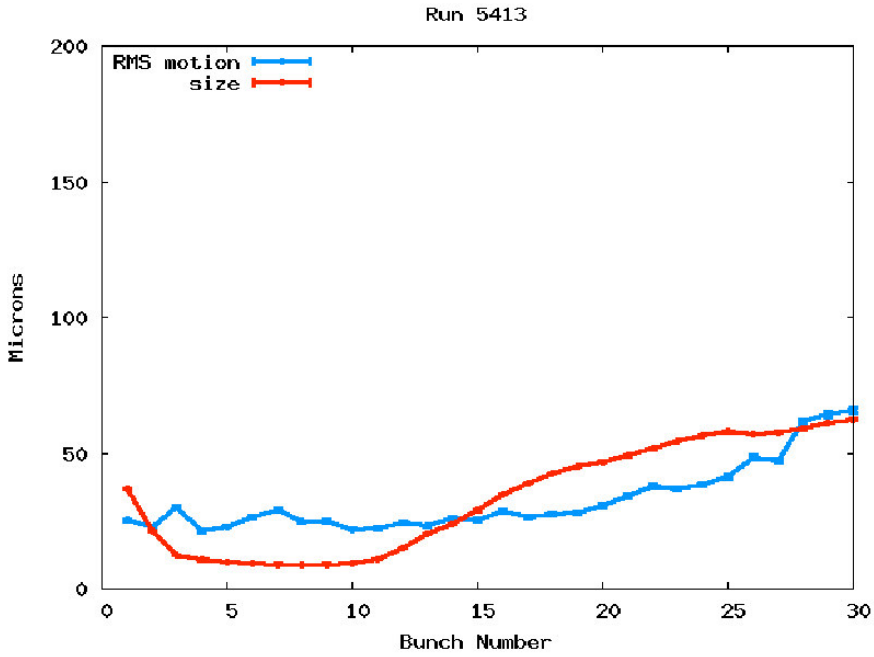

Figure 1.85: Bunch-by-bunch beam size and rms motion at 14 ns spacing, 0.75 mA/bunch, vertical chromaticity ~ 2.2.

Table 1.7: Parameters of CesrTA used for PEHTS simulations

	CesrTA/2	CesrTA/5
Circumference L (m)	768	768
Energy E (GeV)	2.1	5.0
Bunch population N_+ ($\times 10^{10}$)	2	2
Emittance ε_x (nm)	2.6	40
Momentum compaction α ($\times 10^{-4}$)	67.6	62.0
Rms bunch length σ_z (mm)	12.2	15.7
Rms energy spread σ_E/E ($\times 10^{-3}$)	0.80	0.94
Horizontal betatron tune ν_x	14.57	14.57
Vertical betatron tune ν_y	9.62	9.62
Synchrotron tune ν_s	0.055	0.0454
Damping time $\tau_{x,y}$ (ms)	56.4	19.5
Average vertical beta function β_y (m)	20	20
Electron frequency $\omega_e/2\pi$ (GHz)	35	11
Phase angle χ	8.9	3.7

In these simulations, a bunch and an electron cloud are represented by numerous macro-particles, 400,000 and 100,000 for the bunch and electron cloud, respectively. The bunch, which is sliced into 40 pieces along the rms bunch length σ_z, interacts with electrons distributed on the two dimensional $x - y$ plane. Each slice contains approximately 10,000 macro-beam particles.

One interaction between the bunch and electron cloud is treated as 40 interactions between slices and the electron cloud. The number of bunch slices can be significant for a low emittance beam;

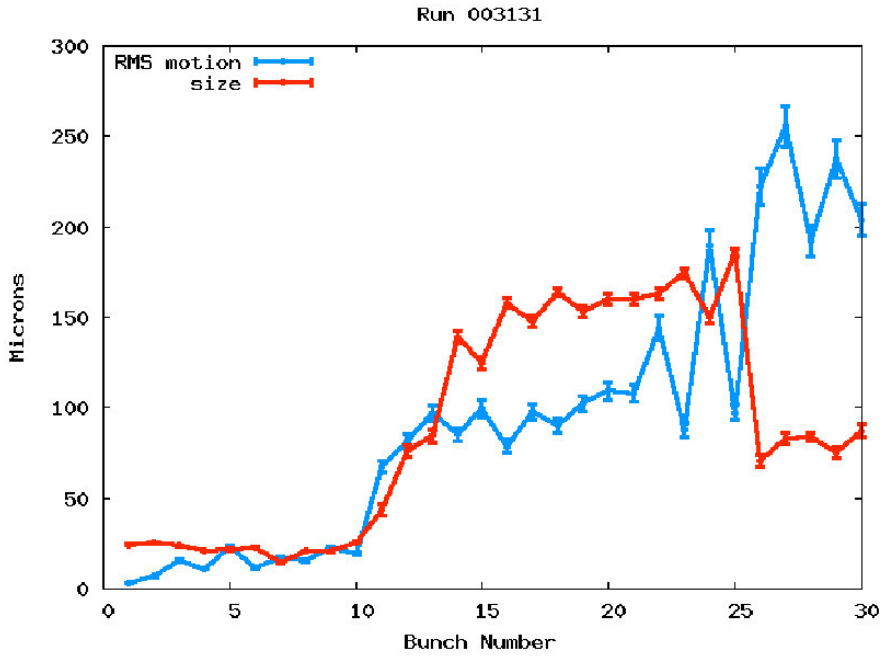

Figure 1.86: Bunch-by-bunch beam size and rms motion at 4 ns spacing, 0.75 mA/bunch, vertical chromaticity ~ -0.8.

therefore the number of slices is chosen to be larger than $\omega_{e,y}\sigma_z/c$ to represent the oscillation of electrons correctly. For this reason, the number of slices, 40, is enough but we checked for the larger number of bunch slices, 100, while maintaining the number of macro-particles of each slice. The result did not change, thus the number of bunch slices, 40, is sufficient to investigate the single-bunch instability in these simulations.

Particles in the bunch are tracked every integration step L/n_{step}; that is, electrons are assumed to be located at n_{step} positions in the ring. The electron cloud, which consists of 100,000 macro-particles, is initialized every interaction of the bunch, just before the interaction with the first slice. We characterize the horizontal and vertical cloud sizes as (Σ_x, Σ_y) in units of beam sizes (σ_x, σ_y). In these simulations, we set the cloud sizes to be (10,20). We compared the results with different cloud sizes, and obtained consistent results for cloud sizes larger than (10,20).

The fast head-tail instability is independent of the integration step if the number of steps in a synchrotron period is sufficient. The number of integration steps is typically chosen as 8 per one revolution as a simple model; that is, 160 steps for one synchrotron period, because $\nu_s = 0.05$ in CesrTA. When the tune shift and tune spread of the beam are large in a single interaction, an artificial incoherent emittance growth may arise. To avoid this emittance growth, the number of steps is chosen to be larger than one. The integration step may induce structure resonance peaks in the frequency spectrum; therefore, simulations with different numbers of steps should be done. We used an integration step number of 10, as a comparison.

The simulation calculates the transverse distribution of every bunch slice and electron interacting with them. Figure 1.91 shows a typical result of vertical position and the size of every bunch slice and the vertical position of electrons interacting with the slices above the threshold. Figures 1.91 (a) and 1.91 (b) are given for 2 and 5 GeV cases of CesrTA. Coherent motions of the beam and cloud

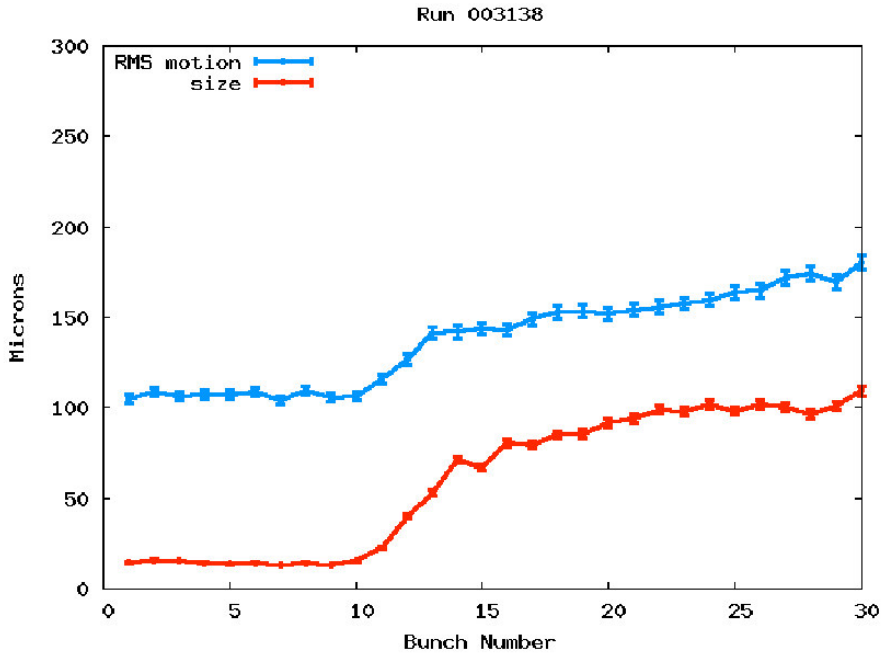

Figure 1.87: Bunch-by-bunch beam size and rms motion at 4 ns spacing, 0.75 mA/bunch, vertical chromaticity ~ -0.4.

are seen. The beam size increases due to the smear of the coherent motion. The longitudinal structure of the bunch for CesrTA/2 is more complex than that of CesrTA/5 due to the high phase factor χ.

The simulation is done for several cloud densities to estimate the threshold. Fig. 1.92 shows the evolution of the beam size of all particles in a bunch. The beam size is given by the projected distribution of all slices. The threshold is determined by whether the rapid increase of beam size is seen as shown in Fig. 1.92 and the increase is related to the coherent motion as shown in Fig. 1.91.

The instability threshold cloud densities are about 0.6×10^{12} and 4.0×10^{12} m^{-3} for 2 and 5 GeV cases, respectively. These values agree with the analytical estimates values shown in Table 1.6 within an average factor of 0.8. In the 2 GeV case, the threshold density agrees with the experimental of 8×10^{11} m^{-3} presented in Sec. 1.3.2.5. within a factor of 0.75.

Above the threshold densities, the coherent motion shown in Fig. 1.91 is seen clearly. For smaller cloud sizes, (10,10), the thresholds are 1.2×10^{12} and 3.0×10^{12} m^{-3}. But the thresholds are consistent with the value of (10,20) for larger cloud sizes (20,40) and (40,80).

A slow growth of the beam size is seen below the threshold in both cases. During the slow growth, any coherent motions as shown in Fig. 1.91 are not seen. The slow growth is caused by an artificial incoherent effect, which is due to the integration with 8 steps for one revolution. Unphysical structure resonances related to $a\nu_x + b\nu_y = 8n$ are induced. Precise estimation of the incoherent emittance growth is discussed later.

The single-bunch instability causes emittance growth above a threshold condition. The essence of the emittance growth is coherent head-tail motion. Direct evidence for the instability has been

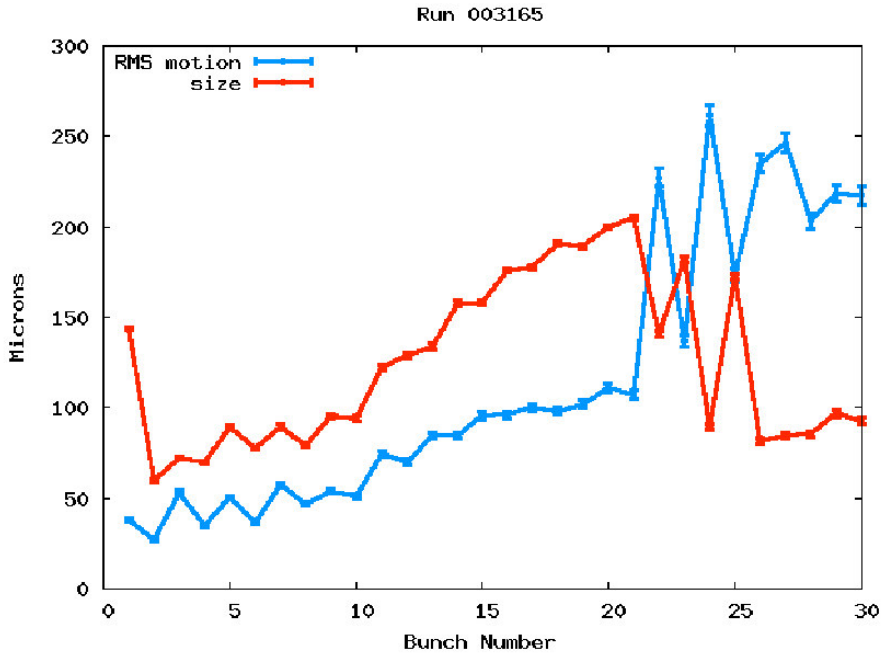

Figure 1.88: Bunch-by-bunch beam size and rms motion at 4 ns spacing with 0.75 mA/bunch, and increased base emittance. (Compare to low-emittance case in Fig. 1.86).

given by the observation of the synchrobetatron mode of a bunch, both in simulations and in measurements (using a bunch-by-bunch position monitor) at KEKB [33].

The synchrobetatron signal is obtained from the simulation by taking the Fourier transformation of the dipole position turn-by-turn. Figure 1.93 shows the Fourier spectra for the dipole moment of the beam above and below the threshold. The spectra for 2 and 5 GeV cases are very different. Clear dipole mode and lower synchrotron sideband are seen in 2 GeV case. The lower synchrotron sideband also appears in the experimental observations discussed in Sec. 1.3.2. Both mode signals are enhanced above the threshold in 2 GeV case. In 5 GeV case, several additional modes appear, and the dipole mode splits into two modes above the threshold. And a sideband appears at around $\nu_\beta + 0.07$ (above the dipole mode) above the threshold. The appearance of this higher frequency sideband above threshold is similar to the synchrobetatron sideband observed at the KEKB LER [31, 34].

Mode coupling may be considered as a mechanism for generating the instability and resulting emittance growth. Figure 1.94 shows the visible modes as a function of the cloud density for different cloud sizes (10,10) and (10,20) in 2 and 5 GeV cases. The mode spectra for a different integration step number, 10, are depicted to distinguish the unphysical structure resonances. The mode frequencies are almost the same for both integration steps. For the 2 GeV case, a sideband at lower frequency is seen for both cloud sizes. The tune shift evaluated by eq. (15) is not seen when the electron-cloud density increases in the 2 GeV case, but the vertical betatron tune shift is coincident with the tune shift evaluated by eq. (15) for the 5 GeV case. But, in the 2 GeV case, the tune shift is more complex because of high phase factor, χ.

For the 5 GeV case, the vertical betatron peak splits into two frequencies above the threshold, and the sideband at a higher frequency is induced in both cases (10,10) and (10,20). A similar spectrum

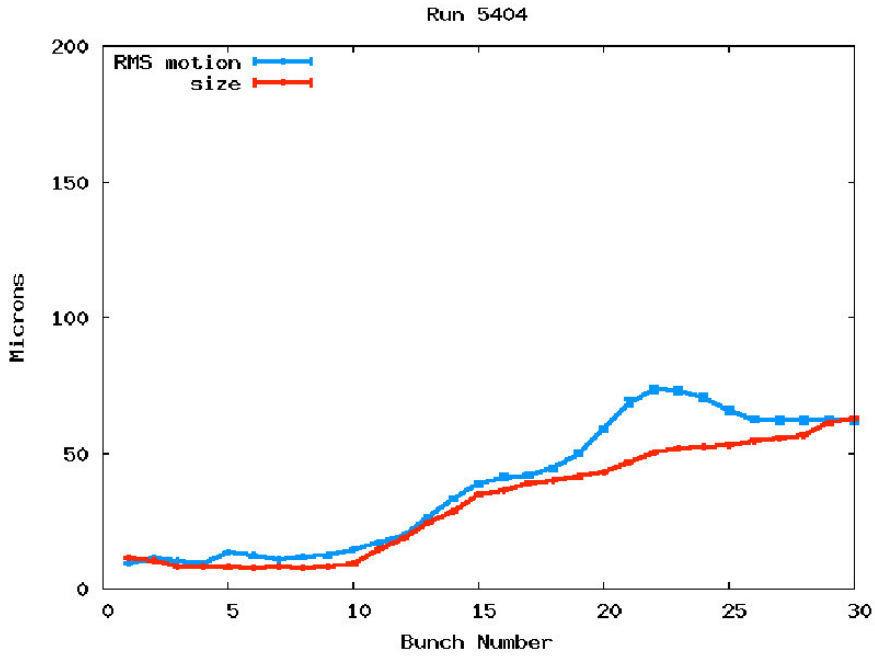

Figure 1.89: Bunch-by-bunch beam size and rms motion at 14 ns spacing with 0.75 mA/bunch, LOW feedback gain.

appears at a larger cloud size (20,40). For cloud sizes larger than (10,20), the threshold density of the electron cloud saturates, but the mode frequencies do not differ greatly from the cloud sizes (10,10) and (10,20) for the 2 and 5 GeV cases. It is difficult to conclude which modes are merged at the threshold density in the figures.

Feedback effect For a single-bunch instability, dipole motion is usually dominant above the threshold density. Therefore, we investigate the effect of a dipole feedback system on the electron-cloud instability. Figure 1.95 shows the amplitude of vertical dipole motion with and without the feedback, and the growth of beam size with the feedback on, in the 2 GeV case. The feedback-damping time is 50 turns. Dipole motion is dominant as shown in Fig. 1.95(a). The bunch-by-bunch feedback system kicks the beam based on an observation of the amplitude of dipole motion. The transverse kick received by the feedback can be expressed by

$$\mathbf{y}_{n,+} = \mathbf{y}_{n,-} - k\mathbf{M} < \mathbf{y}_{n-1,+} >, \tag{1.59}$$

where $\mathbf{y}$ is the vector consisting of the vertical coordinate of each macro-particle in the bunch and its derivative in time, (y, y'), n means the n-th turn, $+$ $(-)$ means the time after (before) feedback kick, k is the feedback-damping factor, $\mathbf{M}$ is the revolution matrix, and $< \mathbf{y}_{n-1,+} >$ is the averaged value of $\mathbf{y}_{n-1,+}$ measured by using two position monitors. The system feeds back the vertical oscillation with a one turn delay. In Fig. 1.95(b), the amplitude of dipole motion decreases significantly with the feedback system. The threshold density increases to 0.8×10^{12} m^{-3} as shown in Fig. 1.95(c). The feedback reduces the amplitude of dipole motion, and the threshold density increases to some extent. However the threshold is not improved with a stronger feedback-damping factor. Therefore the feedback system does not entirely suppress emittance growth in the 2 GeV case.

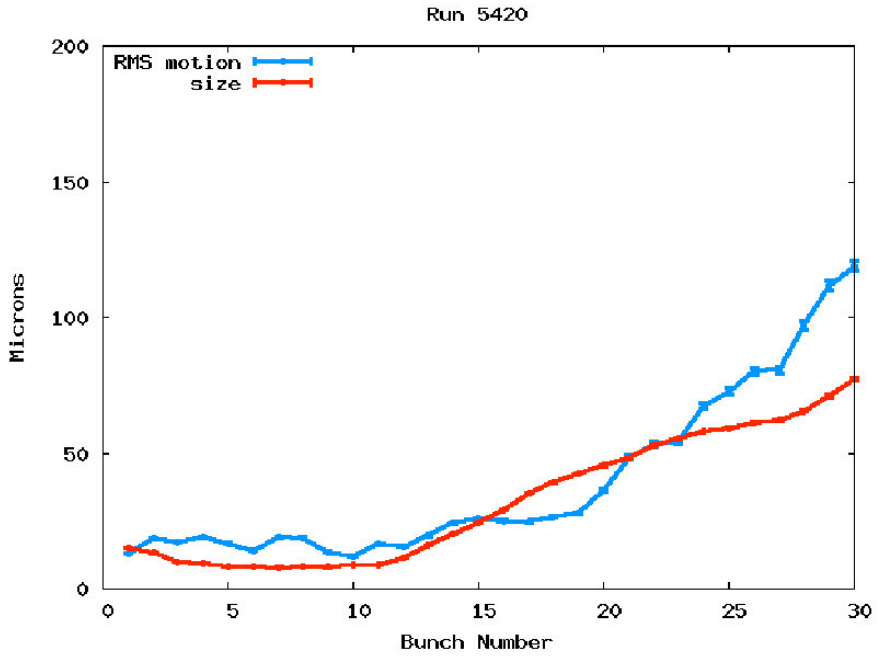

Figure 1.90: Bunch-by-bunch beam size and rms motion at 14 ns spacing with 0.75 mA/bunch, HIGH feedback gain.

Figure 1.96 shows the Fourier spectrum with the feedback on for the 2 GeV case. The feedback system is not effective in reducing the lower sideband peak. Several small sideband peaks appear at frequencies above that of the dipole mode. The spectrum is similar to that of the 5 GeV case, as shown in Fig. 1.93(b).

Figure 1.97(a) shows the evolution of the beam size with the feedback in the 5 GeV case. The feedback-damping time is 50 turns. The amplitude of the beam size and the threshold density do not change significantly with the feedback system on. Figure 1.97(b) shows the dipole motion without and with the feedback system at the threshold density, 4.0×10^{12} m^{-3}. The lower order head-tail instability which does not couple to the dipole mode is dominant because of lower $\omega_{e,y}\sigma_z/c$, but the dipole instability is not serious at the threshold density in 5 GeV case. The amplitude of dipole motion does not change significantly with the feedback system. For a stronger feedback-damping factor, the threshold density does not change as the 2 GeV case. Therefore, the feedback system does not suppress emittance growth in the 5 GeV case.

Dispersion effect Dispersion affects the electron-cloud instability because the electrons in the horizontal plane oscillate with different frequencies depending on their horizontal coordinate[35]. Figure 1.98 shows the beam size evolution in the presence of dispersion. The dispersion is assumed to be 0.8 and 0.7 m, which are averaged values for the realistic lattices of CesrTA 2 and 5 GeV shown in Fig. 1.99. The threshold is clearly degraded for 2 GeV case: $\rho_{e,th} = 0.1 \times 10^{12}$ m^{-3} from 0.6×10^{12} m^{-3}. The degradation is also visible in 5 GeV case, though it is smaller than the 2 GeV case: the threshold decreases from 4.0×10^{12} to 3.0×10^{12} m^{-3}. The difference between the 2 and 5 GeV cases seems to be due to the difference in the phase factor.

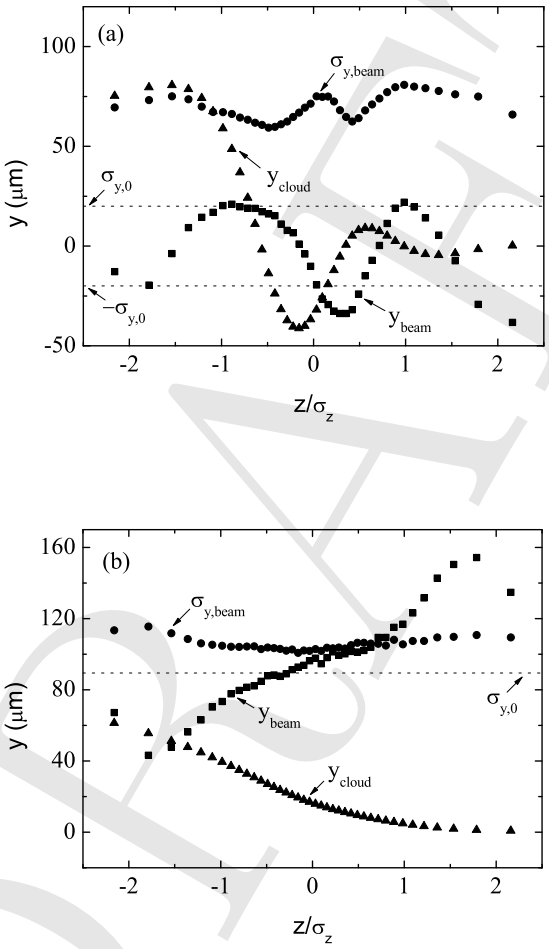

Figure 1.91: The vertical position and size of the bunch slices and the vertical position of electrons interacting with the slices above the threshold are depicted for (a) 2 and (b) 5 GeV cases. The dotted lines indicate the initial vertical beam sizes.

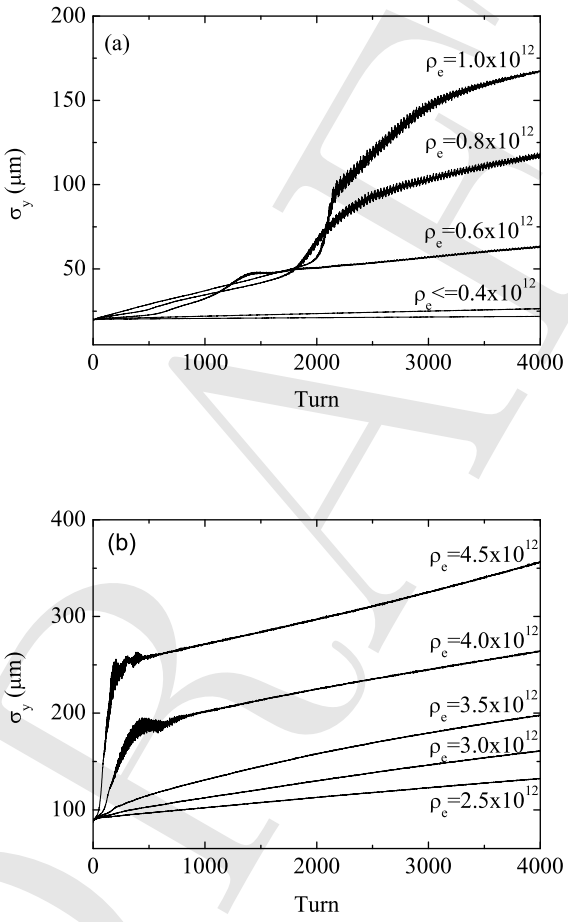

Figure 1.92: Evolution of vertical beam size growth for various cloud densities in CesrTA (a) 2 and (b) 5 GeV cases

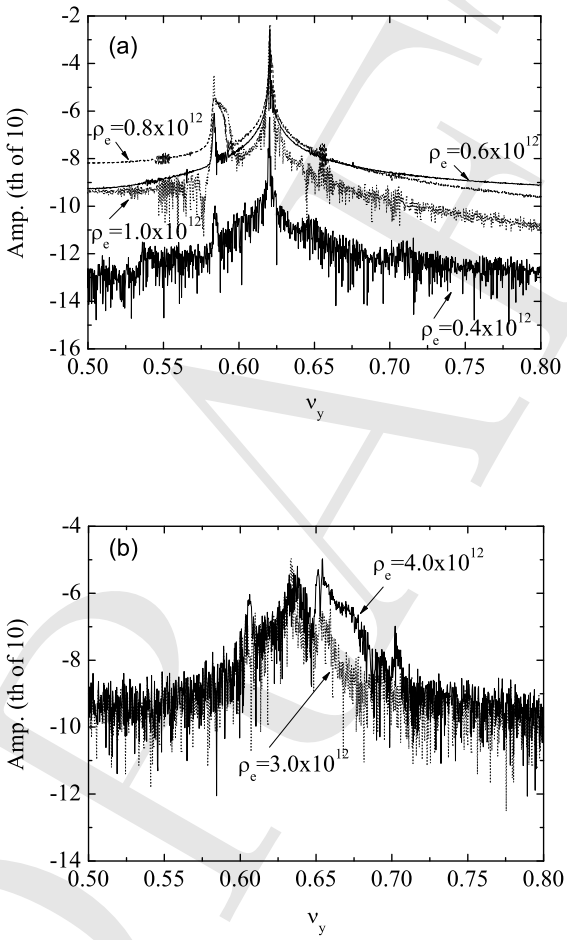

Figure 1.93: Frequency spectra for the dipole moments of (a) 2 and (b) 5 GeV cases. Vertical axis indicates the amplitude of frequency spectra and the index corresponds to the power of 10.

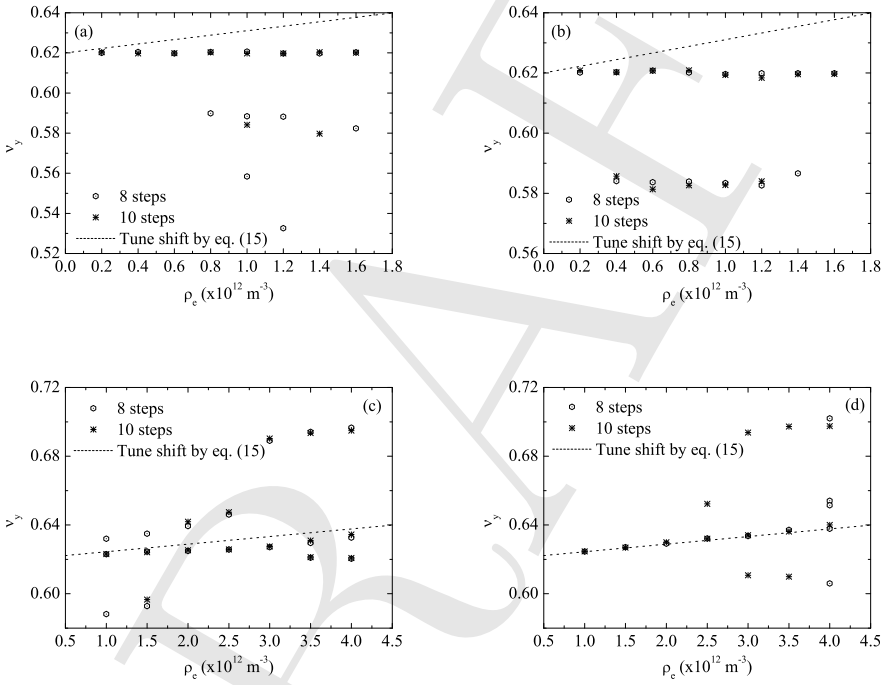

Figure 1.94: Mode frequencies for various cloud densities at different cloud sizes (10,10) and (10,20): (a) cloud size (10,10) for 2 GeV, (b) (10,20) for 2 GeV, (c) (10,10) for 5 GeV, and (d) (10,20) for 5 GeV cases, respectively. The dotted line indicates the tune shift evaluated by eq. (15).

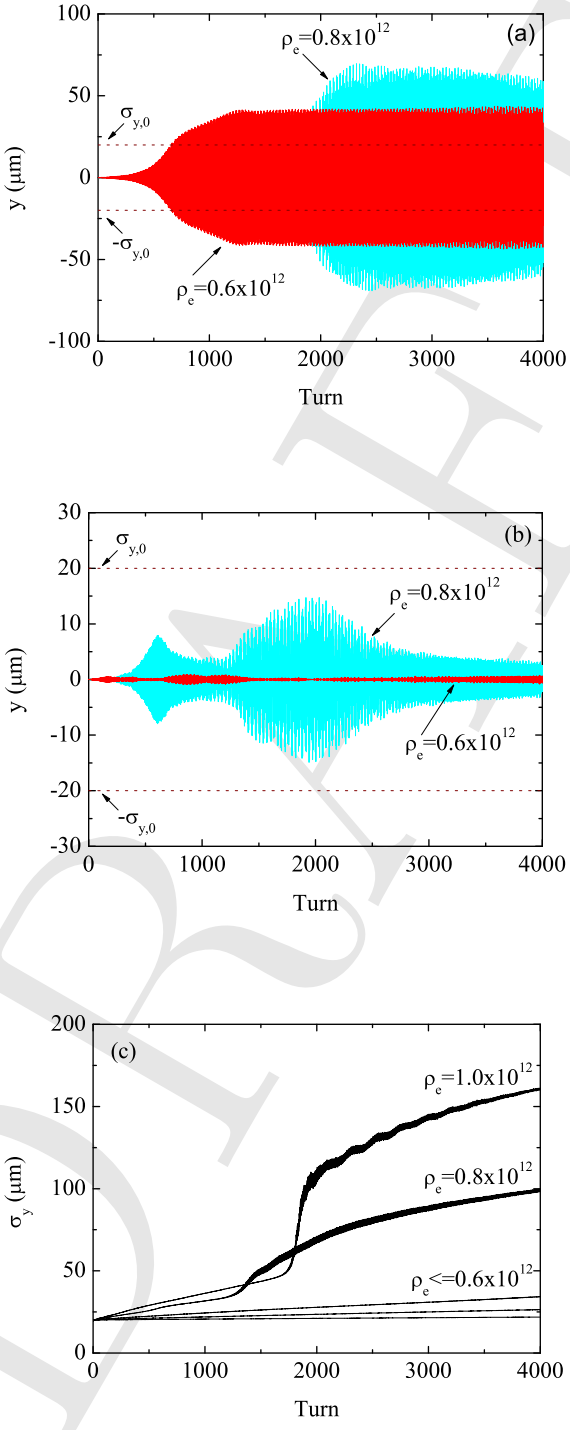

Figure 1.95: Evolution of the dipole motion (a) without and (b) with feedback in 2 GeV case. (c) Vertical beam size growth with feedback in 2 GeV case.

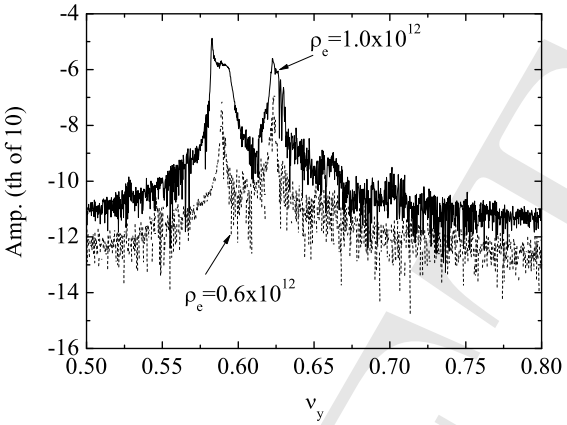

Figure 1.96: Frequency spectrum with feedback in 2 GeV case.

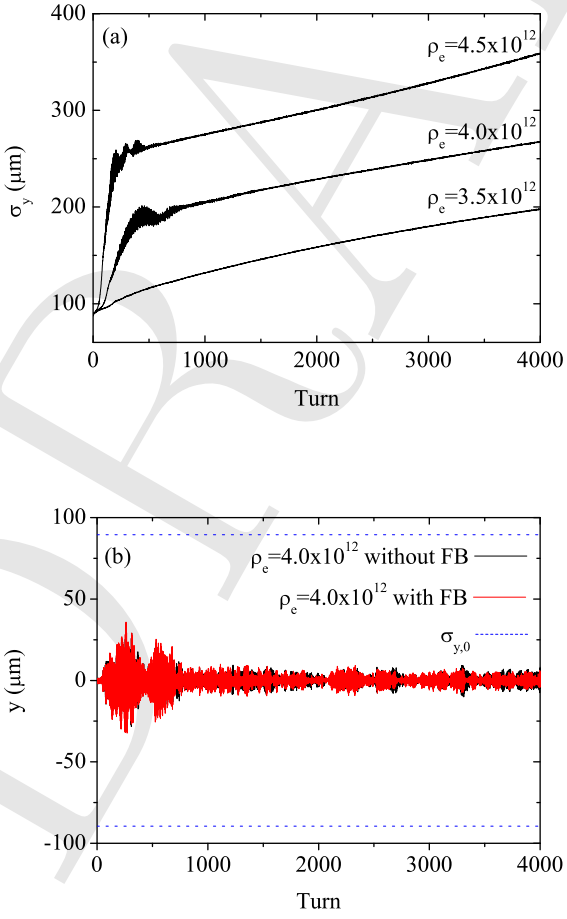

Figure 1.97: (a) Evolution of the beam size with feedback and (b) dipole moment with and without feedback in 5 GeV case.

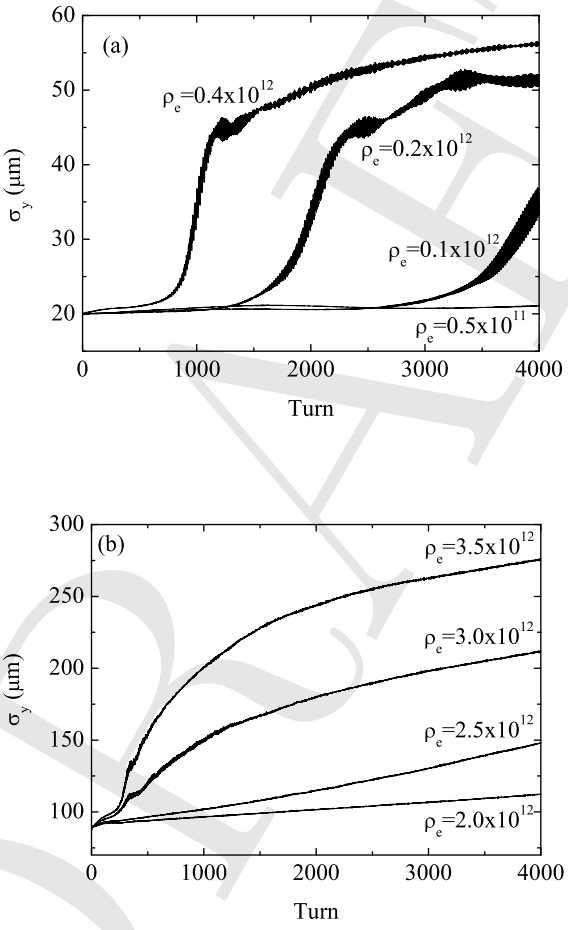

Figure 1.98: Evolution of the beam size with dispersion in (a) 2 and (b) 5 GeV cases.

Incoherent emittance growth below the instability threshold Electrons in the cloud are raked and pinched by the beam force when the beam passes through the electron cloud. This pinching of the electrons results in an enhancement of the tune spread and the enlargement of the vertical emittance. This type of emittance growth is caused by a diffusion due to nonlinear force [36].

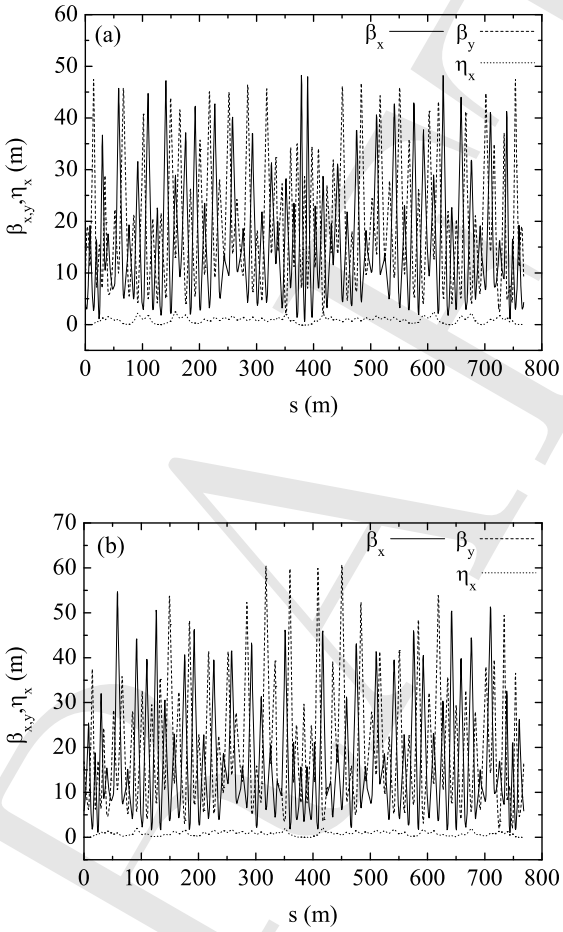

Figure 1.99: Lattice functions for (a) 2 and (b) 5 GeV cases in CesrTA. The super-periodicity is one in both cases. The horizontal, vertical beta functions ($\beta_{x,y}$) and the dispersion (η_x) are depicted. The average β_x (β_y) is about 15 (20) m in 2 GeV and 16 (20) m in 5 GeV cases. The average η_x is about 0.8 and 0.7 m in 2 and 5 GeV cases, respectively.

We use realistic lattices to investigate the incoherent effects of the electron cloud in CesrTA. Figure 1.99 shows the beta functions and dispersion in these realistic lattices. The twiss parameters of the realistic lattices are obtained from the MAD program [12].

There are 83 bending magnets, and we consider those as the interaction points between the bunch and the cloud. The magnetic field of the bending magnets is set to be 0.076 T and 0.19 T, for 2 and 5 GeV lattices, respectively. Figure 1.100 shows the evolution of vertical beam size for various cloud densities in the 2 and 5 GeV cases, respectively. The thresholds of cloud densities are about 1.2×10^{12} and 5.0×10^{12} m^{-3}, for the 2 and 5 GeV cases, respectively. These values are about 50%

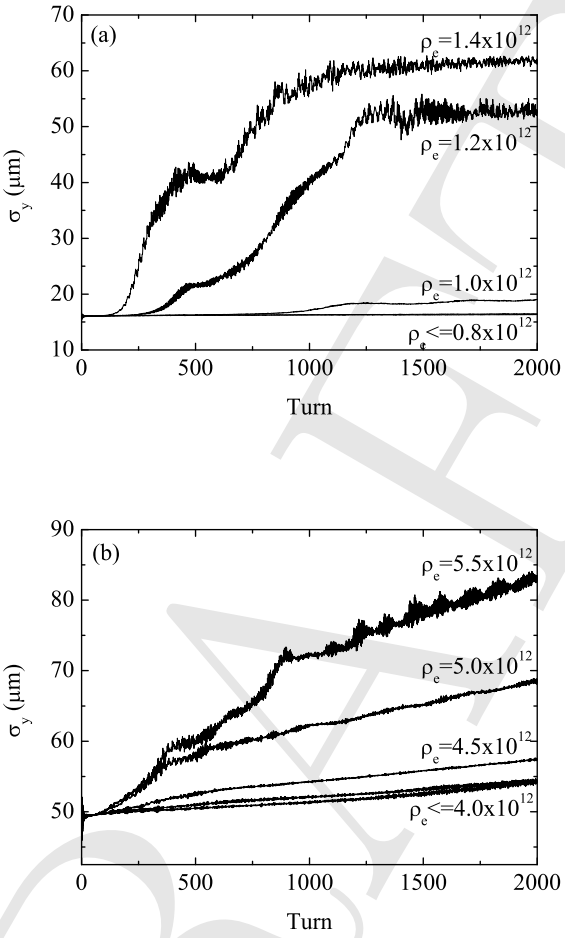

Figure 1.100: Evolution of the beam size in (a) 2 and (b) 5 GeV cases using the realistic lattices.

Table 1.8: Instability threshold estimates for CesrTA. The simple model consists of the eight integration steps and uniform beta function at each interaction point. The lattice parameters for the realistic model are obtained from the MAD program. All threshold cloud densities are in units of 10^{12} m^{-3}.

	2 GeV	5 GeV
Analytical estimate, using equations given in Sec. 1.2.2	0.82	3.2
Simple model(zero η_x, without FB)	0.6	4.0
Simple model(zero η_x, with FB)	0.8	4.0
Simple model(non-zero η_x, without FB)	0.2	3.0
Realistic model	1.2	5.0

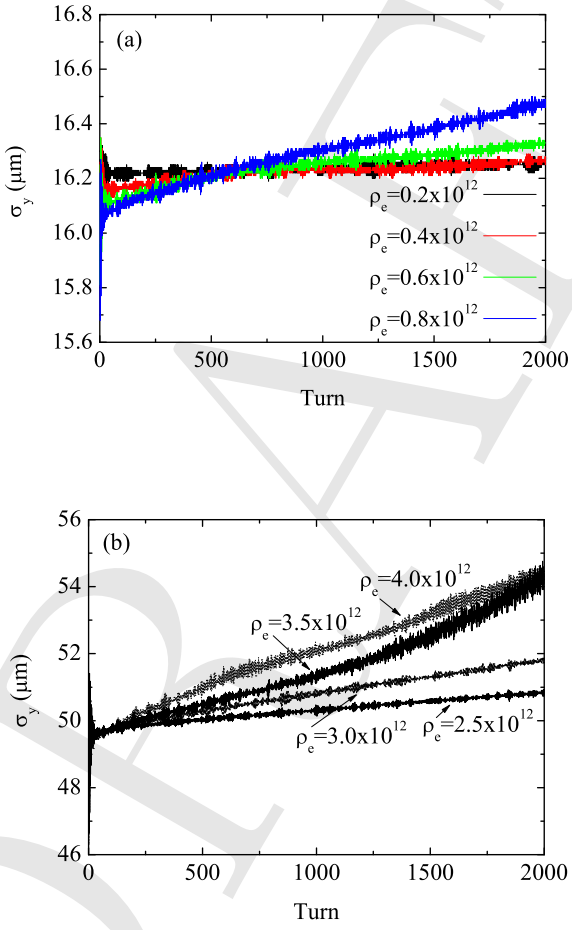

Figure 1.101: Evolution of the beam size below the threshold in (a) 2 and (b) 5 GeV cases.

higher than the analytical estimates. The difference between the threshold densities obtained with various simulation assumptions is presented in Table 1.8.

Figure 1.101 shows the evolution of vertical beam size for various cloud densities below the threshold. The coherent motion of cloud and bunch shown in Fig. 1.91 does not appear below the threshold. The growth rate increases depending on the cloud density below the threshold.

At the electron-cloud density, 0.8×10^{12} m^{-3} in the 2 GeV case, the growth rate is about 7.4×10^{-6} σ_y/turn. This is smaller than the radiation damping rate of CesrTA at 2 GeV, $4.6 \times 10^{-5} \sigma_y$/turn. Assuming that the electron-cloud growth rate is proportional to the vertical beam size, the equilibrium vertical emittance will increase by a factor of $4.6/(4.6 - 0.74) \approx 1.2$ due to subthreshold incoherent emittance growth.

Similarly, at the electron-cloud density, 4.0×10^{12} m^{-3} in the 5 GeV case, the growth rate is about 4×10^{-5} σ_y/turn. This is smaller than the radiation damping rate of CesrTA at 5 GeV, $1.4 \times 10^{-4} \sigma_y$/turn. Assuming that the electron-cloud growth rate is proportional to the vertical beam size, the equilibrium vertical emittance will increase by a factor of $1.4/(1.4 - 1) \approx 1.4$ due to subthreshold incoherent emittance growth.

Beam size increases of this magnitude are significant, and should be observable at CesrTA.

1.3.5.3 CMAD simulations

This subsection provides a comprehensive set of results obtained using the simulation program `CMAD`. Details of the computation methods employed by `CMAD` have been discussed in section 1.2.3. In particular, we take a closer look at electron cloud induced effects on positron beams, including head-tail motion, emittance growth and motion of single particles for parameters specific to ongoing experimental studies at CesrTA The correspondence between simulation and experimental results will also be discussed. The parameters used here represent conditions of CesrTA during experiments being carried out to study the influence of electron clouds on the dynamics of positron beams. Several features such as head tail motion and beam emittance calculations show similar features as to what has already been observed [37, 38]. In these experiments, we have typically used trains varying from 20 to 45 bunches in length. Depending upon properties such as, the bunch current, bunch spacing, surface properties of the vacuum chamber, etc, each bunch creates a certain amount of cloud and, as a result the trailing bunches experience a higher cloud density as compared to the leading ones. CesrTA instrumentation has the ability to observe the turn-by-turn position and the beam size of each of the bunches. CMAD tracks a single bunch and so in order to simulate the effect of different bunches along the train, we perform a set of independent calculations with varying pre-specified cloud densities. The cloud densities seen by the different bunches can be estimated from cloud build up simulations or from experimentally observed tune shifts. The tune shifts calculated from build up simulations have agreed well with observed tune shifts [19, 39]. CMAD presently assumes a uniform distribution of electrons. Work is underway to have the program be able to use any distribution as an initial condition. In the results presented here, we used a 2.08GeV beam, which is the energy most of the experiments have been performed. In these simulations, particles are tracked through the full lattice, where each element of non-zero length in the lattice consists of a cloud-beam "interaction point". Thus, the simulation takes into account the variation of the beam size based upon the beta function and dispersion all around the ring. The calculations model the bunch in 96 slices, and the charge from each slice is distributed

over a 128 × 128 grid, with 300000 macro particles (positrons) and 100000 macro electrons. The physical parameters are given in table 1.9

Table 1.9: .

Parameter	Unit	Value
Energy	GeV	2.08
Bunch Current	mA	1
Bunch Length	mm	12.2
Vertical emittance	pm	20
Horizontal emittance	nm	2.6
Energy spread		8.12×10^{-4}
Horizontal tune		14.57
Vertical tune		9.62
Synchrotron tune		0.055
Horizontal chromaticity	$dQ/(dp/p)$	0.6
Vertical chromaticity	$dQ/(dp/p)$	2.3

Motion of bunch centroid

In this section, we discuss the behavior of the centroid motion for varying cloud densities. The bunch initially had no offset. Nevertheless, a small inaccuracy in the centroid position introduced by the finite number of macro particles is sufficient to trigger a self excitation of the centroid motion that increases with cloud density. A very similar trend in the self excitation has been seen in measurements. Of course, the mechanism of the initial perturbation in the beam offset is different in experiments, *ie* it is not numerical. The self excitation is produced by nonlinear coupling between the two transverse degrees of freedom. In addition, the effect of longitudinal motion will also play a role due to the presence of dispersive coupling between the longitudinal and horizontal motion.

Figure 1.102 shows the vertical bunch displacement versus turn, normalized to the initial beam size, for varying cloud densities. The extent of self excitation clearly grows with cloud density. In some cases, we also see stages of damping induced by the electron clouds. The oscillation clearly becomes more chaotic as the cloud density increases. The horizontal motion, not shown here, is far more stable than the vertical simply because the horizontal size of the beam is larger by about a factor of 100.

Figure 1.103a shows the spectrum of centroid motion of all the bunches simulated, with the electron density progressively increasing as it would along a train. The primary peak corresponds to the vertical betatron tune and the secondary peaks on either side of the betatron peak are first and second order syncho-betatron sidebands. We see the tunes, along with the sidebands, gradually shifting as we go further behind the "train". The second order sidebands become clearly visible at a later stage, somewhere midway in the "train". All the above features have been observed in experiments conducted at CesrTA [37, 38] under similar conditions. Certain details such as the nature of the splitting of the betatron tune peak differs in simulations when compared to experimental observations. Figure 1.103b shows a summary of the heights of the left and right first order sidebands along with vertical betatron peaks for the same set of cloud densities as shown in Figure 1.103a. We see that a transition in the relative height of at least one of the sideband

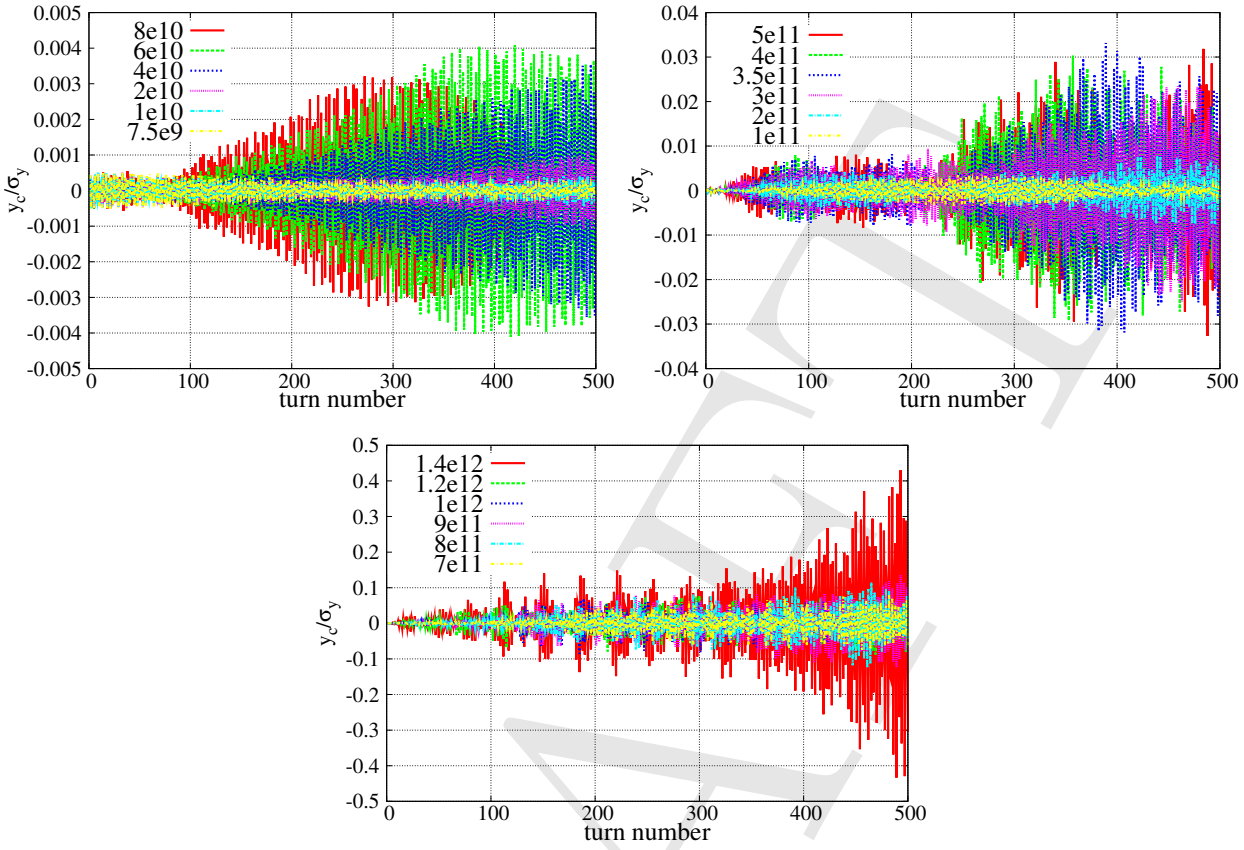

Figure 1.102: Motion of vertical bunch centroid for varying cloud densities.

peaks occurs at cloud densities of $3.5 \times 10^{11} m^{-3}$ and $4 \times 10^{11} m^{-3}$. For cloud densities beyond these values, we see that both the sideband heights remain relatively close in height to the betatron peaks. Figure 1.103c shows the position of the betatron and both the sideband peaks in tune space. We see the gradual shift in betatron tune. Additionally, we see that the sideband peaks are consistently spaced away from the betatron peak by the value of the synchrotron frequency. We do not see an evidence of the first and second order sidebands approaching each other as has been seen at KEK [31]. This phenomenon occurs due to coupling between the different order modes. On the other hand, our simulation results are consistent with what has been observed at CesrTA under the same conditions. It is likely that such a mode coupling would become observable at higher bunch currents and cloud densities. This is yet to be confirmed as to what the conditions at CesrTA should be to observe such a mode coupling.

Calculation of emittance growth rate

Figure 1.104 shows the vertical emittance growth versus turn. The vertical emittance undergoes a higher growth rate due to its smaller initial value compared to the horizontal emittance, not shown here. In PIC simulations, one needs to worry about numerical noise contributing to emittance growth. Numerical noise can contribute to particles artificially straying away from a stable region to an unstable one. This can be minimized by optimally choosing certain computational parameters such as grid spacing, macro particles and extent of the cloud. A study was conducted over a range of these parameters before deciding upon the current set used in these simulations.

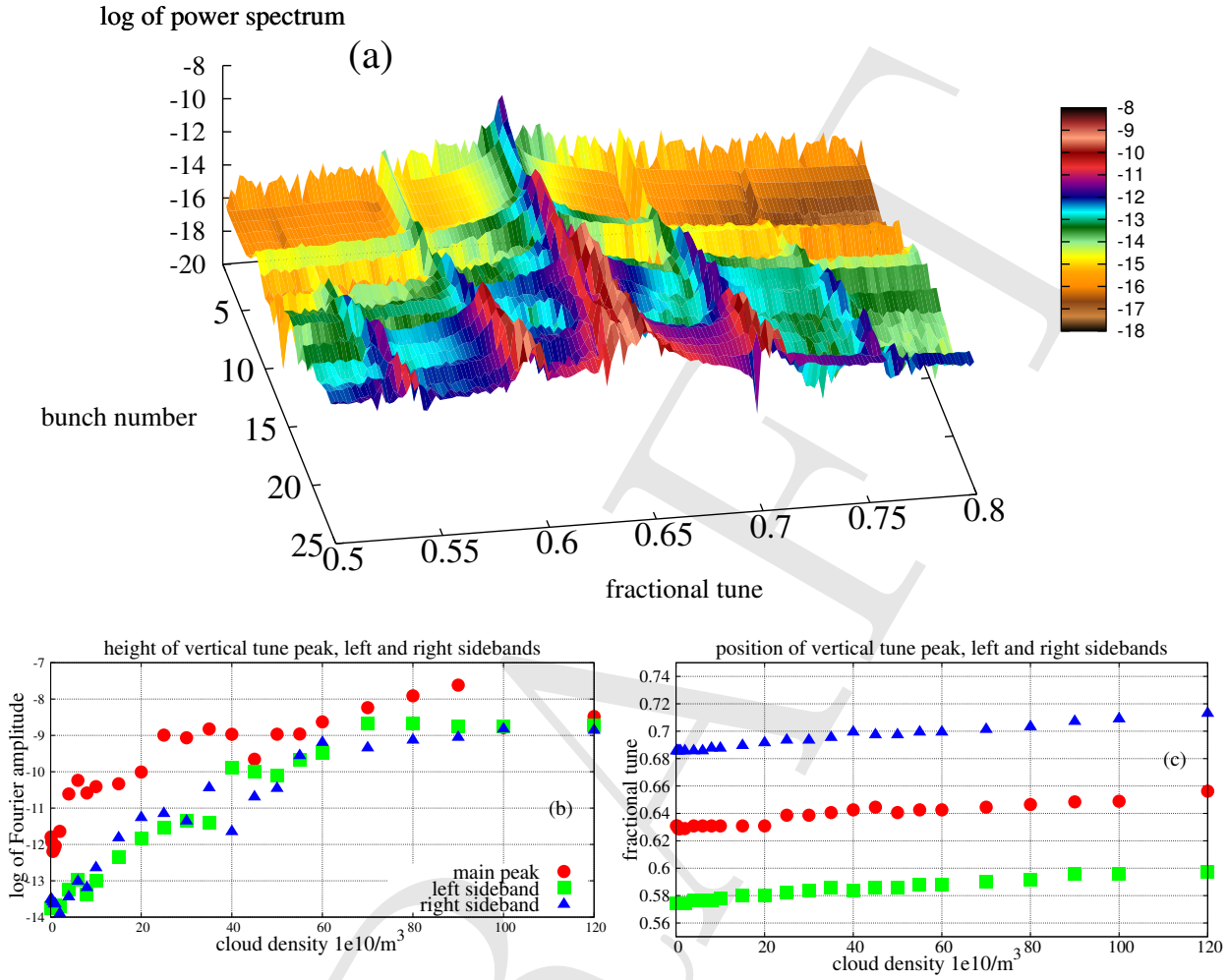

Figure 1.103: Plots showing the combined spectra of all bunches simulated and the relative heights and positions of betatron and sideband peaks.

Despite the uncertainty in estimating the emittance growth rate, we see a definite increase in this quantity in correspondence with the height of the sidebands which is consistent with observations from the X-ray beam size monitor (xBSM) at CesrTA. However, it must be noted that the xBSM measures the beam size after the beam has reached a quasi-equilibrium state, while in simulations we are, in the first 500 turns still looking at a transient state, with the emittance still growing linearly. We also see a transition from a linear to an exponential emittance growth when the cloud density increases from 1.4×10^{12} to 1.6×10^{12} electrons m^{-3}. In order to make a closer comparison between experiments and simulations, one needs to calculate the quasi equilibrium emittance. This would require including the effect of radiation damping and quantum excitations and tracking the beam for several damping times. The damping time of the CesrTA 2GeV configuration is about 21000 turns.

Motion of Individual Particles

We have observed the motion of individual test particles in order to study their confinement prop-

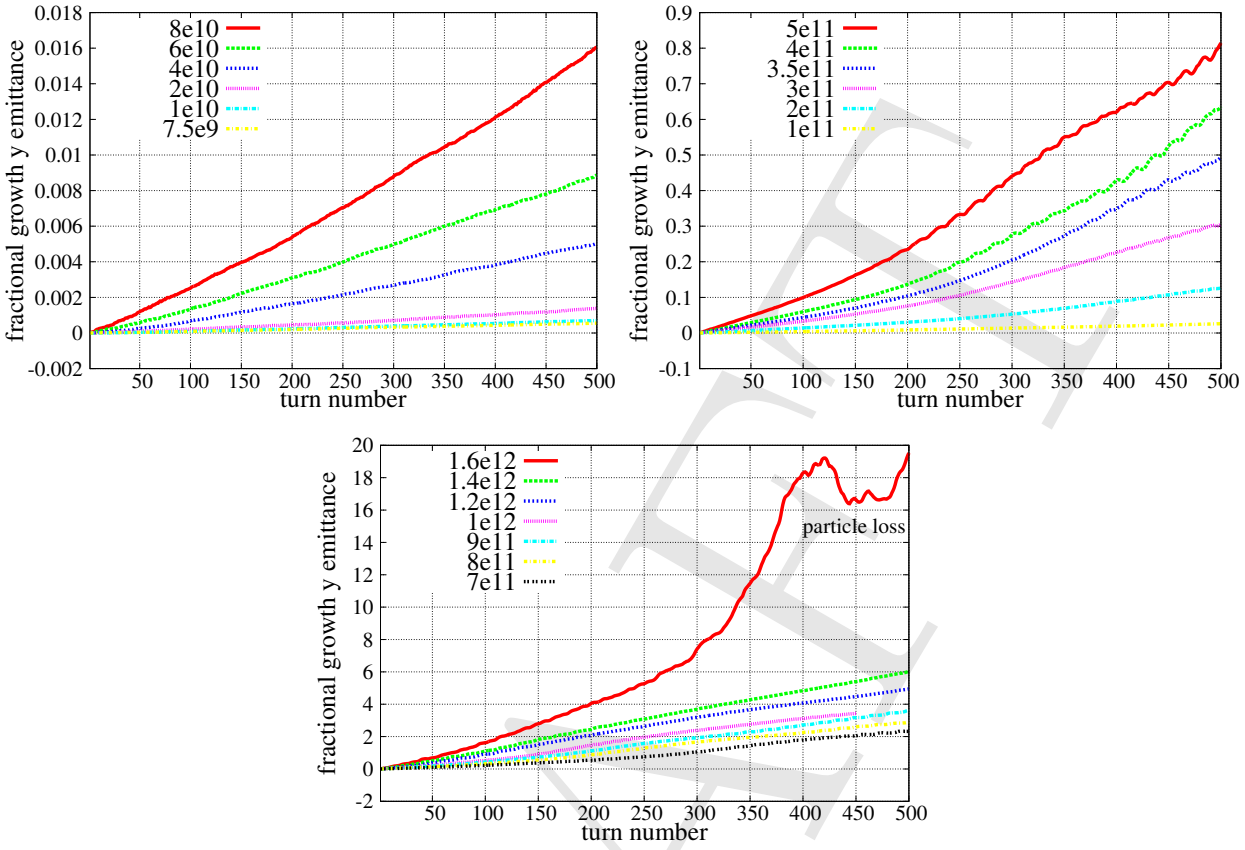

Figure 1.104: Vertical emittance growth rate for varying cloud densities

erties for varying cloud densities and also how their oscillation frequency varies with change in oscillation amplitude. Although it would be difficult to determine these quantities experimentally, probing into such details with the help of simulations can provide significant insight into the underlying physical processes and the mechanisms that drive the beams unstable in the presence of electron clouds.

In Figure 1.105, we show the vertical phase space trajectories of particles initially at $x = 0.1 \times \sigma_x$, $y = 0.1 \times \sigma_y$ and $z = 0.1 \times \sigma_z$. The small initial offset ensures that coupling between the three degrees of freedom, if present affects the dynamics of the particle motion. We clearly see that the particles stray away from the ellipse as the electron density increases. The variation of the tune with oscillation amplitude for various cloud densities can in principle be estimated with the help of such single particle trajectories. We plan to extend the analysis of single particle trajectories beyond just phase space traces to computing tune footprints for different cloud densities.

In conclusion, we note that CMAD has been able to reproduce several features of the dynamics of positron beams observed in experiments. This study was performed for a parameter set corresponding to one set of observations at CesrTA. We intend to extend this study to other conditions at which observations have been made and will be made in future. At the same time, there is an on going effort to include more features into CMAD to enable more detailed quantitative comparisons with measurements.

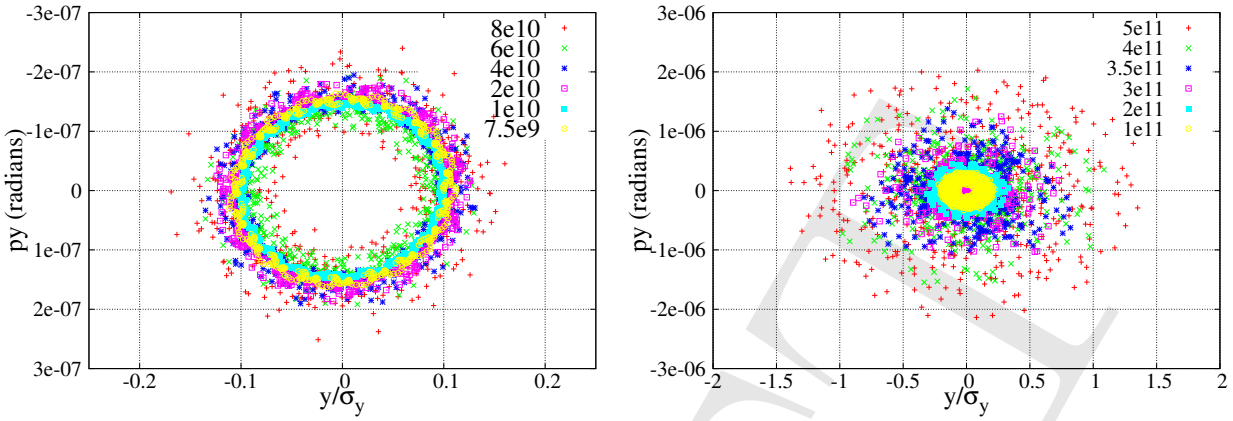

Figure 1.105: Vertical emittance growth rate for varying cloud densities

1.4 Summary and Further Investigations

Appendix A

Some LaTeXing Examples

This appendix provides some examples of how to do things in LaTeX for the Phase I Report and provides some guidelines for preparing material for the report.

Note for experienced LaTeX users: the Phase I Report will generally follow "standard" usage for LaTeX and BibTeX. Hence, you do not need to peruse the examples below in detail; it is recommended that you skim through the material and make note of the guidelines for the preparation of the report (in particular, see Section A.2.2, Section A.7.1, and Section A.7.3). Note that the additional features provided by the 'graphicx' and 'natbib' packages will be available (as described in some of the examples below), but standard commands for graphics inclusion and citations will still work if you prefer to use them.

We fully expect that some formats will evolve through the course of editing the full document. We will add further examples, as needed, based on questions that come from the contributors. So **check back often!**

A.1 Special Commands

For CesrTA, use the command:

```
\cesrta
```

If you need to force a space after CesrTA, then use:

```
\cesrta\
```

A.2 Figures

A.2.1 Figure Logistics

The following figures show examples of the commands for inserting various types of graphics. Graphics files in JPEG, PDF, EPS, and PNG can be readily incorporated into the document. If you need help including a file of a different type, please consult with the editors. Each figure must include a caption and a label for cross-referencing the figure in the text.

Figure A.1 shows an example in which the graphic is a JPEG photo. In this example, the size is set by specifying the width as an absolute dimension. The height is not specified, which results in the aspect ratio being preserved. The graphic is centered between the left and right margins.

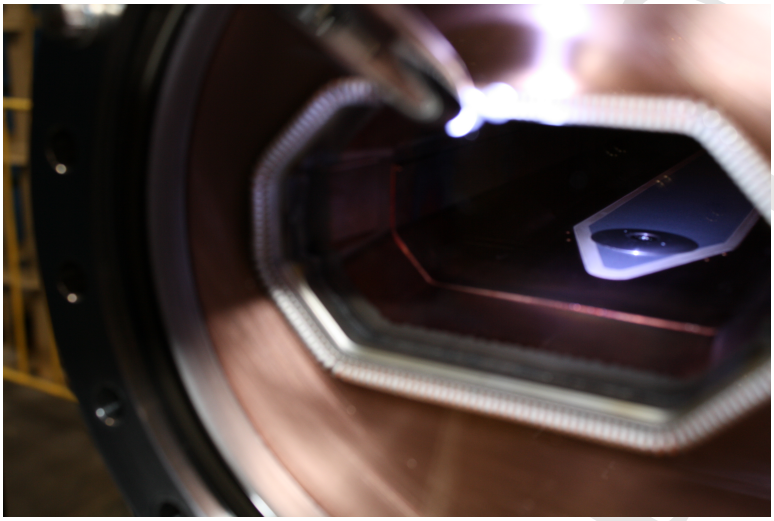

Figure A.1: Example of including a JPEG photo.

Figure A.2 shows an example in which the graphic is a PDF file. In this example, the size is set by specifying the width relative to the column width (the report is one-column, so the column width is equal to the text width).

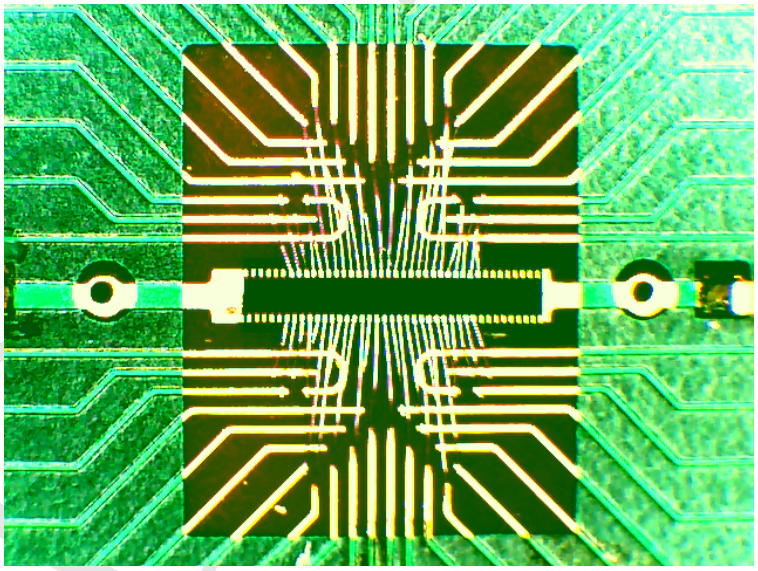

Figure A.2: Example of including a PDF photo. The caption can contain additional information that is relevant to the figure. Although the figure can obviously be discussed in the text of the report, it may be helpful to put some information directly in the caption.

Figure A.3 shows an example in which the graphic is an EPS file. In this example, the height is specified as an absolute dimension, and the aspect ratio is preserved by not specifying the width.

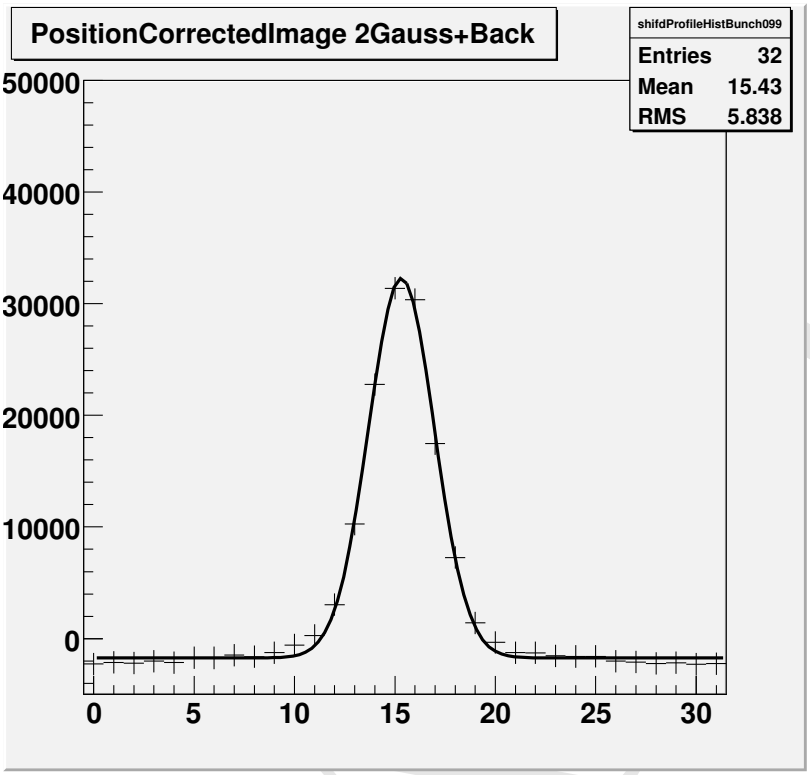

Figure A.3: Example of including an EPS plot.

Figure A.4 shows an example in which the graphic is a PNG file. In this example, the height is specified relative to the text height. The height of the figure should always be smaller than the text height in order to allow room for the figure caption.

Captions are produced with an automatically-generated figure number using the `\caption` command. The caption should be below the graphics. For long figure captions, it is useful to provide a short caption as an optional argument. The short caption is used in the list of figures. This is illustrated in Figure A.2.

Figures may contain more than one graphic. Examples where this option may be useful include different views of the same object, different plots that are related to each other, and so on. Figure A.5 shows an example in which 2 graphics are included.

LaTeX allows for an optional argument to specify the placement of the figure on the page. Placement options include h (here), t (top of page), b (bottom of page), and p (on a separate page with no text). Generally it is better to not worry about the figure placement until the final stages of document preparation, since the figures locations will change as material is added or removed within one section or in preceding sections.

A.2.2 Figure Guidelines

Since the purpose of figures is to supplement the message conveyed in the text, all of the figures that appear in the report should be referenced in the text of the report.

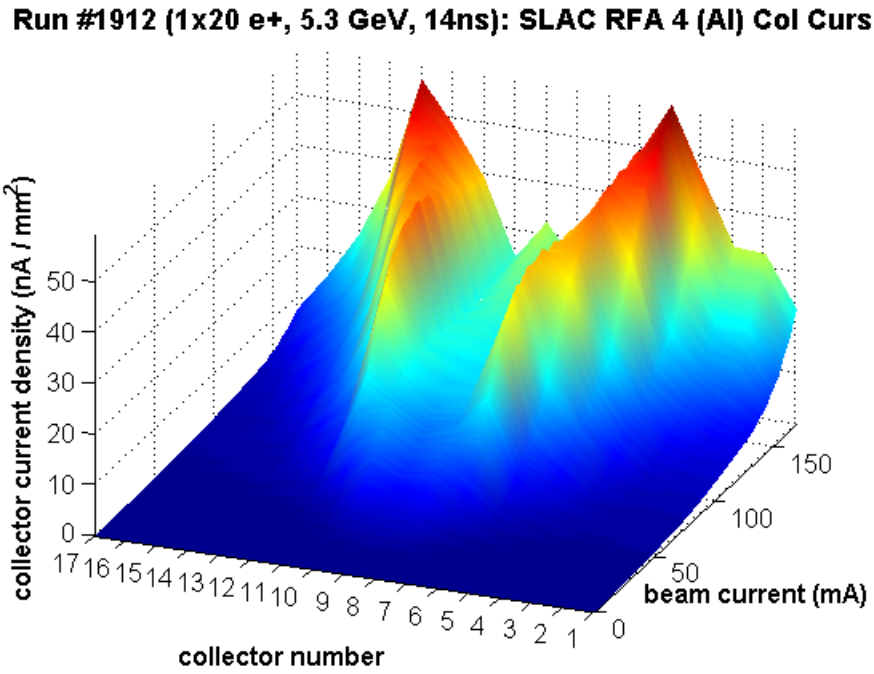

Figure A.4: Example of including a PNG plot.

Common categories of figures are photographs (see Figure A.1 and Figure A.2 for examples), plots (see Figure A.3 and Figure A.4 for examples), and drawings. JPEG is the recommended format for photographs. For plots and drawings, where possible, "vector" formats are recommended in lieu of "bit-mapped" formats. Vector formats generally provide better image resolution and smaller file sizes. JPEG and PNG formats are bit-mapped formats, so they should be avoided for plots and drawings if possible. Vector formats can be produced as EPS or PDF files (note, however, that EPS and PDF files can also be produced with bit-mapped content). Three-dimensional drawings may have to be produced as bitmaps.

Methods for producing graphic files may vary, depending on the software used to produce the graphic. "Save as EPS" is generally a good option, if available. "Save as PDF" may also work. In some case, it may be necessary to select "Print" and then print the graphic to a file, selecting "PostScript" or "PDF Creator" as the printer, and choosing "EPS" as a PostScript feature. If the output file has extension ".prn," this can be changed to ".eps."

Generally is is preferable to place information about the figure in the figure caption, rather than adding a label to the figure itself. According to this line of reasoning, the information at the top of Figure A.4 could be removed from the graphic and added to the caption.

A.3 Tables

This section provides an example table with the style features that are specified for the CesrTA Phase I Report. We appreciate your adherence to this format.

Table A.1 provides the list of chapters and coordinators for this project. Please feel free to contact

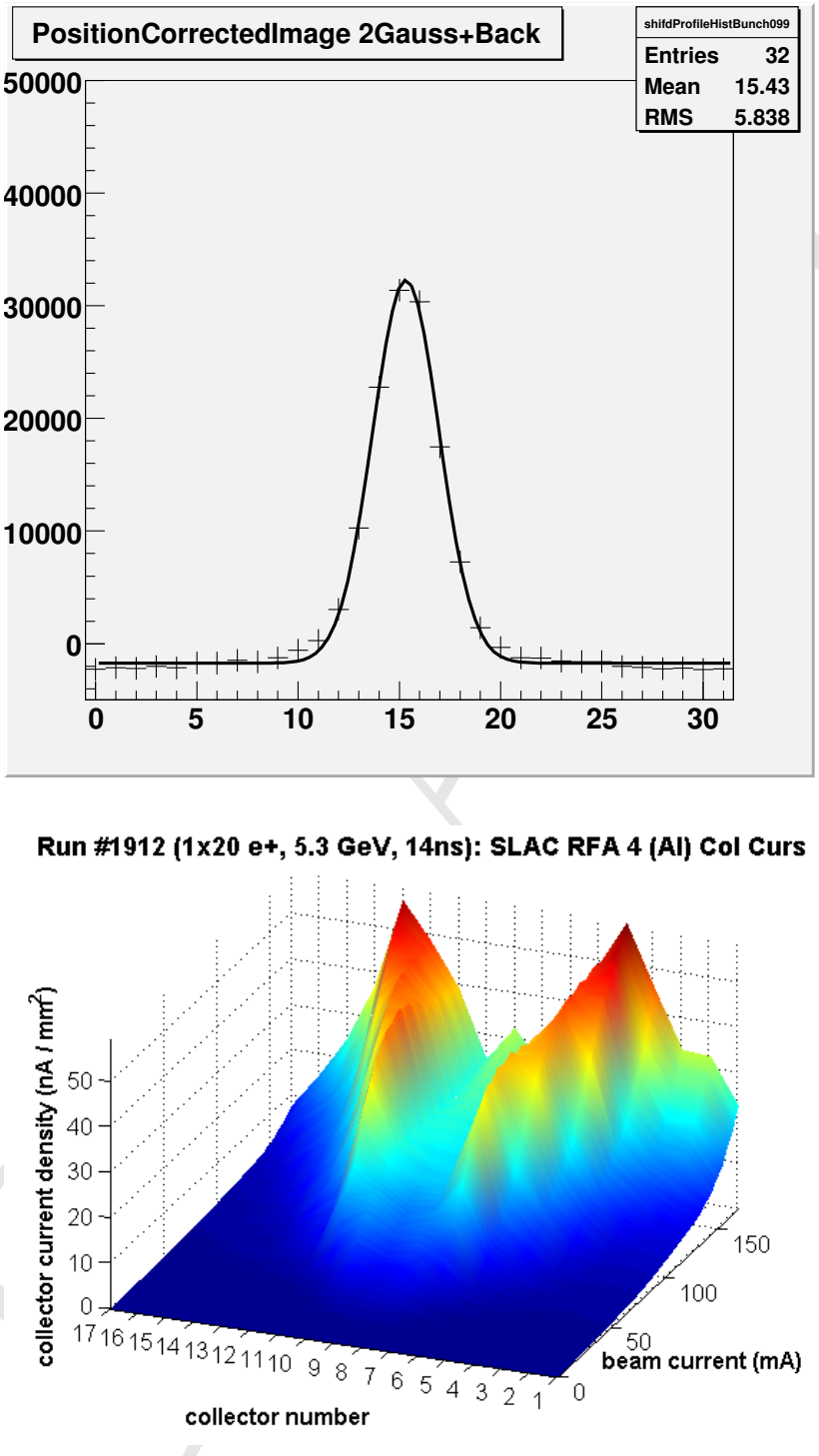

Figure A.5: Example of including two graphics in one figure. Top: top figure in EPS format. Bottom: bottom figure in PNG format.

them with questions about your LaTeX contributions.

Table A.1: List of chapter coordinators.

Chapter	Topic	Coordinator
Ch. ??	Introduction	M. Billing
Ch. ??	CESR Conversion	M. Palmer
Ch. ??	Low Emittance Tuning	D. Rubin
Ch. ??	EC Growth	M. Palmer
Ch. 1	EC Dynamics	G. Dugan
Ch. ??	ILC Recommendations	M. Palmer
Ch. ??	Conclusion	M. Billing
-	Bibliography	W. Hartung

As shown in this example, tables should be centered between the left and right margins. The caption should be placed above the table. A short form of the caption may be provided for the list of tables via the optional argument to the `\caption` command. The placement options and guidelines described above for figures also apply to tables.

A.4 Equations

Equations may be "in-text," such as $E = mc^2$, or displayed. Equation (A.1) is an example of a displayed equation generated by MathType:

$$\Delta a = 2\pi G_{\infty}\alpha\lambda\left(e^{-z/\lambda} - 1\right). \tag{A.1}$$

Please remember to **label** all equations. For a single equation, as in the example above, this can be done by using the `equation` environment, which produces the equation with an automatically-generated equation number. To cross-reference the equation in the text, as above, label it with a key using `\label{key}` inside the `equation` environment and then use `\ref{key}` to generate the equation number. As illustrated above, generally the format of the cross-reference should be something like

```
...as shown in Equation~(\ref{key}).
```

Note the inclusion of parentheses around the equation number.

For a group of two or more equations, use the `eqnarray` environment instead of the `equation` environment.

A.5 List Environments

When creating numbered or un-numbered lists, please use the list environments provided with /LaTeX/ in order to standardize the look and feel of the presentation instead of emulating it yourself. This is accomplished by using the *itemize* or *enumerate* environments. Note that lists can be nested. A bulleted list can be created with the following commands (note that the indentation used is to make the example more easily readable - it's not required):

```
\begin{itemize}
   \item First item
   \begin{itemize}
         \item First sub-item
         \item Second sub-item
   \end{itemize}
   \item Second item
   \item Third item
\end{itemize}
```

which renders as:

- First item
  - First sub-item
  - Second sub-item
- Second item
- Third item

If you prefer a numbered list you can use (note that the indentation used is to make the example more easily readable - it's not required):

```
\begin{enumerate}
   \item First item
   \begin{enumerate}
         \item First sub-item
         \item Second sub-item
   \end{enumerate}
   \item Second item
   \item Third item
\end{enumerate}
```

which renders as:

1. First item
   (a) First sub-item
   (b) Second sub-item
2. Second item
3. Third item

A.6 Cross-References

References to figures, tables, equations, and other parts of the report are all done in a similar way using a key to specify the item of interest. To reference a chapter or section (or subsection,...) of the report, make sure the item of interest has a `\label{key}` associated with it, and then reference it with the `\ref` command using its key, for example, Chapter **??**. The `\label{key}`

declaration should appear inside or just after the sectioning command which defines the beginning of the sectional unit.

A.7 Bibliography and Citations

A.7.1 Bibliography Logistics

The bibliography will be generated using BibTeX. A BibTeX database has been set up, mostly from a search for existing CesrTA papers and from citations therein. The supplementary material for the CesrTA proposal and review has also been included for the most part. Keys have been assigned to all entries in the BibTeX database. Additional keys will be assigned by the bibliography coordinator for new entries.

You may view the BibTeX file (CesrTA.bib) in CesrTA Wiki area for the Phase I Report (or download (check out) with the rest of the files). It is in the `Bibliography/` directory.

You may also view an HTML list of papers in the database with keys and links. The file (HtmlCesrTA.htm) is in the same directory as the BibTeX file. You may view it with a Web browser.

Please check whether all of the references you wish to cite are in the database and send the information for those that are missing to the bibliography coordinator. Alternatively, you may send your existing list of references to the coordinator, who can then add the missing ones to the database. You can send your reference list in the form of an existing BibTeX file, in another format, or in the form of a paper whose reference list you want to include in the database.

There will be one bibliography for the entire Phase I Report. Please notify the coordinator when you find errors and omissions in the database.

A.7.2 Citation Logistics

The report will make use of the 'natbib' package for citations. Citations will be numbered according to the order in which they appear. Instead of the standard `\cite{key}` command, please use natbib's `\citep{key}` command (for a "parenthetical" citation). You may provide a list of keys, as in `\citep{key1, key2,...}`. The natbib package will perform sorting and compression when multiple keys are provided.

Example: to cite a reference such as the CESR Conversion PAC09 paper [40], use

```
...during the CESR Conversion~\citep{PAC09:FR1RAI02}.
```

The tilde between the text and the citation inserts a "non-breakable" space, which prevents the citation from appearing at the beginning of a new line.

For those who find a non-standard command objectionable, natbib also allows the standard `\cite` command in place of `\citep`. The natbib package provides many other features, although they are mostly oriented toward support for "author-year" citations and are not likely to be very useful for numbered citations. Some of the natbib features are not fully supported by the bibliography style that we are using for the Phase I Report (`\citet`, for example), but this should not be an issue, since we are not using "author-year" citations.

You may wish to refer to a particular part of a paper that you cite (a page number, a section, a figure, a table, etc.). This is generally to be encouraged, especially when you are citing material in a book, design report, etc. The recommended method for this report is to cite the paper in the bibliography and specify the part of interest in the text. The optional argument of the `\citep` command may be useful for this purpose. Example:

```
This was already demonstrated before the last round of
measurements~\citep[Figures 3 and 4]{IPAC10:TUPD022}.
```

The above modifies the citation [41, Figures 3 and 4]. (Note that this works the same way as for the standard LaTeX `\cite` command.) By putting the specifics in the text, we can avoid multiple entries in the bibliography for the same work.

A.7.3 Bibliography and Citation Guidelines

It is preferable for the references in the bibliography to be ones that are available to the public. In cases where it is necessary for to cite work that is not in the public domain, you might consider how the work could be made publicly available. For work that is not suitable for journal articles or conference proceedings, there are other options, including e-print servers and archives of laboratory reports, including several report series associated with CESR/LEPP/CLASSE.

The bibliography can be used to acknowledge "private communications" for unpublished information, but this should be used sparingly (also, citing a "private communication" from someone who is one of the authors of the Phase I Report might be considered a circular argument).

You may wish to include information about a device or product and its manufacturer in the report. Please include this information in the text or in a footnote.[1] Example:

```
We used a dc electron gun\footnote{Model ELG-2, Kimball
Physics, Inc., Wilton, NH.} positioned at 25 degrees
to the manipulator.
```

A.7.4 Bibliography Details

The coordinator will try to make sure that consistency is maintained between different database entries and will try to identify and eliminate duplicate entries associated with works that have been published in more than one way. For cases in which a paper is determined to have been published as an internal report/pre-print/e-print as well as a proceedings paper or a journal article, the latter version will be used preferentially.

In assigning keys, the goal is to maintain a scheme whereby a unique key can be associated with each entry in the database. The disadvantage is that the keys are long. The advantage (we hope) is that the bibliography database can be expanded and updated in the future for other reports, proposals, etc.

The format of the bibliography will be determined by the BibTeX bibliography style, and will not necessarily be the same as the list of papers mentioned above (which was converted to HTML using somewhat primitive methods). In particular, the bibliography will not include URLs.

[1] This is an example of a footnote.

The rule of thumb is that each entry in the bibliography will be a "stand-alone" entry. In other words, the XREF feature of BibTeX will not be used to cross-reference one entry to another.

Bibliography

[1] H. Jin *et al.*, "Electron Cloud Effects in Cornell Electron Storage Ring Test Accelerator and International Linear Collider Damping Ring," *Jpn. J. Appl. Phys.* **50**, 026401 (Feb. 2011).

[2] K. Ohmi, "Particle-in-Cell Simulation of Beam-Electron Cloud Interactions," in *Proceedings of the 2001 Particle Accelerator Conference, Chicago, IL*, P. Lucas & S. Webber, Eds. (2001), p. 1895–1897.

[3] M. T. F. Pivi, "CMAD: A New Self-consistent Parallel Code to Simulate the Electron Cloud Build-up and Instabilities," in *Proceedings of the 2007 Particle Accelerator Conference, Albuquerque, NM*, C. Petit-Jean-Genaz, Ed. (2007), p. 3636–3638.

[4] D. Schulte & F. Zimmermann, "Electron Cloud Build-Up Simulations using ECLOUD," in *Proceedings of ECLOUD 2004: 31st ICFA Advanced Beam Dynamics Workshop on Electron-Cloud Effects, Napa, CA*, M. Furman, S. Henderson & F. Zimmerman, Eds. (2004), CERN-2005-001, p. 143–152.

[5] G. Rumolo & F. Zimmermann, "Electron Cloud Simulations: Beam Instabilities and Wakefields," *Phys. Rev. ST Accel. Beams* **5**, 121002 (Dec. 2002).

[6] M. A. Furman & G. R. Lambertson, "The Electron-Cloud Instability in the Arcs of the PEP-II Positron Ring," in *Proceedings of MBI97: International Workshop on Multibunch Instabilities in Future Electron and Positron Accelerators, Tsukuba, Japan, 1997*, Y. H. Chin, Ed. (1997), KEK Proceedings 97-17, p. 170.

[7] M. A. Furman & M. T. F. Pivi, "Probabilistic Model for the Simulation of Secondary Electron Emission," *Phys. Rev. ST Accel. Beams* **5**, 124404 (Dec. 2002).

[8] K. Ohmi, S. Heifets & F. Zimmermann, "Study of Coherent Tune Shift Caused by Electron Cloud in Positron Storage Rings," in *Proceedings of the Second Asian Particle Accelerator Conference, Beijing, China* (2001), p. 445–447.

[9] K. Ohmi, F. Zimmermann & E. Perevedentsev, "Wake-Field and Fast Head-Tail Instability Caused by an Electron Cloud," *Phys. Rev. E* **65**, 016502 (Dec. 2001).

[10] A. W. Chao, *Physics of Collective Beam Instabilities in High Energy Accelerators*, John Wiley & Sons, New York (1993).

[11] K. Ohmi, "Electron Cloud Instabilities in the Damping Ring of International Linear Collider," in *Proceedings of the 2005 International Linear Collider Physics and Detector Workshop and Second ILC Accelerator Workshop, Snowmass, CO*, N. A. Graf, Ed. (2005), SLAC-R-798/eConf:C0508141.

[12] H. Grote & F. C. Iselin, "The MAD Program (Methodical Accelerator Design) Version 8.10 User's Reference Manual," Tech. Rep. CERN-SL-90-13-AP-rev-3, CERN, Geneva, Switzerland (Jan. 1993).

[13] K. G. Sonnad *et al.*, "Progress on Simulation of Beam Dynamics with Electron Cloud Effects: An Update," in *Proceedings of ECLOUD 2010: 49th ICFA Advanced Beam Dynamics Workshop on Electron Cloud Physics, Ithaca, NY*, K. Smolenski, Ed. (in press).

[14] J.-L. Vay, A. Friedman & D. P. Grote, "Self-Consistent Simulations of High-Intensity Beams and E-Clouds with WARP POSINST," in *Proceedings of ICAP 2006: International Computational Accelerator Physics, Chamonix, France* (2006), p. 256–262.

[15] F. C. Iselin, "Lie Transformations and Transport Equations for Combined-Function Dipoles," *Part. Accel.* **17**, p. 143–155 (Oct. 1985).

[16] M. Frigo & S. G. Johnson, "The Design and Implementation of FFTW3," *Proc. IEEE* **93**, p. 216–231 (Feb. 2005).

[17] Y. Cai *et al.*, "Simulation of the Beam-Beam Effects in e^+e^- Storage Rings with a Method of Reduced Region of Mesh," *Phys. Rev. ST Accel. Beams* **4**, 011001 (Jan. 2001).

[18] J. P. Boris, "Relativistic Plasma Simulation—Optimization of a Hybrid Code," in *Proceedings of the Fourth Conference on the Numerical Simulation of Plasmas, Washington DC*, J. Boris & R. Shanny, Eds., Naval Research Laboratory, Washington DC (1970), p. 3–67.

[19] D. L. Kreinick *et al.*, "Using Coherent Tune Shifts to Evaluate Electron Cloud Effects on Beam Dynamics at CesrTA," in *Proceedings of ECLOUD 2010: 49th ICFA Advanced Beam Dynamics Workshop on Electron Cloud Physics, Ithaca, NY*, K. Smolenski, Ed. (in press).

[20] J. A. Crittenden *et al.*, "Progress in Studies of Electron-cloud-induced Optics Distortions at CesrTA," in *Proceedings of the 2010 International Particle Accelerator Conference, Kyoto, Japan* (2010), p. 1976–1978.

[21] J. A. Crittenden *et al.*, "Studies of the Effects of Electron Cloud Formation on Beam Dynamics at CesrTA," in *Proceedings of the 2009 Particle Accelerator Conference, Vancouver, BC* (2009), p. 4631–4633.

[22] J. R. Calvey *et al.*, "Electron Cloud Modeling Considerations at CesrTA," in *Proceedings of the 2009 Particle Accelerator Conference, Vancouver, BC* (2009), p. 3306–3308.

[23] C. M. Celata, "Electron Cloud Dynamics in the Cornell Electron Storage Ring Test Accelerator Wiggler," *Phys. Rev. ST Accel. Beams* **14**, 041003 (Apr. 2011).

[24] J.-L. Vay *et al.*, "Update on Electron-Cloud Simulations Using the Package WARP-POSINST," in *Proceedings of the 2009 Particle Accelerator Conference, Vancouver, BC* (2009), p. 4719–4721.

[25] L. F. Wang *et al.*, "Numerical Study of the Photoelectron Cloud in KEKB Low Energy Ring with a Three-Dimensional Particle in Cell Method," *Phys. Rev. ST Accel. Beams* **5**, 124402 (Dec. 2002).

[26] L. F. Wang, "User's Guide for CLOUDLAND," Tech. Rep. KEK Internal 2003-2, KEK, Tsukuba, Japan (2003).

[27] L. Wang & M. Pivi, "Trapping of Electron Cloud in ILC/CesrTA Quadrupole and Sextupole Magnets," in *Proceedings of ECLOUD 2010: 49th ICFA Advanced Beam Dynamics Workshop on Electron Cloud Physics, Ithaca, NY*, K. Smolenski, Ed. (in press).

[28] G. F. Dugan, M. A. Palmer & D. L. Rubin, "ILC Damping Rings R&D at CesrTA," in *ICFA Beam Dynamics Newsletter*, J. Urakawa, Ed., International Committee on Future Accelerators, No. 50, p. 11–33 (Dec. 2009).

[29] R. Cimino, I. R. Collins & V. Baglin, "VUV Photoemission Studies of Candidate Large Hadron Collider Vacuum Chamber Materials," *Phys. Rev. ST Accel. Beams* **2**, 063201 (Jun. 1999).

[30] J. W. Flanagan *et al.*, "Single-Shot Resolution of X-Ray Monitor using Coded Aperture Imaging," in *Proceedings of DIPAC 2011: 10th European Workshop on Beam Diagnostics and Instrumentation for Particle Accelerators, Hamburg, Germany* (in press).

[31] J. W. Flanagan *et al.*, "Observation of Vertical Betatron Sideband due to Electron Clouds in the KEKB Low Energy Ring," *Phys. Rev. Lett.* **94**, 054801 (Feb. 2005).

[32] J. W. Flanagan *et al.*, "Further Studies on Betatron Sidebands due to Electron Clouds," in *Proceedings of the 2006 European Particle Accelerator Conference, Edinburgh, Scotland* (2006), p. 2898–2900.

[33] K. Ohmi *et al.*, "Simulation Analysis of Head-Tail Motion Caused by Electron Cloud," in *Proceedings of the 2005 Particle Accelerator Conference, Knoxville, TN*, C. Horak, Ed. (2005), p. 907–909.

[34] E. Benedetto *et al.*, "Simulation of the Synchro-Betatron Sideband Instability Caused by Electron Clouds at KEKB," in *Proceedings of the 2007 Particle Accelerator Conference, Albuquerque, NM*, C. Petit-Jean-Genaz, Ed. (2007), p. 4033–4035.

[35] K. Ohmi & H. C. Jin, "Fast Head Tail Instability due to Electron Cloud under the Presence of the Dispersion," in *Proceedings of the 2009 Particle Accelerator Conference, Vancouver, BC* (2009), p. 4686–4688.

[36] E. Benedetto, G. Franchetti & F. Zimmermann, "Incoherent Effects of Electron Clouds in Proton Storage Rings," *Phys. Rev. Lett.* **97**, 034801 (Jul. 2006).

[37] M. Billing *et al.*, "Techniques for Observing Beam Dynamical Effects Caused by the Presence of Electron Clouds," in *Proceedings of ECLOUD 2010: 49th ICFA Advanced Beam Dynamics Workshop on Electron Cloud Physics, Ithaca, NY*, K. Smolenski, Ed. (in press).

[38] M. G. Billing *et al.*, "Measurement Techniques to Characterize Instabilities Caused by Electron Clouds," in *Proceedings of the 2011 Particle Accelerator Conference, New York, NY* (in press).

[39] D. L. Kreinick *et al.*, "Application of Coherent Tune Shift Measurements to the Characterization of Electron Cloud Growth," in *Proceedings of the 2011 Particle Accelerator Conference, New York, NY* (in press).

[40] M. A. Palmer *et al.*, "The Conversion and Operation of the Cornell Electron Storage Ring as a Test Accelerator (CesrTA) for Damping Rings Research and Development," in *Proceedings of the 2009 Particle Accelerator Conference, Vancouver, BC* (2009), p. 4200–4204.

[41] J. R. Calvey *et al.*, "CesrTA Retarding Field Analyzer Modeling Results," in *Proceedings of the 2010 International Particle Accelerator Conference, Kyoto, Japan* (2010), p. 1970–1972.